PROCEEDINGS OF 2023 INTERNATIONAL CONFERENCE ON ADVANCES IN MULTIDISCIPLINARY ENGINEERING, SCIENCES AND TECHNOLOGY (ICAMEST), 29-30 SEP 2023 DUBAI, UAE.

ORGANISED BY
ADVANCED ACADEMIC AND RESEARCH CONSULTANCY (AARC)
ISNI 0000000512511788

23 October 2023

Preface to the Conference Proceedings ICAMEST 2023

On behalf of the conference committee, I would like to extend my warmest welcome to allof the attendees to our International Conference on Advances in Multidisciplinary Engineering Sciences and Technology Innovation (ICAMEST 2023). First, I would like to take this opportunity to convey my appreciation to the organizing committee for efforts to make it happen.

Being part of the global community, the significance of engineering sciences and technology is well established. The purpose of this effort was to connect various researchers globally to share the research by the involvement of industry and academic institutions. While considering the innovation we should also be compatible to UNs Sustainable Development Goals (SDGs) for better sustainability of our environment and world.

Overall, the conference provided a truly complete perspective and its an effort to motivate the participants. I'd like to take this chance to thank the participants for their contributions.

Prof. Dr. Md Abdul Kalam
University of Technology Sydney

Preface to the Conference Proceedings

Due to limited time duration for the first International Conference on Advances in Multidisciplinary Engineering Sciences and Technology Innovation (ICAMEST 2023), the scope of conference was only limited to the track of Advances in Mechanical, Materials Engineering & Renewable Energy Technology. On behalf of conference committee, I am thankful to all reviewers for valuable time and contributions. Additionally, we are appreciative for the contributions made by all honorable authors to the conference. Participants from different nations, had the chance to present their works on a wide range of subjects related to various engineering domains.

On behalf of the editors,
Secretary ICAMEST 2023

Conference Committees

Conference Chair

Prof MA Kalam, University of Technology Sydney (UTS) Australia.

Technical Experts & Reviewers

i. Dr. Teoh Yew Heng, Universiti Sains Malaysia (USM)

ii. Dr. Rizwan Fattah, University of Technology Sydney (UTS) Australia

iii. Dr U. Shafiq UCSI University, Malaysia

iv. Dr. T. Amin, NUST, Pakistan

v. Prof Dr Amir Shafeeq, Punjab University, Pk (Expert Chemical Engineering)

vi. Dr Umer Farooq (Expert Mechanical Engineering), KFUEIT, PK

vii. Dr Yasir Niaz (Expert Agriculture Engineering), KFUEIT, PK

viii. Dr Amir Alauddin (Expert Chemical Engineering), NUST, PK

ix. Dr Umar Ijaz GC University PK, (Expert Electrical Engineering)

x. Dr Mubashir Gulzar UET Taxila, (Expert Mechanical Engineering)

xi. Dr Sadia Murawwat LCWU, PK (Expert Electrical and Computer Engineering)

xii. Dr M Tanveer UMT, Pk (Expert Computer Science & Information Technology)

List of Papers

The Influence of Silica Filler on Wear Behavior of Epoxy Composite Coatings for Sliding Tribo-pair

1st Muhammad Kamran Shaukat
Department of Mechanical Engineering
University of Engineering and Technology
Taxila, Pakistan
mkamran.shaukat@students.uettaxila.edu.pk

2nd Mubashir Gulzar
Department of Mechanical Engineering
University of Engineering and Technology
Taxila, Pakistan
Mubashir.gulzar@uettaxila.edu.pk

3rd Zia Ur Rehman
Department of Mechanical Engineering
University of Engineering and Technology
Taxila, Pakistan
ziafaruqi154@gmail.com

4th Muhammad Maarij
Department of Mechanical Engineering
University of Engineering and Technology
Taxila, Pakistan

***Abstract*— Wear is a common issue that may occur in many industrial applications. Therefore, the development of a protective layer is necessary to overcome wear issues. One of the primary strategies for enhancing tribological performance and wear behavior of the components is the epoxy composite coating. The impact of fillers on the wear performance of epoxy composite coating was investigated in this research. The experiments were conducted under four different scenarios such as epoxy filler under dry conditions, epoxy filler under lubrication conditions, and epoxy composite without fillers under dry and lubrication conditions with different loading conditions (10N, 20N, 30N, and 40N) for each experiment. The result demonstrates that the epoxy coating with fillers under lubrication conditions witnessed the lowest wear rate. In lubrication conditions with filler, the wear rate was 98% better than in dry conditions without filler. In the same way, in the dry sliding conditions, there is decreasing in the wear rate with filler by 89% compared to dry sliding conditions without filler. Additionally, SEM analyses were done to investigate the wear process on a worn surface of material samples.**

Keywords— Epoxy composite Coating, Wear Rate, Silica Filler, SEM, Tribology

Introduction

At present, there is a trend toward using lubricants that don't have any additives [1]. Metals like steel quickly wear down when just base lubricating oil is employed [2]. Although polymer coatings find widespread usage in industrial applications [3], due to their poor tribological behavior when exposed to large contact mechanical stresses, these coatings frequently perform poorly. Friction and the wear resistance qualities of material that is produced may be enhanced by using the solid lubricant as a filler in the matrix [4]. Due to the outstanding mechanical and thermal qualities it has, epoxy resin bisphenol A diglycidyl ether ($C_{21}H_{24}O_4$) is often utilized as a thermosetting polymer in a variety of applications [5-7]. These applications include coatings, adhesives, and composites[8-9], Silica particles (SiO_2) are frequently utilized in a wide variety of applications. Some examples of these applications include catalysts, fillers, and biomedical devices.

Epoxy resins wear resistance and mechanical strength have been demonstrated to be greatly increased by conventional inorganic fillers like silicon dioxide or silicon carbide. [10,11]. From the literature, When used with the right filler material and created into a composite, epoxy has unquestionably far better mechanical and tribological properties. Following a study of the literature, the author felt a need for further research on the various tribe behaviors of epoxy resin bisphenol A diglycidyl ether with SiO_2 filler in the form of a composite under dry and lubricated circumstances during reciprocating sliding. Because materials of this sort are utilized in the movement of reciprocation in a great number of mechanical applications, a more comprehensive tribological examination is required. To accomplish this objective, pin-on-disk equipment was utilized for the experimental assessment of wear on steel. In addition, wear tests were done with and without the presence of the epoxy composite covering in both dry and lubricated circumstances.

Experimental Methodlogy

Materials

Araldite 506 (epoxy resin bisphenol A diglycidyl ether) and the Hardener HY 951 were applied as a coating sourced through Al-Hamd Epoxy traders (an international supplier from Lahore). We utilized UNI-CHEM-purchased silica granules with a size range of 7 to 10 µm as filler. A stainless steel 304 pin with 9mm dia. and 25mm length was coated. For all tribological tests, the steel disc with 65 HRC of hardness was employed. SAE 5w-30 (Engine oil) with a 150 viscosity index was used for lubrication.

Composite Preparation

The steel pins (AISI 304) with dimensions of diameter 9 mm and length 25 mm were coated. It took around 10 minutes of evenly swirling epoxy and the hardener HY951 at room temperature to prepare the epoxy composite coating. The hardener ratio for the addition was 2:1. Epoxy resin and silica powder made up 5% of the weight of the composite. A composite epoxy coating with a thickness of between 150 µm and 200 µm was applied to the sample material using the dip coating method and the dispersal of fillers in the resin was made sure by removing the air bubbles using a vaccum pump. The composite sample was then dried for almost 4 hours at the temperature of 80°C in the oven and 20 hours at ambient room temperature. **figure 1** depicts the samples of prepared material.

Figure 1 Material samples

Tribological Test

Pin-on-disk wear equipment was used to conduct tribological testing. To determine the wear rate, wear tests were conducted at room temperature. The wear track radius was set at 35 mm and the rotation of the disk was set at about 300 rpm in the experimental wear test rig. In addition, the time of 7200 sec was also set in the experimental test rig to approach the steady wear process. The wear tests were performed under various loads (such as 10 N, 20 N, 30 N, and 40 N) under dry in addition to lubrication conditions. The following equation can be used to calculate the specified wear rate.

$$K = \frac{\Delta V}{L \times D} \, m^3/Nm \tag{1}$$

Where;

K = Wear rate.
ΔV = Total volume loss during the experiment.
L = Load applied to the specimen.
D = Distance.
Change in mass can be calculated as

$$\Delta m = m_f - m_i \tag{2}$$

Where;
Δm = Changes in mass.
m_f = Final mass of wear.
m_i = Initial mass of wear.
Wear volume can be calculated as

$$\text{Vwear} = \frac{\Delta m}{\rho} \tag{3}$$

Where;
Vwear = Wear volume.
Δm = Change in mass of wear
ρ = Density of wear.
Pin-on-disk on which tests were performed is shown below in **figure 2 and figure 3:**

Figure 2 Pin-on-Disk Apparatus diagram

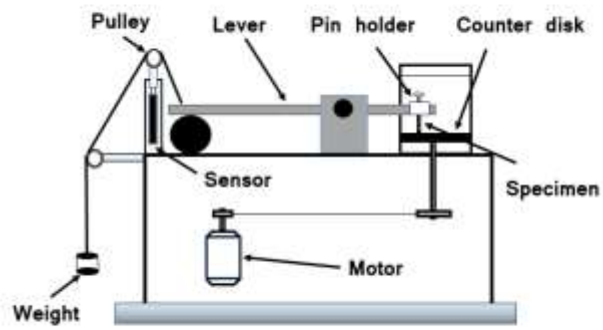

Figure 3 Pin-on-disk Schematic

Results and Discussion

Wear Analysis of the specimen with composite coating

For this study, four separate scenarios were created, including epoxy fillers in dry and lubrication conditions as well as epoxy composite without fillers in both dry and lubrication conditions. The test specimens were subjected to a range of applied loads, including 10, 20, 30, and 40 N. **Figure 4** depicts the comparison between different epoxy composites under different loading conditions. The graph shows that as the applied force rose, the wear rate increased as well. The wear rate reached its maximum and minimum value of 11.28 x 10^{-6} mm^3 /N.m (40 N load) and 3.62857 x 10^{-6} mm^3/N.m (10 N load) respectively for epoxy composite with filler material under dry conditions. In epoxy composite with filler under lubrication conditions, a decreased wear rate was seen in comparison to other examples. The inclusion of a lubricating layer between the base material and disc contact is what causes this decreased wear rate. The wear rate reached its maximum value (0.51 x 10^{-6} mm^3/N.m) and the minimum value (0.15 x 10^{-6} mm^3/N.m) at 40 N and 10 N load respectively for epoxy with filler under lubrication conditions. The epoxy without filler had the highest rate of wear in dry conditions, it was also noticed from the data. The reason is the addition of fillers may be able to withstand heavier loads, increasing the wear load-bearing capability. The specimen material has no filler to protect against the worn surface caused by wear.

Table I highlights the contribution of this work clearly in comparison to the previous works.

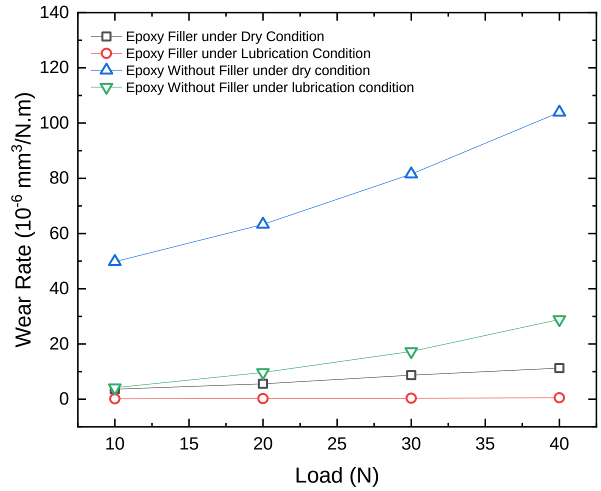

Figure 4 Comparing the difference in wear rate under various loading conditions

Scanning Electron Microscopy (SEM) Analysis

The wear behavior on the specimen's worn surface was investigated using SEM analysis for a specimen with epoxy composite fillers in dry and lubricated conditions. According to the experimental findings, it was determined that under the same loading condition of 30N, the wear rate is higher under the dry state with epoxy filler than it is under the lubrication condition. For dry condition in comparison to when the material was lubricated, the figure depicts cracked, bigger fractures, and debris puller outs creating pits on the work surface as can be seen in **figure 5(a**). Similar results have been observed by Sudheer et al. [17] while using epoxy filler in dry conditions. The graphical representations of depth and distance on the material's worn surface are shown in **figure 5(b)**.The standard Deviation of the wear profile data for epoxy coating with filler under dry condition is 16.87 units which indicates more distance from the mean value as compared to epoxy coating condition under lubricated conditions**.** To investigate the wear process on the specimen's worn surfaces, SEM examination using the epoxy filler under lubrication conditions was also looked at. The loading condition was the same as under dry conditions with epoxy filler material. SEM surface topography is shown in **figure 6(a)**. There are fewer scratches and debris observed under lubrication conditions. This decrement in wear rate on the worn surfaces is due to the implementation of a thin lubrication layer between the disc and pin coated with epoxy. The wear profile for lubrication condition with filler is shown in **figure 6(b)**. The standard deviation of wear profile data obtained from SEM was 7.93 units which indicates less distance from the mean value as compared to dry condition. SEM analysis of material specimens without epoxy filler material under dry condition was also performed at a loading condition of 30N to observe the wear mechanism on the worn surfaces. In **figure 7(a)** the SEM image clearly shows there are more scratches, debris, and more material has been removed from the specimen, and hence there is more wear rate observed during the experiment. Flaky, larger cracks and debris were observed without epoxy composite filler material. The 3D network structure, interstitial empty spaces, and poor surface properties of neat epoxy are the reasons for this. In **figure 7(b)**, the wear profile indicates more roughness present. The standard deviation of wear profile data obtained from SEM was 29.80 units which indicates more distance from the mean value as compared to other conditions.

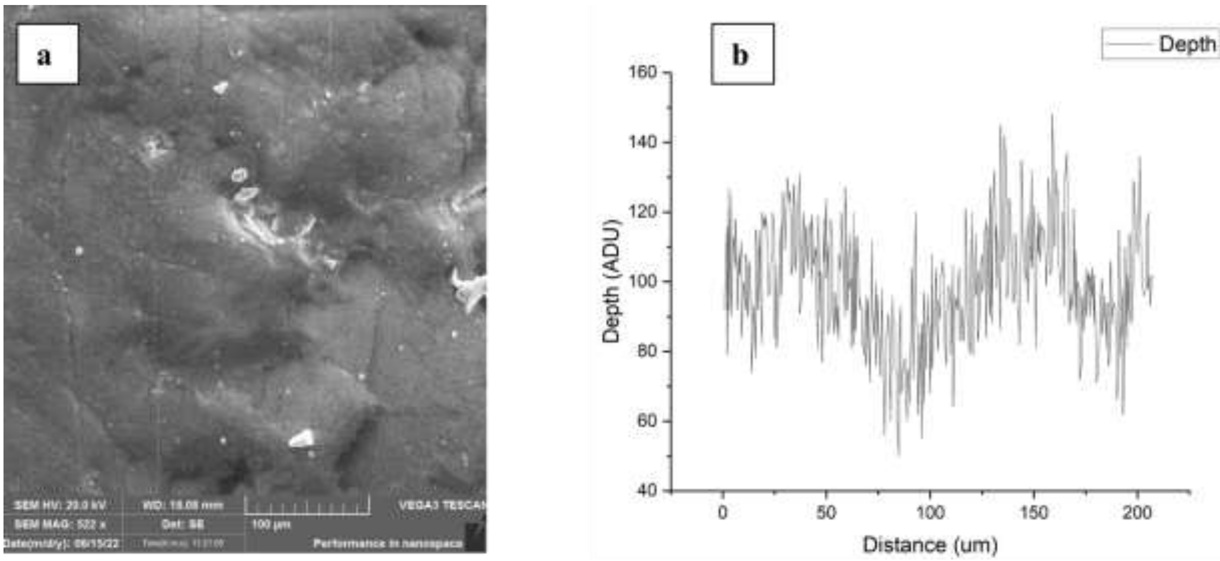

Figure 5 SEM for epoxy composite with filler under dry condition **(a)** SEM Topography **(b)** Wear profile

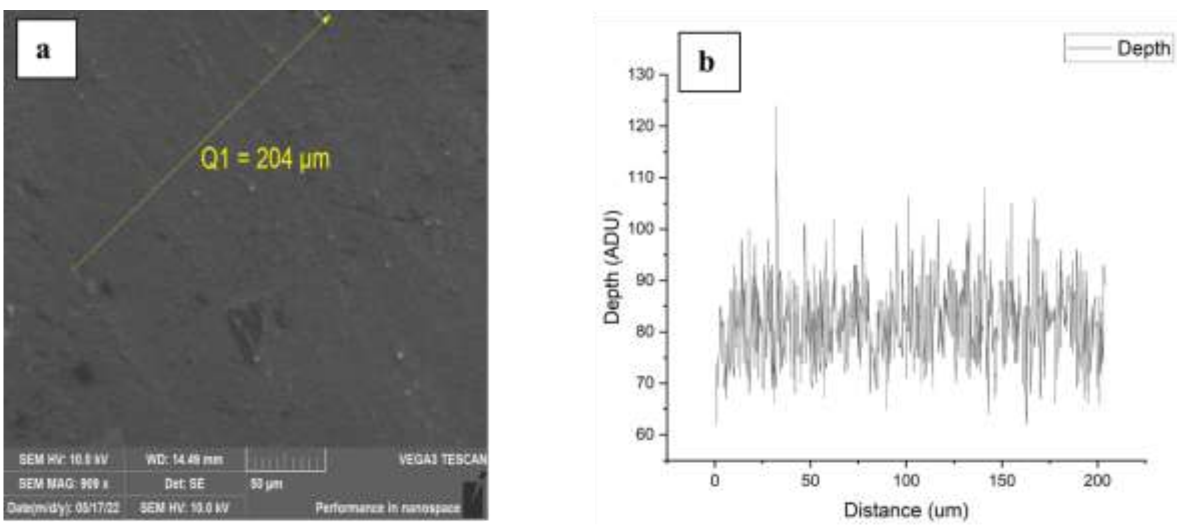

Figure 6 SEM for epoxy composite with filler under lubrication condition **(a)** SEM Topography **(b)** Wear profile

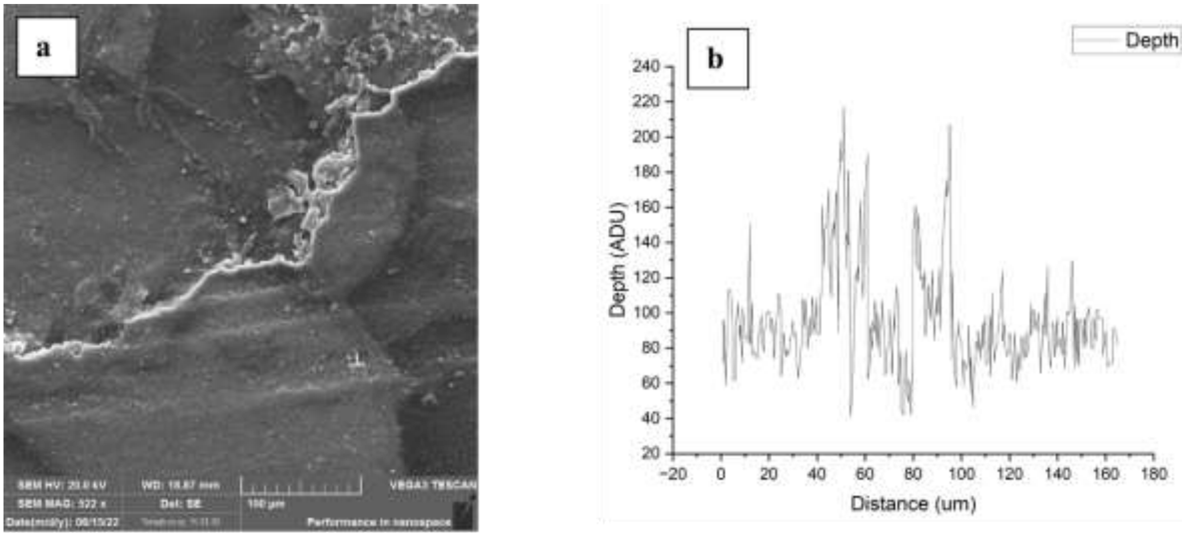

Figure 7 SEM for epoxy composite without filler under dry condition **(a)** SEM Topography **(b)** Wear profile

TABLE I. PARAMETRIC COMPARISON OF LITERATURE REVIEW WITH THE CURRENT STUDY

Reference	**Material**	**Variables**	**Wear under Dry Condition**	**Wear for Lubrication**
Gafsi et al. [12]	Epoxy: Di glycidyl ether of bisphenol A Filler: Graphite Substrate: Aluminum	10N load, Ball on Plan surface, Chromium Ball,	$\approx 6.7\times10^{-4}$ without filler and $\approx 1\times10^{-5}$ with graphite filler	Not Available
Kumar et al. [13]	Epoxy: Araldite AY 103 Filler: Graphite Substrate: Steel	1-5N load, Pin-on-disk, Steel Disk	$15\text{-}55\times10^{-6}$ without filler and $2\text{-}5.5\times10^{-6}$ with filler	$\approx 0.025\text{-}0.05\times10^{-6}$ with filler SN 150 Lubricant
Hao et al. [14]	Epoxy: Di glycidyl ether of bisphenol A Filler: MoS_2, SiC and graphite	60–120N load, Ball-on-disk, Steel ball	$\approx 1\text{-}6\times10^{-6}$ without filler and $\approx 0.5\text{-}18\times10^{-6}$ with different filler.	Not Available
Alajmi et al. [15]	Epoxy: Epoxy resin R246TX Filler: Graphite powder	50N load, Block on the ring, Steel counter face	$\approx 2\times10^{-5}$ without filler and $\approx 0.5\text{-}\approx 0.5\text{-}1\times10^{-5}$ with different filler.	Not Available
Kumar et al. [16]	Epoxy: Di glycidyl ether of bisphenol A Filler: Graphene/Graphite Substrate: Steel	3-10N load, Ball on the cylinder, Steel ball, SN 150 Lubricant	Not available	$\approx 2.5\times10^{-7}$ with graphene filler and $\approx 5.4\times10^{-7}$ with graphite filler
Current Study	Epoxy: Di glycidyl ether of bisphenol A Filler: Silica Substrate: Steel	10-40N load, Pin-on-disk, Steel Disk	$4.9\text{-}10.3\times10^{-5}$ without filler and $3.6\text{-}11.2\times10^{-6}$ with filler	$\approx 1.5\text{-}5\times10^{-7}$ with filler and lubricant

Conclusion

Wear performance and the effect of fillers on the wear behavior were investigated under a variety of circumstances, including epoxy composite without fillers under both dry and lubrication conditions, epoxy filler under dry conditions, and lubrication conditions. The SEM method was utilized to examine wear processes on pin-on-disk equipment during wear assessments at various applied loads.

- The wear rate on the worn surface of the material samples is significantly impacted by the application of the epoxy composite coating with fillers.
- As applied loads increase, the wear rate increases. At applied stresses of 40N and 10N, respectively, the maximum and minimum wear rates were noted.
- The wear process on the material surfaces was also investigated using SEM analysis. SEM tests led to the conclusion that an epoxy composite covering without filler had the highest wear rate. To improve tribological and wear performance, the lubricating layer, both with and without filler materials, is crucial.
- It was also concluded that the wear rate in lubrication conditions with filler decreased by 98% than in dry conditions without silica fillers added. Similarly, the reduction of wear rate in lubrication condition with filler was 89% as compared to dry condition.

The proposed study can be useful for future researchers to examine the impact of composite coating with fillers on the wear behavior and tribological characteristics of materials.

Acknowledgment

We are thankful to our supervisor Dr. Mubashir Gulzar for his guidance throughout my research. Also, we would like to thank Fracture Mechanics Lab UET, Taxila staff for their support during experiment work.

References

[1] H. Ghaednia, … R. J.-J. of E., and undefined 2015, "Experimental analysis of stable CuO nanoparticle enhanced lubricants," *Taylor & Francis*, vol. 10, no. 1, pp. 1–18, Jan. 2015, doi: 10.1080/17458080.2013.778424.

[2] N. Bay *et al.*, "Environmentally benign tribo-systems for metal forming," *Elsevier*, vol. 59, no. 2, p. 760, 2010, doi: 10.1016/j.cirp.2010.05.007.

[3] M. Beardsley, P. Happoldt, K. Kelley, and E. Rejda, "Thermal barrier coatings for low emission, high efficiency diesel engine applications," 1999, Accessed: Mar. 07, 2023. [Online]. Available: https://www.sae.org/publications/technical-papers/content/1999-01-2255/

[4] D. Trabelsi, M. Zouari, M. Kharrat, M. Dammak, M. Eyraud, and F. Vacandio, "Type and concentration effects of particulate solid lubricants on the microstructure, friction, and wear of electrodeposited Ni

composite coatings," *Proceedings of the Institution of Mechanical Engineers, Part J: Journal of Engineering Tribology*, vol. 233, no. 6, pp. 965–974, Jun. 2019, doi: 10.1177/1350650118811057.

[5] Y. Baghdadi, L. Youssef, … K. B.-J. of A., and undefined 2020, "The effects of modified zinc oxide nanoparticles on the mechanical/thermal properties of epoxy resin," *Wiley Online Library*, vol. 137, no. 43, Nov. 2020, doi: 10.1002/app.49330.

[6] E. A. Baroncini, S. Kumar Yadav, G. R. Palmese, and J. F. Stanzione, "Recent advances in bio-based epoxy resins and bio-based epoxy curing agents," *J Appl Polym Sci*, vol. 133, no. 45, Dec. 2016, doi: 10.1002/APP.44103.

[7] S. Krishnan, S. Kumar, S. K. Samal, S. Mohanty, and S. K. Nayak, "Toughening of petroleum based (DGEBA) epoxy resins with various renewable resources based flexible chains for high performance applications: a review," *ACS Publications*, vol. 57, no. 8, pp. 2711–2726, Feb. 2018, doi: 10.1021/acs.iecr.7b04495.

[8] J. Sun *et al.*, "Self-enriched mesoporous silica nanoparticle composite membrane with remarkable photodynamic antimicrobial performances," *Elsevier*, Accessed: Mar. 07, 2023. [Online]. Available: https://www.sciencedirect.com/science/article/pii/S0021979719312019

[9] J. A.-M. R. Foundations and undefined 2021, "Hybrid Materials based on Silica Nanostructures for Biomedical Scaffolds (Bone Regeneration) and Drug Delivery," *books.google.com*, vol. 87, pp. 103–120, 2021, doi: 10.21741/9781644901076-4.

[10] Y. Kang, X. Chen, S. Song, L. Yu, and P. Zhang, "Friction and wear behavior of nanosilica-filled epoxy resin composite coatings," *Appl Surf Sci*, vol. 258, no. 17, pp. 6384–6390, Jun. 2012, doi: 10.1016/J.APSUSC.2012.03.046.

[11] S. W. Koh, J. Kim, J. D. Kim, B. T. Kim, S. O. Hwang, and W. S. Choi, "Effect of Load on the Abrasive Wear of Silica-Filled Epoxy Resin Composites," *Trans Tech Publ*, 2007, doi: 10.4028/www.scientific.net/MSF.544-545.255.

[12] N. Gafsi, I. Smaoui, R. Verdejo, M. Kharrat, M. A. ´ L. Manchado, and M. Dammak, "Tribological and mechanical characterization of epoxy/graphite composite coatings: Effects of particles' size and oxidation," *journals.sagepub.com*, vol. 235, no. 1, pp. 129–137, Jan. 2021, doi: 10.1177/1350650120944273.

[13] V. Kumar, S. K. Sinha, and A. K. Agarwal, "Tribological studies of epoxy and its composite coatings on steel in dry and lubricated sliding," *Tribology - Materials, Surfaces and Interfaces*, vol. 9, no. 3, pp. 144–153, Sep. 2015, doi: 10.1179/1751584X15Y.0000000015.

[14] Y. Hao, X. Zhou, J. Shao, and Y. Zhu, "The influence of multiple fillers on friction and wear behavior of epoxy composite coatings," *Surf Coat Technol*, vol. 362, pp. 213–219, Mar. 2019, doi: 10.1016/J.SURFCOAT.2019.01.110.

[15] M. Alajmi, K. Alrashdan, … T. A.-J. of M., and undefined 2020, "Tribological characteristics of graphite epoxy composites using adhesive wear experiments," *Elsevier*, Accessed: Mar. 15, 2023. [Online]. Available: https://www.sciencedirect.com/science/article/pii/S2238785420318329

[16] V. Kumar, S. Sinha, A. A.-T. International, and undefined 2017, "Tribological studies of epoxy composites with solid and liquid fillers," *Elsevier*, 2016, doi: 10.1016/j.triboint.2016.09.010.

[17] M. Sudheer, R. Prabhu, K. Raju, T. B.-A. in materials science, and undefined 2014, "Effect of filler content on the performance of epoxy/PTW composites," hindawi.com, Accessed: Mar. 07, 2023. [Online]. Available: https://www.hindawi.com/journals/amse/2014/970468/

Response Surface Modeling and Experimental Verification of Mechanical Properties of SMAW Welded Dissimilar ASTM A36 and Hardox 500

1st Hafiz Muhammad Waqas Saleem
Department of Mechanical Engineering
University of Engineering and Technology
Taxila, Pakistan.
waqas.saleem9991@yahoo.com

2nd Mubashir Gulzar
Department of Mechanical Engineering
University of Engineering and Technology
Taxila, Pakistan.
mubashir.gulzar@uettaxila.edu.pk

Abstract—Mechanical properties of the welded joint depict weld quality which along with it depends upon the used welding process and corresponding input parameters. Manufacturing units are in constant search for the efficient methods for the welding to be of the required quality. Substandard process parameter values cause welding defects which in turn leads to inferior mechanical properties of the welded joint. To achieve desired mechanical properties and productivity in SMAW (shielded metal arc welding) it is of the utmost importance to choose the right parameters with optimum values. The past practice was to find optimum values of the parameters was through hit and trial method which is cumbersome and inefficient method leading to the wastage of a lot of resources and time. In this era of depleting resources much research is going on at getting the optimum results with minimum time and wastage. Literature review presents the opportunity of investigating and optimization of welding of Hardox 500 and ASTM A36 which are frequently used in the manufacturing of fan rotors, tractor blades and any structures needing abrasion resistance in order to obtain the required mechanical properties. To improve mechanical properties, performance and weld quality of the mentioned materials, the main goal of the present work is to investigate and optimize the parameters of welding. Selected welding parameters are welding current, groove angle and root gap. For the Design of Experiments, RSM is used. Optimization was done using Minitab to get the best combination of the parameters. The best SMAW parameters combination found out are current of 145Amperes, bevel angle of 65.60º and root gap of 3.3mm.

Keywords— *SMAW, Hardox 500, ASTM A36, RSM, Minitab*

I. Introduction

Welding is a fabrication technique that is used to join two or more materials with or without the application of heat, pressure or filler material. In shielded metal arc welding, the arc being produced between electrode and weld pool helps in joining the metals without the use of pressure. The common welding technique used in industry is shielded metal arc welding [1]. Shielded Metal Arc Welding (SMAW) can be implemented easily in all positions with variety of electrodes [2]. There is no pressure involved in this process. Welder skill in maintaining welding speed, angle, striking of arc and other appropriate adjustments is crucial for obtaining standard joints [3]. The welding plant, welder, electrodes, and work pieces make up the basic SMAW setup [4]. To obtain desired metallurgical and mechanical characteristics, SMAW electrodes are used to weld 70% of metal joints. Numerous low carbon electrodes, including basic low hydrogen (E7018), rutile (E6013), and cellulosic electrodes, are available for SMAW [5]. In order to create an arc of 5000ºC, welding voltage in the range of 15-45 Volts and welding current in the range of 10-500A are used commonly [6]. In many instances the theoretical relation between response and input variables that controls the process is either not available or is very complex. In the situations like these the information about the relation between control and response variables is obtained using empirical methods. RSM is one such technique introduced by box and Wilson which by using mathematical and statistical techniques finds relation between input and output variables and predict the data for the combination of variables for which the experiments haven't been done, it produces an empirical model which approximately describes the process and hence gives mathematical model for the analysis and validation [7]. Response surface methodology (RSM) is used for setting up a series of experimental designs [8]. The most commonly used design in RSM is central composite design (CCD) which fascinated the technical community universally for optimization procedures [9]. M. S. Reddy and M. Vinoth kumar studied four main factors of friction stir welding namely welding speed, tool diameter; tilt angle and tool rotation speed. By applying ANOVA and DOE the significance of the model was gauged [10]. H. Kumar, R. Prasad, P. Kumar, and M. Deo studied gas metal arc welding (GMAW) which is a commonly used welding technique on HSLA A572 gr 50 steel. The process parameters which greatly affect the mechanical properties of HAZ (heat affected zone) and weld bead zone were investigated. The parameters were current, Gas flow rate, and welding speed [11]. A. Kumar, A. Bhattacharyya, and C. Pandey studied the effects of filler composition on mechanical and microstructural properties of dissimilar metals of P92 steel and Ni-based Inconel 617. These metals are used for the manufacturing of boiler components. The joint is prepared by SMAW using the Inconel 617, Inconel 625 and Inconel 82 [12]. S. Tewari, A. Gupta, and J. Prakash investigated the effects of different welding parameters on the weld ability of mild steel specimens having dimensions 50mm× 40mm× 6 mm welded by metal arc welding. The welding current, voltage, speed, heat input rate was chosen as process parameters [13]. M. I. Qazi, R. Akhtar, M. Abas, Q. S. Khalid, A. R. Babar, and C. I. Pruncu . studied the effects of SMAW parameters on the welded ASTM A 516 Gr70. Mechanical properties of the butt weld in flat position at room temperature were investigated. The process parameters were root gap, groove angle, electrode diameter and preheat temperature each at three levels [14]. X. Fan, Y. Li, Y. Qi, X. Cai, Z. Wang, and C. Ma in this study welded a cryogenic high manganese steel with nickel-based material using shielded metal arc welding and submerged arc welding. The testing of the samples indicated that the comprehensive properties of SMAW joints were better than SAW joints [15]. S. Arunkumar. studied the process parameters of metal inert gas commonly known as MIG welding which is used to join two dissimilar metals namely A387 and SS316 stainless steel. The chosen process parameters are voltage, current, bevel angle [16]. L. Natrayan, R. Anand, and S. S. Kumar in this study established an optimization technique using Taguchi method to explore tensile strength of AISI 4140 stainless steel welded joint. Three process parameters namely welding current, welding speed and filler diameter have been selected to perform the required experiments which have been designed using orthogonal array method [17]. V. Panwar, D. K. Sharma, K. P. Kumar, A. Jain, and C. Thakar . investigated the effects of different machining parameters on the surface roughness of EN 36 alloy steel. Design of experiment is done using box-behnken approach. Process parameters were spindle speed, feed rate and cutting depth. The regression model was formed using RSM to predict the best combinations of parameters from 15 experiments [18]. C. Chanakyan, S. Sivasankar, M. Meignanamoorthy, M. Ravichandran, and T. Muralidharan in this study did the parametric optimization of friction stir process parameters namely tool rotational speed, welding speed and axial load. CCD was used to design experiments. 20 experiments with three levels each was used [19]. Sathish, S. D. Kumar, K. Muthukumar, and S. Karthick welded DMR249A steel using GTAW (gas tungsten arc welding) in a single pass with current, torch speed and arc gap as the input variables. They used RSM and Taguchi approach to model the depth of penetration of the weld in a single pass [20]. M. V. Ramana, B. R. Kumar, M. Krishna, M. V. Rao, and V. Kumar applied RSM on Robotic Tungsten Inert Gas welding. The process parameters were current, wire feed and traveling speed. They used RSM to optimize these process parameters to maximize impact strength [21].

The literature review and industry problem present with the opportunity to investigate the research gap of SMAW welding of Hardox 500 and A-36 as there isn't any work done on these particular materials. Novelty of this research work is to solve this industry problem by the optimum selection of welding parameters for optimal weld quality and mechanical properties by using intelligent statistical technique namely RSM. In this study response surface modeling was used to optimize three process parameters to get maximum impact toughness and minimum hardness of the SMAW welded Hardox 500 and ASTM A36, the design of experiment was done using central composite design of response surface methodology.

II. Experimental Details

III. Material

Hardox 500 and ASTM A-36 are the base plate materials for investigation and testing in the current study. Hardox 500 is a high strength low alloy steel with high abrasion and wear resistance. It is mostly used in such type of applications where high abrasion resistance is required such as construction machinery, truck parts, bulldozer blades and boilers ID and FD fan blades. ASTM A36 is most commonly used mild and hot-rolled steel, having excellent welding properties and is very suitable for grinding, punching, and tapping, drilling and machining processes. It is commonly used in construction of oil rigs and in forming bins, tanks, bearing plates, rings, ornamental works, stakes, agricultural equipment, automotive equipment, machinery parts and frames. Many parts that are produced using flame cutting also use this plate. This includes bridges, walkways, ramps, overhead cranes etc. The mechanical characteristic which is found through testing on UTM (ultimate tensile testing machine) for both the materials is given in the TABLE I, and chemical composition which is found using wet analysis technique and spectroscopy is given in the TABLE II and TABLE III.

TABLE II. MECHANICAL CHRACTERISTICS OF MATERIAL

Sr No.	*Property*	*Hardox 500*	*ASTM A36*
1	Tensile Strength (MPa)	1400-1600	400 – 550
2	Yield Strength (MPa)	1250-1400	250

TABLE III. CHEMICAL COMPOSITIOIN OF HARDOX 500

Element	*Mo*	*B*	*C*	*Si*	*Mn*	*Cr*	*Ni*	*P*	*S*
Percentage	0.25	0.25	0.27	0.7	1.6	1	0.25	0.025	0.01

TABLE IV. CHEMICAL COMPOSITIOIN OF ASTM A36

Element	*C*	*Cu*	*Mn*	*P*	*Si*	*S*	*Fe*
Percentage	0.27	0.20	1.03	0.04	0.28	0.05	98

IV. Experimental Apparatus

The welding plant used in this study is three phase Lincoln electric arc plant with potential current range from 50 to 600 Amperes. During the experimentation, welding plant was under calibration dates. Semi-auto flame cutting was used to cut plates from both the plates and edge preparation was done. Electric grinders, chipping hammer and wire brush were used to clean the slag. Electric oven is used to preheat electrode to 100°C. UTM, Charpy impact testing machine and portable hardness tester is used to measure required mechanical properties of the samples. Milling and shaper machines are used to prepare samples for tensile and impact testing as per ASTM A370 standard. Bevel protector was used to measure bevel angles of samples.

V. Design Space for Experimentation

The goal of the experimentation is to optimize process parameters namely electric current, root gap and bevel angle to get maximum impact toughness, maximum tensile strength and minimum hardness. From literature review, shop floor experience, expert's opinion, design specifications of the electrodes and design requirements process parameters ranges were selected. U. Patil and M. Kadam considered welding current, electrode angle, root gap and welding speed as process parameters [22]. S. Janasekaran, W. Tayier used electrode diameter, welding speed and bevel angle as the process parameters [23]. Table IV depicts design space for the experimentation using CCD of RSM.

TABLE V. DESIGN SPACE FOR EXPERIMENTATION

Factors	**Levels**				
	Lowest	***Low***	***Centre***	***High***	***Highest***
Welding Current (Amperes)	108	125	150	175	192
Bevel Angle (degree)	43	50	60	70	77
Root Gap (mm)	1	2	3.5	5	6

VI. Experimental Design

RSM is widely used statistical technique to design the experiments using factorial or partial factorial approach and after analyzing the data using analysis of variance it gives an empirical 1st or 2nd order model to explain the data and also gives significant and insignificant process parameters. After that it uses response surface graphs to optimize for the best possible combination of the process parameters to achieve the desired response. In this study there are three response variables which need to be optimized simultaneously to get the best possible combination of the input parameters. The whole process was done using Minitab software.

VII. Central Composite Design

It is most commonly used design by researchers as it is most popular and flexible. It will always have 2 levels which are high and low and k number of influencing parameters. It consists of axial as well as central points. To create this model 1st of all make a 2^k factorial or 2^{k-p} factorial design and then add axial or star points in it. The 2^k or 2^{k-p} factorial allow us to do curve fitting for first order model while axial points allow us to do curve fitting for 2nd order model. This is the model which we used in this study. The design was done in Minitab software version 19.

VIII. Design Matrix with Output Responses

20 samples being prepared using the parametric combinations found using CCD depicting in TABLE V. The samples were prepared by first cutting the plates of sizes 120×120mm from both the material plates, then bevels were prepared using grinders. After grinding welding of the samples were done using E7018 electrode of diameter 4mm with SMAW apparatus, after tacking was done all samples were pre heated to avoid hydrogen cracking and welding defects. Welding was done in flat 1G position with butt welded joint type. Welding electrodes were warmed to 100°C in an electric oven. Same welding facility and conditions with same welder

was used to avoid likelihood of the issues due to these factors. After each pass slag was removed using chipping hammer, grinding and wire brushing. 20 tensile, hardness and impact samples were prepared to measure the properties at each combination. 100TON UTM, portable hardness tester and V-notch Charpy impact tester was used to find the values of impact toughness, hardness and tensile strength.

TABLE VI. DESING MATRIX WITH RESPONSES

Sr. No	***Current (Amperes)***	***Bevel Angle (Degree)***	***Root Gap(mm)***	***Hardness (HRC)***	***Impact (Joules)***	***Tensile (MPa)***
1	125	50	2	28.7	79	498
2	175	50	2	27.3	105	514
3	125	70	2	23	112	514
4	175	70	2	25.6	116	509
5	125	50	5	28.3	124	512
6	175	50	5	28.3	108	506
7	125	70	5	27.6	117	508
8	175	70	5	30	103	497
9	108	60	3.5	25.6	99	510
10	192	60	3.5	32.3	109	510
11	150	43	3.5	26	122	518
12	150	77	3.5	27	115	504
13	150	60	0.97	27.3	103	509
14	150	60	6	27	125	506
15	150	60	3.5	23.6	121	510
16	150	60	3.5	23.3	120	510
17	150	60	3.5	23.3	121	498
18	150	60	3.5	23	119	495
19	150	60	3.5	23	119	512
20	150	60	3.5	23	120	500

IX. Held Constant Variables

The held constant variables during the experimentation of the samples are presented in the TABLE VI.

TABLE VII. HELD CONSTANT VARIABLES

Electrode Type/ Diameter	***Preheat Temperature***	***Welding Voltage***	***Welding Position***	***Polarity***	***Plate Thickness***	***Root Face***
E-7018/4mm	100 ^{o}C	Auto	1 G	Reverse	10mm	2mm

X. Results and Discussions

The results of experimentation are analyzed with RSM using Minitab software. Regression was done for each of the response variables i.e. tensile, impact and hardness. RSM uses ANOVA as a tool to analyze the data which is being collected from experiments to find P-values and F-values which depicts model validation and significance of the input parameters. RSM explains the relation between several explanatory variables and one or more response variables. All the samples were broken from the base metal (ASTM A36 side) so the tensile test was cleared by all the samples so it is not included in the optimization of the multi response optimization.

XI. Hardness

When response surface regression was done on the data set which we got from the experimentation, results as depicted by Table VII were obtained. ANOVA was done using 95% confidence interval.

TABLE VIII. ANOVA FOR HARDNESS

Source	*DF*	*Adj SS*	*Adj MS*	*F-Value*	*P-Value*
Model	9	99.164	11.0183	3.94	0.022
Linear	3	23.874	7.9581	2.85	0.091
Current	1	16.187	16.1866	5.79	0.037
Bevel Angle	1	1.630	1.6301	0.58	0.463
Root Gap	1	6.058	6.0576	2.17	0.172
Square	3	61.170	20.3901	7.30	0.007
Current*Current	1	43.262	43.2622	15.48	0.003
Bevel Angle*Bevel Angle	1	10.818	10.8181	3.87	0.077
Root Gap*Root Gap	1	17.318	17.3181	6.20	0.032
2-Way Interaction	3	14.120	4.7067	1.68	0.233
Current*Bevel Angle	1	5.120	5.1200	1.83	0.206
Current*Root Gap	1	0.180	0.1800	0.06	0.805
Bevel Angle*Root Gap	1	8.820	8.8200	3.16	0.106
Error	10	27.942	2.7942		
Lack-of-Fit	5	18.231	3.6463	1.88	0.253
Pure Error	5	9.711	1.9422		
Total	19	127.106			

The Table VII shows that squared model is the most significant of all as squared current is most significant factor to affect hardness. Squared Root gap is also significantly affecting the hardness. The P value of 0.037 for current depicts that current is the significant factor in affecting hardness and Fig. 1 also depicts that. P value of 0.253 indicates that lack of fit is insignificant and model is adequately explaining the data. Based on the above data mathematical model (1) is obtained where C is current, B is bevel, A is angle, R is root, and G is gap.

$$Hardness = 162.9 - 0.99 \times C - 1.8 \times BA - 7.8 \times RG + 0.002 \times C^2 + 0.008 \times BA^2 + 0.487 \times RG^2 + 0.003 \times C \times BA + 0.004 \times C \times RG + 0.07 \times BA \times RG \quad (1)$$

XII. Pareto Chart

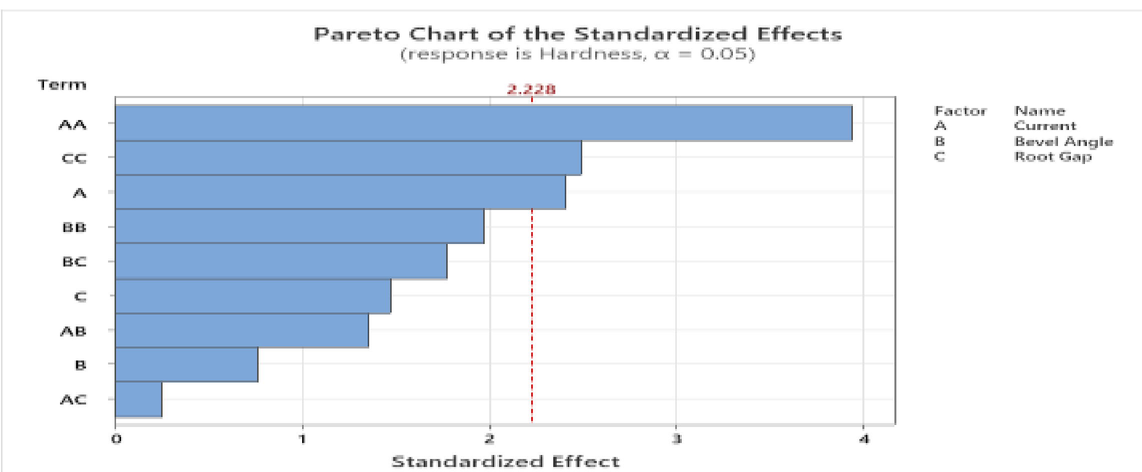

Fig. 1. Pareto Chart for the Standardized Effects of Hardness

XIII. Contour Plots for Hardness

Contour plots in the Fig. 2 shows that for Fig. 2a at hold value of root gap of 3.5mm the desired region is between bevel angle of 55º to 60º and current of 135A to 160A. For Fig. 2b at the hold value of bevel angle of 60º the optimum region for the hardness is between root gap of 3-3.5mm and current of 140A to 145A. For Fig. 2c at the hold value of current of 150A, the optimum region lies at the root gap of 2-3mm and bevel angle of about 65⁰. The contour plots show that as the current increases hardness decreases up to some point and then increases after words, taking into consideration Fig. 2a, at the bevel angle of 65⁰ as the current increases from 120A hardness decreases and as it increases further after 165A it starts to increase, the reason for which is that as the current increases the hotter weld pools are created at the fusion zone which have higher cooling rates thus promoting the formation of martensite which is the indicator of increase in hardness and brittleness [14], same can be seen for root gap as it increases the depth of penetration and large area necessitates the requirement of higher heat input to cater for higher deposition rate, this results in widened heat affected zone and large residual stresses in the weld joint thus leading to higher hardness values. These observations are in line with the findings of previous studies [24][25][26].

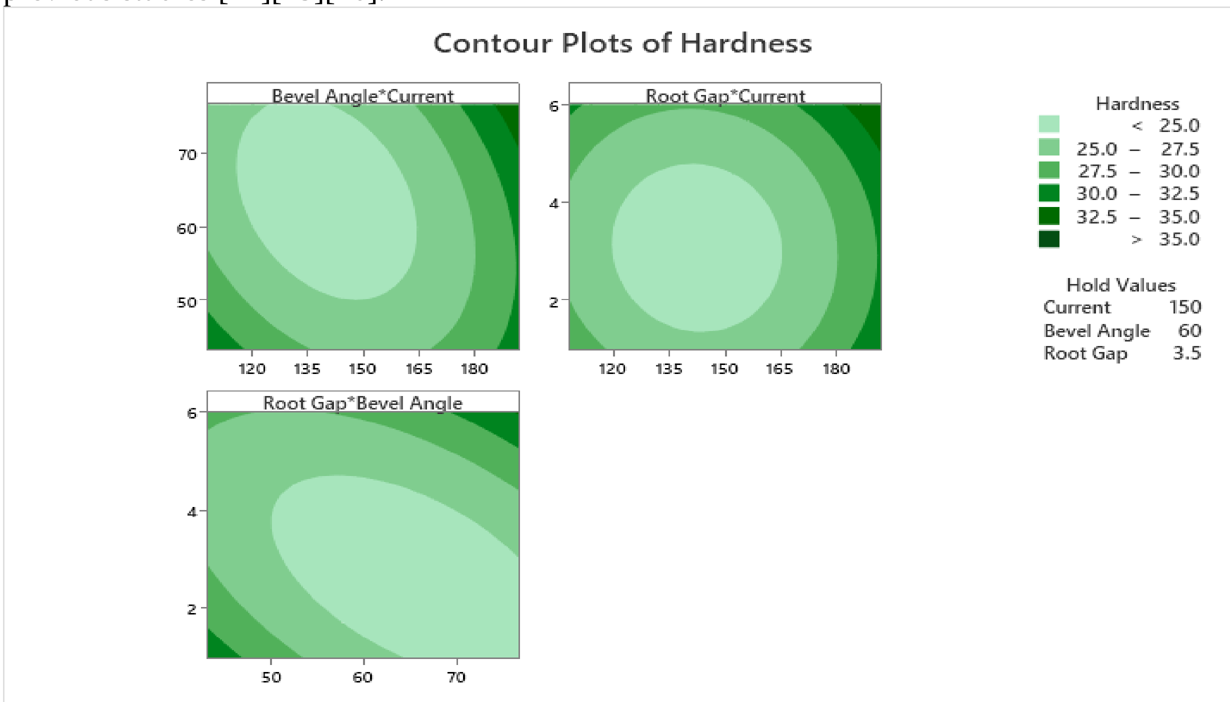

Fig. 2. Contour Plots for Hardness a) Bevel Angle vs Current b) Root Gap vs Current c) Root Gap vs Bevel Angle

XIV. Impact Toughness

The Table VIII for the ANOVA shows that squared and two-way interaction as well as linear model are all significant while for the predictor terms root gap, squared current, interaction of current, root gap and bevel angle are also significant. Lack of fit is not significant as it has very high value of 0.609 for the significance interval of 0.05. Root Gap is the most significant term which is affecting impact properties. Fig. 3. Also depicting the same pattern that root gap, interaction and squared terms are significant.

TABLE IX. ANOVA FOR IMPACT TOUGNESS

Source	***DF***	***Adj SS***	***Adj MS***	***F-Value***	***P-Value***
Model	9	2174.61	241.62	9.94	0.001
Linear	3	587.44	195.81	8.05	0.005
Current	1	34.86	34.86	1.43	0.259
Bevel Angle	1	60.24	60.24	2.48	0.147
Root Gap	1	492.35	492.35	20.25	0.001

Square	3	665.79	221.93	9.13	0.003
Current*Current	1	559.83	559.83	23.02	0.001
Bevel Angle*Bevel Angle	1	91.55	91.55	3.76	0.081
Root Gap*Root Gap	1	104.84	104.84	4.31	0.065
2-Way Interaction	3	921.37	307.12	12.63	0.001
Current*Bevel Angle	1	78.12	78.12	3.21	0.103
Current*Root Gap	1	378.12	378.12	15.55	0.003
Bevel Angle*Root Gap	1	465.12	465.12	19.13	0.001
Error	10	243.19	24.32		
Lack-of-Fit	5	105.86	21.17	0.77	0.609
Pure Error	5	137.33	27.47		
Total	19	2417.80			

Based on the data presented in the TABLE VIII mathematical model (2) for the impact toughness is obtained

$$Impact = -561 + 4.5 \times \mathrm{C} + 6.9 \times \mathrm{BA} + 70.4 \times \mathrm{RG} - 0.009 \times \mathrm{C}^2 - 0.0252 \times \mathrm{BA}^2 - 1.2 \times \mathrm{RG}^2 - 0.012 \times \mathrm{C} \times \mathrm{BA} - 0.1833 \times \mathrm{C} \times \mathrm{RG} - 0.50 \times \mathrm{BA} \times \mathrm{RG} \quad (2)$$

XV. Pareto Chart

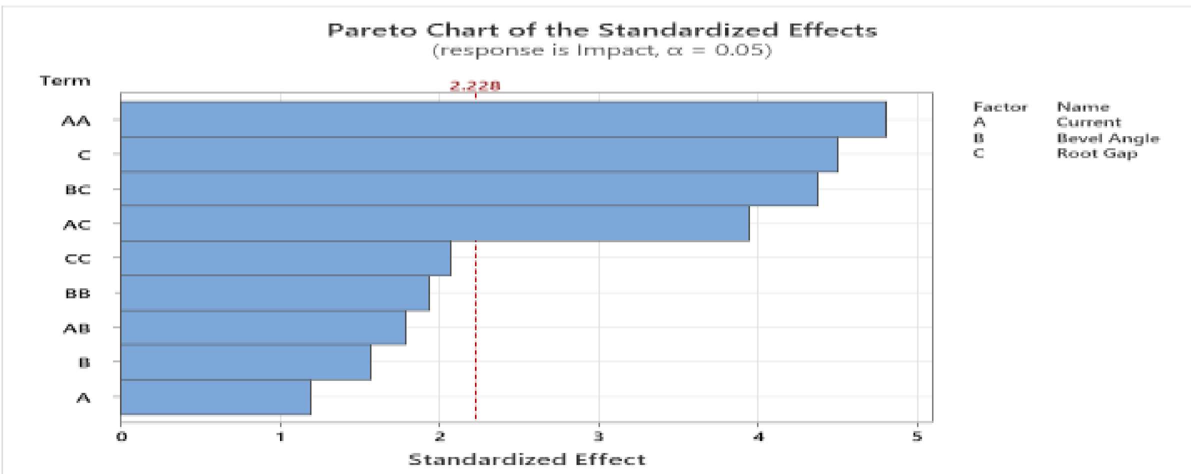

Fig. 3. Pareto Chart for the Standardized Effects of Impact Tougness

XVI. Contour Plots for Impact

The dark green area in the contour plots of Fig. 4 is desired area for the maximum impact toughness. In Fig. 4a for the hold value of root gap of 3.5mm the maximum impact toughness occurs at the bevel angel of 60-65º and current of 145 to 150A. In Fig. 4b for the hold value of bevel angle of 60º this region occurs at root gap of 4 to 5 mm and current of 120A to 165A. In Fig. 4c at the hold value of current at 150A the desired region lies between 5-6mm root gap and bevel angle of 40º to 50º. Contour plots show that as the current increases so does the impact toughness but it starts decreasing at higher values of current, this finding is in line with the studies [27][28]. Fig.4a depicts that at root gap of 3.5mm impact dramatically increases with the increases in groove angle, this trend is in line with [14]. With increase in root gap impact toughness increases due to increase in heat affected zone, uniform weld pool and homogenized grain structure leading to improved properties, this finding is in line with [29].

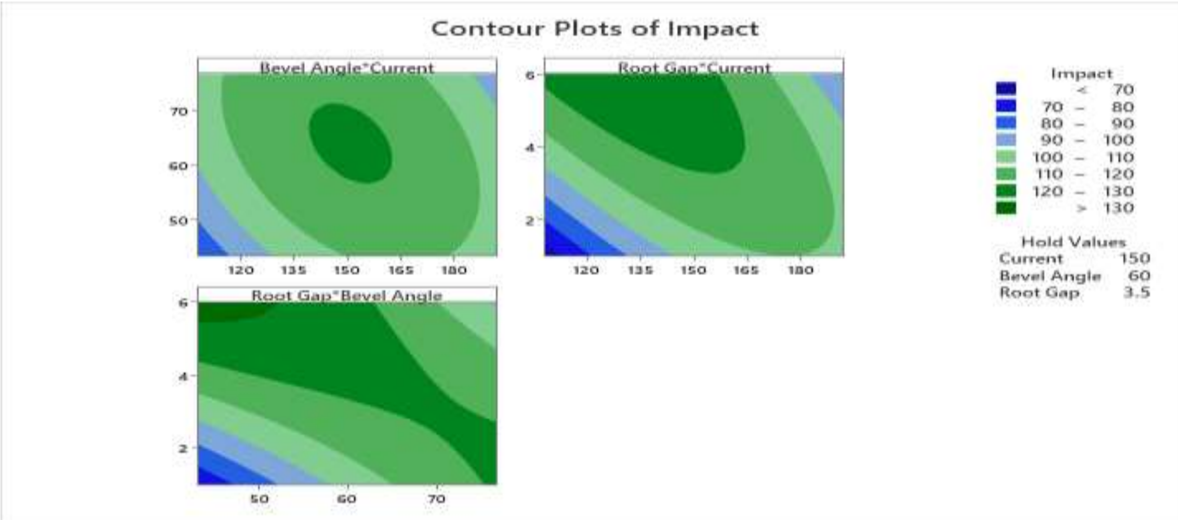

Fig. 4. Contour Plots for Impact Toughness. a) Bevel Angle vs Current b) Root Gap vs Current c) Root Gap vs Bevel Angle

XVII. Multiple Response Optimization

Multi response optimization was done using the criteria of maximum impact toughness and minimum hardness. Equal importance was given to both the properties and composite desirability of 0.87 was obtained. The response optimizer of the Minitab software was used and following results were obtained.

TABLE X. SOLUTION FOR OPTIMIZATION

Solution	*Current*	*Bevel Angle*	*Root Gap*	*Impact Fit*	*Hardness Fit*
1	144.4	65.6	3.27	120.2	23.4

The solution suggests that the current of 145Amperes, bevel angle of 65.60^{o} and root gap of 3.3mm is the best possible combination to get the maximum impact and minimum hardness of the welded samples of Hardox 500 and ASTM A36.

XVIII. Validation

Validation experimentation was done using the optimized setting values for current, bevel angle and root gap. The sample was welded and then samples for impact and hardness were taken and tested. The value for hardness we got was 22.5 HRC while average value for the impact was 118J. This proves that the best results were obtained at these optimized settings.

XIX. Conclusion

- For tensile strength each sample when loaded was broken from the A36 side of the welded sample which means that for tensile specimen each sample passed the test and hence any combination of the setting will produce the desired result
- For Hardness current is the most significant factor affecting it. As the squared terms are significant it implies that quadratic model should be used to curve fit the response of the experiments.

- For Impact toughness root gap is the most significant factor which affects it the most. Also, interaction terms significance implies that quadratic model must be used to curve fit the observations
- Multi response optimization using Minitab software while setting hardness to minimum and impact to maximum and giving equal weights to both suggests the best possible combination of the parameters to be current 145A, bevel angle 66º and root gap of 3.2mm.
- For tensile specimen it was determined by examining the broken samples that the welded joint had more strength as compared to base metal.
- The least significant factor is found to be groove angle but it interacted with others to affect the responses.

Acknowledgment

This research work was done under the kind supervision of sir Dr Mubashir Gulzar and all the material, testing facilities were provided by my organization HMC Taxila, I am eternally grateful for all the people who in any capacity contributed to this work.

References

G. S. Sidhu and S. S. Chatha, "Role of shielded metal arc welding consumables on pipe weld joint," International journal of emerging technology and advanced engineering, vol. 2, no. 12, pp. 746-750, 2012*)*

A. Dadi, P. B. Goyal, and M. H. Patel, "A review paper on optimization of shielded metal arc welding parameters for welding of (Ms) Sa-516 Gr. 70 plate by using Taguchi approach," International Journal of Scientific Research in Science and Technology, vol. 4, no. 5, pp. 1536-43, 2018.

S. B. AV and P. Giridharan, "Productivity improvement in flux assisted TIG welding," International Journal on Design and Manufacturing Technologies, vol. 6, no. 2, 2012.

A. K. Paul, "Robust product design using SOSM for control of shielded metal arc-welding (SMAW) process," IEEE Transactions on Industrial Electronics, vol. 63, no. 6, pp. 3717-3724, 2016.

A. K. Paul, "Practical realization of scalar optimization function of shielded metal arc welding process," IFAC Proceedings Volumes, vol. 47, no. 1, pp. 684-691, 2014..

Y. H. Huijie Liu, Encyclopedia of Materials: Metals and Alloys. 2022.

L. A. S. a. M. C. Ortiz, Response Surface Methodology. Elsevier B.V., 2009

R. H. Myers, D. C. Montgomery, and C. M. Anderson-Cook, Response surface methodology: process and product optimization using designed experiments. John Wiley & Sons, 2016.

D. C. Montgomery, "Design and Analysis of Experiments, eight edition," Joh Wiley and Sons, 2013

M. S. Reddy and M. Vinoth kumar, "Friction stir welding parameters optimization of naval grade AA5083 alloy: RSM," International Journal on Interactive Design and Manufacturing (IJIDeM), pp. 1-12, 2023

H. Kumar, R. Prasad, P. Kumar, and M. Deo, "Microstructural and mechanical properties of GMAW welded 572 GR 50 steel," Materials Today: Proceedings, 2023

A. Kumar, A. Bhattacharyya, and C. Pandey, "Structural Integrity Assessment of Inconel 617/P92 Steel Dissimilar Welds Produced Using the Shielded Metal Arc Welding Process," Journal of Materials Engineering and Performance, pp. 1-19, 2023

S. Tewari, A. Gupta, and J. Prakash, "Effect of welding parameters on the weldability of material," International Journal of Engineering Science and Technology, vol. 2, no. 4, pp. 512-516, 2010

M. I. Qazi, R. Akhtar, M. Abas, Q. S. Khalid, A. R. Babar, and C. I. Pruncu, "An integrated approach of GRA coupled with principal component analysis for multi-optimization of shielded metal arc welding (SMAW) process," Materials, vol. 13, no. 16, p. 3457, 2020

X. Fan, Y. Li, Y. Qi, X. Cai, Z. Wang, and C. Ma, "Mechanical properties of cryogenic high manganese steel joints filled with nickel-based materials by SMAW and SAW," Materials Letters, vol. 304, p. 130596, 2021.

S. Arunkumar et al., "Taguchi optimization of metal inert gas (MIG) welding parameters to withstand high impact load for dissimilar weld joints," Materials Today: Proceedings, vol. 56, pp. 1411-1417, 2022.

L. Natrayan, R. Anand, and S. S. Kumar, "Optimization of process parameters in TIG welding of AISI 4140 stainless steel using Taguchi technique," Materials today: proceedings, vol. 37, pp. 1550-1553, 2021

V. Panwar, D. K. Sharma, K. P. Kumar, A. Jain, and C. Thakar, "Experimental investigations and optimization of surface roughness in turning of en 36 alloy steel using response surface methodology and genetic algorithm," materials today: proceedings, vol. 46, pp. 6474-6481, 2021

C. Chanakyan, S. Sivasankar, M. Meignanamoorthy, M. Ravichandran, and T. Muralidharan, "Experimental investigation on influence of process parameter on friction stir processing of AA6082 using response surface methodology," Materials Today: Proceedings, vol. 21, pp. 231-236, 2020

T. Sathish, S. D. Kumar, K. Muthukumar, and S. Karthick, "Natural inspiration technique for the parameter optimization of A-GTAW welding of naval steel," Materials Today: Proceedings, vol. 21, pp. 843-846, 2020

M. V. Ramana, B. R. Kumar, M. Krishna, M. V. Rao, and V. Kumar, "Optimization and influence of process parameters of dissimilar SS304L–SS430 joints produced by Robotic TIG welding," Materials today: proceedings, vol. 23, pp. 479-482, 2020

U. Patil and M. Kadam, "Microstructural analysis of SMAW process for joining stainless steel 304 with mild steel 1018 and parametric optimization by using response surface methodology," Materials Today: Proceedings, vol. 44, pp. 1811-1815, 2021.

S. Janasekaran, W. Tayier, G. J. Hoe, and T. H. Hong, "Optimization of Tensile Strength in Automated Shielded Metal Arc Welding Using Taguchi Technique," in *Advances in Material Science and Engineering: Selected articles from ICMMPE 2020*, 2021: Springer, pp. 364-369

S. Suntari, H. Purwanto, S. M. B. Respati, S. Sugiarto, and Z. Abidin, "Effect of Electrode Diameter and Current on Dissimilar Metal Welding (Stainless Steel-Galvanized Steel) in Bus Body Construction: Microstructure and Properties Evaluation," *Automotive Experiences*, vol. 5, pp. 402-415, 2022.

S. I. Talabi, O. B. Owolabi, J. A. Adebisi, and T. Yahaya, "Effect of welding variables on mechanical properties of low carbon steel welded joint," *Advances in Production Engineering & Management*, vol. 9, pp. 181-186, 2014

G. Jang, H. Kim, and S. Kang, "The effects of root opening on mechanical properties, deformation and residual stress of weldments," *Welding journal*, vol. 80, pp. 80-89, 2001.

Naik, A.Balaram. (2018). The Analysis of SMAW Parameters for Optimization of Mechanical Properties using Taguchi Method on DSS Material. International Journal for Research in Applied Science and Engineering Technology. 6. 2976-2985. 10.22214/ijraset.2018.1409.

Yadav AK, Kumar A, Singh CP, Singh AK, Nand MS. Studies on impact of welding parameters on angular distortion and mechanical properties of structural steel welded by SMAW. Int. Res. J. Mod. Eng. Technol. Sci. 2020;2(5):445-59.

Baghel PK. Effect of SMAW process parameters on similar and dissimilar metal welds: An overview. Heliyon. 2022 Dec 9.

Biochar-Based Photocatalysts: A Revolutionary Approach for theDegradation of Organic Pollutants

Engr. Muhammad Suleman

Lecturer, ICEE, Deputy Director, Career Counseling Centre, KFUEIT, Rahim Yar Khan

Abstract:

Environmental pollution due to organic contaminants has become a significant global concern, necessitating innovative and sustainable solutions. This review explores the revolutionary approach of using biochar-based photocatalysts for the degradation of organic pollutants. Biochar, derived from biomass pyrolysis, offers a porous structure and high surface area, makingit an ideal candidate for enhancing photocatalytic properties when combined with metal oxides and sulphides. The integration of metal-based photocatalysts with biochar results in materials with improved efficiency, stability, reusability, and affordability. These biochar-based photocatalysts hold immense promise for applications in wastewater treatment, soil and groundwater remediation, and air purification. The photocatalysis process itself involves the generation of electron-hole pairs under light illumination, prominent to the photocatalytic degradation of organic pollutants through the production of reactive radicals. In this review we discussed several synthesis methods which have been developed to create biochar-based photocatalysts with varying properties and structures. Properties such as enhanced surface area, active sites, electron transport, electron reservoir capacity, and improved charge separationefficiency contribute to the superior performance of biochar-supported photocatalysts. This review represents the recent development and progress of biochar-based materials and their photocatalytic performance for the degradation of organic pollutants in wastewater. Overall, biochar-based photocatalytic materials represent a sustainable and promising approach for addressing environmental pollution. Their ability to harness solar energy for pollutant degradation, coupled with their cost-effectiveness and eco-friendliness, makes them a powerful tool in the quest for a cleaner and healthier world. Further research and optimization of these innovative materials hold the key to a more sustainable and pollution-free future.

Keywords: Biochar, Photocatalyst, Organic pollutants, Photocatalytic degradation

1 Introduction

In our ever-evolving world, environmental pollution has emerged as a menacing global challenge. As industries burgeon and urbanization surges, the inadvertent release of organic pollutants into the environment has reached alarming proportions [1]. The deleterious effects of these pollutants on both human health and the environment cannot be overstated. Finding effective and sustainable solutions to combat this pressing issue has become a matter of paramount importance [2].

In photocatalysis, biochar-based photocatalyst is a cutting-edge and innovative approach to tackling organic pollutant degradation. These remarkable materials, incorporating metal oxides and sulphides, have emerged as potential game-changers in the realm of environmental remediation [3]. By seamlessly merging the ancient wisdom of biochar with cutting-edge nanotechnology, biochar-based photocatalysts hold the promise of not only mitigating the adverse effects of organic pollutants but also fostering a greener and more sustainable future [4]. Controlling the decomposition of organic contaminants is a crucial issue. Chemical compounds such as insecticides, dyes, medications, and byproducts from industrial processes are all included in the category of pollutants [5]. Environmental systems, water supplies, and human populations are all negatively impacted by the pervasiveness of these compounds. Physical and chemical treatments, the two most common methods for eliminating pollutants, have been found to be inefficient in a number of ways. Therefore, a long-term plan that is both effective and ecologically benign is required. Photocatalysts made from charcoal have great potential in this regard [6].

Biochar, which is a material that is rich in carbon and is produced from the pyrolysis of biomass, has been used for a number of years as a method of enhancing the quality of soil and storing carbon [7]. Because of the material's porous structure, substantial surface area, and robust carbonmatrix, it is an appealing candidate for use in a wide variety of contexts. In spite of this, a huge step forward was taken when researchers started the process of enhancing biochar with metal oxides and sulphides in order to magnify the photocatalytic properties it had [8].

This novel approach is predicated on the combination of biochar with metal oxides or sulphides as its primary constituents. Titanium dioxide (TiO_2) [9] and zinc oxide (ZnO) [10] are two examples of metal oxides that have shown extraordinary photocatalytic activity owing to their capacity to create electron-hole pairs when exposed to ultraviolet (UV) or visible light. Because of this special quality, the entities are able to convert organic pollutants into harmless byproducts [11]. The photocatalytic potential of sulphides, such as cadmium sulphide (CdS) [12], zinc sulphide (ZnS) [13], and molybdenum sulphide (MoS2) [14], has also been shown. A dramatic change takes place when these metal-based photocatalysts are combined with biochar [15].

This novel approach is predicated on the combination of biochar with metal oxides or sulphides as its primary constituents. Titanium dioxide (TiO_2) [9] and zinc oxide (ZnO) [10], metal oxides that have shown extraordinary photocatalytic activity owing to their capacity to create electron- hole pairs when exposed to ultraviolet (UV) or visible light. Because of this special quality, the entities are able to convert organic pollutants into harmless byproducts [11]. The photocatalytic potential of sulphides, such as cadmium sulphide (CdS) [12] and zinc sulphide (ZnS) [13] molybdenum sulphide (MoS_2) [14], has also been shown efficient photodegradation activity. An affected change takes place when these metal-based photocatalysts are combined with biochar [15].

Biochar's surface area is considerably improved when metal oxides or sulphides are added for photocatalysis. Biochar's porous nature makes it a great medium for immobilizing metal nanoparticles, which improves their ability to react to light and organic pollutants [16]. [16]. Biochar's synergistic impact with metal-based photocatalysts improves photo catalysis overall efficiency and the catalyst's longevity, reducing the frequency with which the catalyst must be replaced [17].

Biochar-based photocatalysts have other advantageous properties, such as stability and reusability. When compared to traditional photocatalysts, which often have problems with photo-corrosion or aggregation, biochar-based compounds show outstanding endurance [18]. This leads to the discovery of more long-lasting and cost-effective strategies for the breakdown of organic contaminants [19] Biochar, as a component of these photocatalysts, is ecologically benign and sustainable since it may be generated from a variety of renewable biomass sources [19]. Moreover, biochar-derived photocatalysts provide not only environmental advantages but also economic benefits. The cost associated with the manufacture of biochar is rather reasonable, and its integration with metal oxides or sulphides does not need complex or expensive processes [20]. The cost-effectiveness of biochar-based photocatalysts makes them an appealing choice for extensive implementation, especially in areas where limited resources are a significant consideration [21].

For the advancement of biochar based photocatalytic material, in this review we represents the development of biochar-based photocatalysts incorporating metal oxides and sulphides, a paradigm shift in the field of organic pollutant degradation. This review provides insights into recent advancements in the synthesis of biochar based photocatalytic material. It covers the synthesis, delves into the general properties of biochar, including their photocatalyticcharacteristics. This study also examines into the relevance of various biochar-basedphotocatalysts and explains their function in the photocatalytic performance used for the degradation of organic contaminants in wastewater.

2 Photocatalysis Process

Photocatalysis, an established advanced oxidation process (AOP), offers a simple, cost-effective,and environmentally friendly solution for the degradation of organic pollutants. This process harnesses the power of light to activate a photocatalyst, initiating a series of reactions that lead tothe degradation of pollutants [22].

When the photocatalyst is illuminated by light, the electrons in the valence band (VB) of the photocatalyst get excited and migrate into the conduction band (CB), which results in theformation of electron-hole pairs (Equation 1). Because the holes in the valence band (h^+) have a significant oxidizing potential, they are able to combine with hydroxide ions (OH^-) or water molecules (H_2O) to produce hydroxyl radicals ($^\bullet OH$) (Equation 2). At the same time, oxygen molecules have the ability to scavenge photogenerated electrons in the conduction band, which results in the production of superoxide radical anions (O^{2-}) (Equation 3) [23].

$$Photocatalyst + hv \rightarrow h^+_{VB} + e^-_{CB} \quad \text{(Eq. 1)}$$

$$OH^- + h^+ \rightarrow OH^\cdot \quad \text{(Eq. 2)}$$

$$O_2 + e^- \rightarrow O_2^{\cdot -} \quad \text{(Eq. 3)}$$

Both hydroxyl radicals ($OH^\bullet$) and superoxide radical anions ($O_2^{\bullet -}$) are essential in the process oforganic pollutant breakdown. These highly reactive entities engage in chemical reactions withcontaminants, causing the disruption of their chemical bonds and subsequent conversion into fewer complexes and less detrimental molecules. In conclusion, the degradation process culminates in the generation of water, carbon dioxide, and several other by-products (Fig. 1)[23].

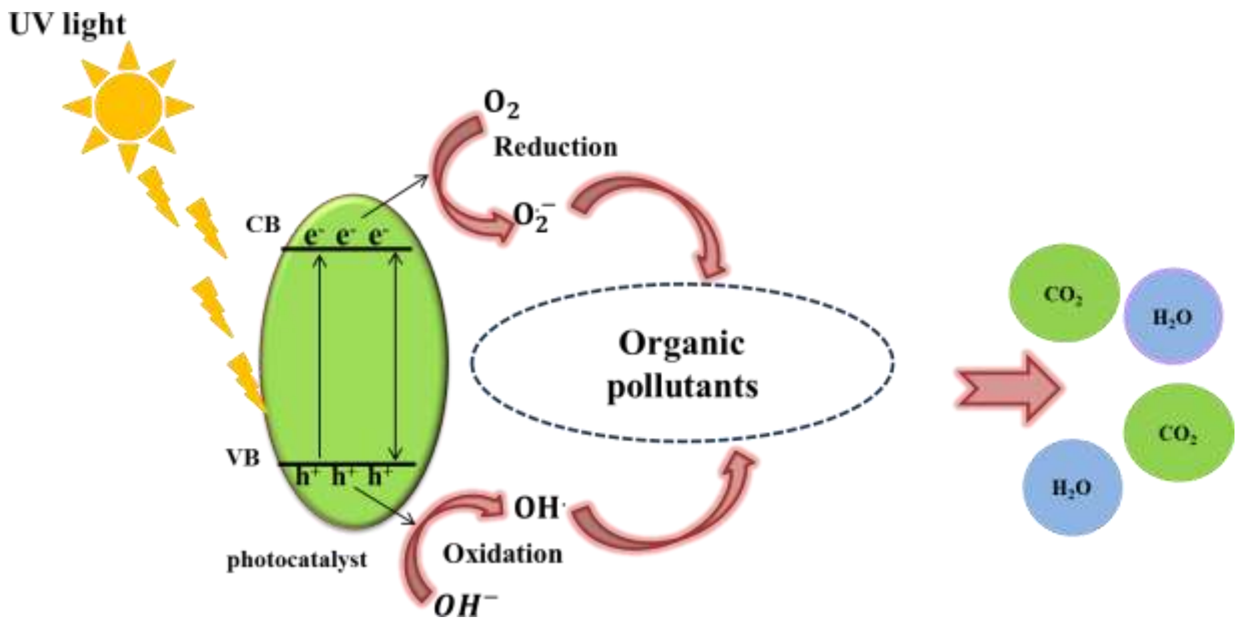

Figure 1: Mechanism of photocatalytic degradation

Photocatalysis has several benefits as an advanced oxidation process (AOP) for the destructionof organic pollutants. The technique exhibits versatility and efficiency, making it applicable to a diverse array of contaminants. The use of light as an energy source renders it a sustainable and renewable modality. Furthermore, the photocatalytic process takes place at ambient temperaturesand pressures, resulting in reduced energy demands in comparison to some other advanced oxidation processes (AOPs). In addition, it is possible to customize and enhance photocatalysts to target certain pollutants or fulfil specific applications [24].

3 Biochar Based Photocatalyst

3.1 Biochar

Biochar is a carbonaceous material that resembles charcoal and is generated by the pyrolysis process. For the process of pyrolysis, organic waste, such as agricultural leftovers, wood pieces, or even animal dung, is heated to high temperatures in an atmosphere devoid of oxygen [25]. Theprocess that was just described includes the thermal breakdown of the organic components,which ultimately results in the development of a material that is rich in carbon and has both a high porosity and a high level of stability. Improving the condition of the soil and removing excess carbon from the atmosphere are the two key functions that biochar serves. The aforementioned material acts as a soil additive that is ecologically responsible and has the ability to improve soil productivity, moisture retention, and nutrient absorption. As a direct consequenceof this, it is of considerable use in the field of agriculture [8]. In addition, the production of biochar is able to make use of a wide variety of feedstocks, including particular biomass crops, agricultural waste, and forestry residues, amongst other possibilities. Because of this property, biochar is a versatile and ecologically beneficial source of carbon that serves the twin objectiveof improving soil quality and making actions that sequester carbon easier to carry out [26].

Photocatalytic nanoparticles may be immobilized in a biochar matrix due to its porous nature. In addition to improving the photocatalysts' durability and recycling potential, this immobilization keeps the nanoparticles evenly dispersed and easily accessible during catalytic reactions [27]. Biochar's huge surface area also makes it effective in adsorbing impurities, which speeds up the process of cleaning the environment. Biochar photocatalysts may be used in a variety of contexts[28]. They can be used to degrade organic pollutants in wastewater treatment facilities, remove gases and particles from polluted air, and clean up polluted soil and groundwater [19, 29]. Furthermore, by altering the semiconductor nanoparticle type and biochar surface functionalization, these materials may be tailored to target certain contaminants [30]. Despite its potential, optimizing biochar photocatalysts for industrial applications and guaranteeing their long-term stability remain significant hurdles [31]. Ongoing research endeavors in this particular domain are mostly focused towards enhancing the efficiency, cost-effectiveness, and durabilityof these pioneering materials [32]. In conclusion, the utilization of biochar in conjunction with photocatalysts presents a viable and auspicious approach, whereby it may be synergisticall integrated with other catalytic substances such as metal oxides (such as TiO_2 [33], Fe_2O_3 [34], ZnO [35], $BiVO_4$ [36]) and metal sulfides (such as ZnS [37], CdS [38] and MoS_2 [39]) for tackling environmental pollution, offering a green solution that harnesses renewable solar energyto combat pollution effectively and reduce the environmental footprint of remediation processes.

Conclusion

Biochar-based photocatalysts, incorporating metal oxides, sulphides and other photocatalyst, represent a groundbreaking approach for the degradation of organic pollutants. These materials offer a sustainable and efficient solution to the pressing issue of environmental pollution. By combining the ancient wisdom of biochar with modern nanotechnology, these photocatalysts have shown remarkable promise in various applications, including wastewater treatment, soil and groundwater remediation, and air purification.

References

1. Natarajan, S., H.C. Bajaj, and R.J. Tayade, *Recent advances based on the synergetic effect of adsorption for removal of dyes from waste water using photocatalytic process.* Journal of Environmental Sciences, 2018. **65**: p. 201-222.
2. Xue, Y., et al., *Immobilization of photocatalytic materials for (waste) water treatment using 3D printing*

technology–advances and challenges. Environmental Pollution, 2022: p. 120549.
3. Toan, T.Q., et al., *Ultrasonic-assisted synthesis of magnetic recyclable Fe 3 O 4/rice husk biochar based photocatalysts for ciprofloxacin photodegradation in aqueous solution.* RSC advances, 2023. **13**(16): p. 11171-11181.
4. Zhang, H., et al., *Recent development of sludge biochar-based catalysts in advanced oxidation processes for removing wastewater contaminants: A review.* Fuel, 2023. **348**: p. 128444.
5. Yuan, X., et al., *Recent advancements and challenges in emerging applications of biochar-based catalysts.* Biotechnology Advances, 2023: p. 108181.
6. Mian, M.M. and G. Liu, *Recent progress in biochar-supported photocatalysts: synthesis, role of biochar, and applications.* RSC advances, 2018. **8**(26): p. 14237-14248.
7. Qian, S., et al., *Biochar-compost as a new option for soil improvement: Application in various problem soils.* Science of The Total Environment, 2023. **870**: p. 162024.
8. Kurniawan, T.A., et al., *Challenges and opportunities for biochar to promote circular economyand carbon neutrality*. Journal of environmental management, 2023. **332**: p. 117429.
9. Eddy, D.R., et al., *Heterophase polymorph of TiO2 (Anatase, Rutile, Brookite, TiO2 (B)) for efficient photocatalyst: fabrication and activity.* Nanomaterials, 2023. **13**(4): p. 704.
10. Mutalib, A.A. and N. Jaafar, *ZnO photocatalysts applications in abating the organic pollutant contamination: A mini review.* Total Environment Research Themes, 2022: p. 100013.
11. Saeed, M., et al., *Synthesis of a CoO–ZnO photocatalyst for enhanced visible-light assisted photodegradation of methylene blue.* New Journal of Chemistry, 2022. **46**(5): p. 2224-2231.
12. Wang, Z., B. Mei, and J. Chen, *Removing semiconductor-cocatalyst interfacial electron transfer induced bottleneck for efficient photocatalysis: A case study on Pt/CdS photocatalyst.* Journal of Catalysis, 2022. **408**: p. 270-278.
13. Isac, L. and A. Enesca, *Recent Developments in ZnS-Based Nanostructures Photocatalysts for Wastewater Treatment.* International journal of molecular sciences, 2022. **23**(24): p. 15668.
14. Zhang, S., et al., *Low-cost bauxite residue-MoS2 possessing adsorption and photocatalysis ability for removing organic pollutants in wastewater.* Separation and Purification Technology, 2022. **283**: p. 120144.
15. Zhu, J., et al., *One-pot hydrothermal synthesis of MoS2 modified sludge biochar for efficient removal of tetracycline from water.* Journal of Water Process Engineering, 2022. **49**: p. 103089.
16. Rangarajan, G., A. Jayaseelan, and R. Farnood, *Photocatalytic reactive oxygen species generationand their mechanisms of action in pollutant removal with biochar supported photocatalysts: A review.* Journal of Cleaner Production, 2022. **346**: p. 131155.
17. Cai, X., et al., *Titanium dioxide-coated biochar composites as adsorptive and photocatalytic degradation materials for the removal of aqueous organic pollutants.* Journal of Chemical Technology & Biotechnology, 2018. **93**(3): p. 783-791.
18. Bhavani, P., M. Hussain, and Y.-K. Park, *Recent advancements on the sustainable biochar based semiconducting materials for photocatalytic applications: A state of the art review.* Journal of Cleaner Production, 2022. **330**: p. 129899.
19. Lyu, H., Q. Zhang, and B. Shen, *Application of biochar and its composites in catalysis.* Chemosphere, 2020. **240**: p. 124842.
20. Ye, S., et al., *Facile assembled biochar-based nanocomposite with improved graphitization for efficient photocatalytic activity driven by visible light.* Applied Catalysis B: Environmental, 2019. **250**: p. 78-88.
21. Li, H., et al., *An investigation of the biochar-based visible-light photocatalyst via a self-assembly strategy.* Journal of environmental management, 2018. **217**: p. 175-182.
22. Liu, H., C. Wang, and G. Wang, *Photocatalytic advanced oxidation processes for water treatment: recent advances and perspective.* Chemistry–An Asian Journal, 2020. **15**(20): p. 3239- 3253.
23. Pandis, P.K., et al., *Key points of advanced oxidation processes (AOPs) for wastewater, organic pollutants and pharmaceutical waste treatment: A mini review.* ChemEngineering, 2022. **6**(1): p. 8.
24. Ren, L., et al., *Photocatalytic mechanisms and photocatalyst deactivation during the degradationof 5-fluorouracil in water.* Catalysis Today, 2023. **410**: p. 45-55.
25. Wang, J. and S. Wang, *Preparation, modification and environmental application of biochar: A review.* Journal of Cleaner Production, 2019. **227**: p. 1002-1022.
26. CHENG, H., S. Yang, and N. BOLAN, *Biochar for future and futuristic biochar.* Pedosphere, 2023.
27. Zhao, C., et al., *Review of Advances in the Utilization of Biochar-Derived Catalysts for Biodiesel*

Production. ACS omega, 2023. **8**(9): p. 8190-8200.

28. Shan, R., et al., *A review of recent developments in catalytic applications of biochar-basedmaterials.* Resources, conservation and recycling, 2020. **162**: p. 105036.
29. Kang, K., S. Nanda, and Y. Hu, *Current trends in biochar application for catalytic conversion of biomass to biofuels.* Catalysis Today, 2022.
30. Zhang, S.-Z., et al., *Biochar based functional materials as heterogeneous catalysts for organic reactions.* Current Opinion in Green and Sustainable Chemistry, 2022: p. 100713.
31. Kumar, A., K. Saini, and T. Bhaskar, *Advances in design strategies for preparation of biochar based catalytic system for production of high value chemicals.* Bioresource technology, 2020. **299**: p. 122564.
32. Li, Y., et al., *A critical review of the production and advanced utilization of biochar via selective pyrolysis of lignocellulosic biomass.* Bioresource Technology, 2020. **312**: p. 123614.
33. Zeshan, M., et al., *Remediation of pesticides using TiO2 based photocatalytic strategies: A review.* Chemosphere, 2022: p. 134525.
34. Xu, H.-Y., et al., *Mechanism insights into the enhanced photocatatlytic peroxydisulfate activationby Fe3O4/BiOI heterojunction.* Materials Science and Engineering: B, 2023. **294**: p. 116509.
35. Manohar, M., et al., *ZnO Nanocomposites in Dye Degradation.* Advanced Oxidation Processes in Dye-Containing Wastewater: Volume 2, 2022: p. 317-341.
36. Akhter, P., et al., *Montmorillonite-supported BiVO4 nanocomposite: synthesis, interface characteristics and enhanced photocatalytic activity for dye-contaminated wastewater.* Journal of Industrial and Engineering Chemistry, 2023. **123**: p. 238-247.
37. Kanakaraju, D. and A. Chandrasekaran, *Recent advances in TiO2/ZnS-based binary and ternary photocatalysts for the degradation of organic pollutants.* Science of The Total Environment, 2023. **868**: p. 161525.
38. Das, S. and Y.-H. Ahn, *Synthesis and application of CdS nanorods for LED-based photocatalytic degradation of tetracycline antibiotic.* Chemosphere, 2022. **291**: p. 132870.
39. Mohammed, R., et al., *Reusable and highly stable MoS2 nanosheets for photocatalytic, sonocatalytic and thermocatalytic degradation of organic dyes: Comparative study.* Nano- Structures & Nano-Objects, 2022. **31**: p. 100900.
40. Cui, J., et al., *Recent progress in biochar-based photocatalysts for wastewater treatment: synthesis, mechanisms, and applications.* Applied Sciences, 2020. **10**(3): p. 1019.

Analysis of Camshaft Failure - A Review

Muhammad Hammad Khaliq
Department of Mechanical Engineering
University of Engineering and Technology
Taxila, Pakistan

Ahmad Suleman
Department of Mechanical Engineering
University of Engineering and Technology
Taxila, Pakistan

Muhammad Saim
Department of Mechanical Engineering
University of Engineering and Technology
Taxila, Pakistan

Muhammad Luqman
Department of Mechanical Engineering
University of Engineering and Technology
Taxila, Pakistan

Ahmad Shahzad
Department of Mechanical Engineering
University of Engineering and Technology
Taxila, Pakistan

Ghina Fatima
Department of Mechanical Engineering
University of Engineering and Technology
Taxila, Pakistan

Abstract:- A review of static, structural still as model study of engine camshafts is included in the article below. The Camshaft is nothing more than an important component found in the engines of cars and other uses. The camshaft is crucial to the efficient and smooth operation of engines. The project's objective is to model and analyze the camshaft using FEM. Today's top camshaft producers have created a variety of cam profile designs with the aim of achieving a positive and effective engine performance. Due to the high load and high speed involved in engine operation, it is essential to examine engine component failure under such simultaneous stress. Numerous studies have been published to far on the failure of engine components. Various pieces of software are used to accomplish the research, with ANSYS perhaps being the most well- liked in the present day.

The mechanism tremors as the consequence of the crankshaft's perpetual exposure to high speed rotational action. It is a tool used to run engine valves at the proper opening and shutting times. They are also exposed to various contact fatigue loads due to the contact between the plunger and the cam. The shaft will vibrate and wear prematurely as a result of these fluctuations in loads and velocity.

With the objective to enhance safety while also taking into account the member's lifespan, models and fatigue analysis must be used to the camshafts. An engine camshaft model was established using a numerical finite element methodology in order to accomplish the aforementioned investigation of the engine camshaft for this thesis. The camshaft originated in CATIA software, and after the contrary, it was placed in a STEP file for additional inquiry. Then, by spooling this model in the ANSYS computer, the natural frequency, mode shapes, and alternative fatigue stresses of the camshaft portion are established.

Keywords: - *Stress Analysis, Modal Analysis, Fatigue analysis, Finite Element Analysis, ANSYS, Characteristics*

INTRODUCTION

Components are simply mechanisms that may be utilized in engine valve systems to directly convey a certain activity to their adherents. The cam serves as the driver and the follower serves as the driven element in this pair of cams and adherents. A preferable pair with line contact would be a cam and follower system.

The Camshaft, which contains propeller face, enduring journals, and cam prongs to restrict the mechanism's undesired movements, is nothing less than the key component of the engine valve mechanism. The intake & valve are worked by the camshaft in accordance with the timing of the engine's strokes employing motion transmission through direct contact. If the movements are not transferred properly, the valve timings will be immediately impacted, which will decrease the engine stroke efficiency. All actions linked to this mechanism are carefully examined, analyzed, and constructed in order to provide exact work from the camshaft. Instead of maincomponents, camshafts also include smaller componentslike tappets, rocker arms, and push rods. The crankshaftaids in the operation of the camshaft in this system. synchronizing a few cogs that time catalyst pulses. In order to decide the engine's firing order, the vibration will be communicated to a number of ignition valves when it is received by the camshaft.

Regarding the malfunction, strain concentration insidegeometric features like cavities, fractures, cuts, and edges isa frequent sign of premature failure of the camshaft's connected elements. Adaptability and high-cycle fatigue attributes are also evident. Among the prevalent causes of camshaft failure are contact fatigue, inadequate lubrication, and cam wear. It is vital for assessing the phenomenon of fatigue in order to identify the factors contributing to failureas a result of exhaustion. Therefore, it will be destroyed. Predicting failures and Significant goals comprise prolonging the camshaft's functional lifespan for the many specialists involved in the enquiry and creation team.

The effectiveness of the camshaft depends on several factors. Cam specs, lift shape, valve train composition, and diverse production methods are a few of them. The endeavors being made by several manufacturing sectors to assess and improve the effect of abrasion on the camshaft's durability are noteworthy. To obtain the requisite surface polish and lift profile, the grooves of the camshaft are carefully machined. Thus, it is discovered that the grinding approach used (offensive, conservative, or mild) affects the camshaft's service life. The production and grinding of camshafts both entail several procedures. Thermal stresses created during camshaft grinding result in thermal damage to the camshafts, which reduces their output rates. Thus, to achieve high rates of production with greater efficiency, itis crucial to have a seamless connection between the grinding process and the technical design of camshaft. After those camshafts were made experimentally in the foundry, this planning was examined using casting simulation software.

EMPERICAL ASSESSMENT

Multiple academic articles on analysis of failure of the camshaft assembly are evaluated. A.S. Dhavale and et.al.[1] In order to design effective mechanism connections, the dynamic behavior of the components, including the mathematical behavior of the physical model, must be taken into account. This was explored throughout this article's modeling and fracture analysis of the camshaft. Here, two dynamic models of cam supporter frameworks for large, single-level prospects and varying levels of flexibility are given and examined. As stated by Bayrakceken et al. [2] They discussed the crack assessment of a nodular cast-iron camshaft assembly in their paper. After a shockingly little duration of driving, the examined camshaft fractures. To identify the root of the failure, the microstructure and chemical nature of the camshaft material are studied. Several fractographic tests are used to assess the fracture situations. The finite element method also applies stress analysis to identify the areas of the camshaft that are subject to high stress.
Dr P.s. Chauhan and et.al.[3] This study has explored the camshaft assembly of multiple substances with varying synthesis options, as analyzed using finite elements. FEA analysis and camshaft sketching are carried out using SolidWorks and ANSYS Software, respectively. G. Wanga, D. Taylor and et.al.[4] During the testing and modeling phases of this research, grey cast-iron camshafts used in Rover cars were subjected to cyclic bending and torsion. A novel approach presented as crack modeling was trained to

anticipate the exhaustion threshold. This method calculates a uniform stress intensity index (K) for the amount of tension in sections using a linear elastic finite element analysis. Levent Cenk Kumruoğlu and et.al.[5] In the assessment, the solidification, cooling rate, and metal flow were evaluated experimentally and statistically in relation to the mechanical and metallographic characteristics of camshafts made from chilled cast iron. First off, the entire casting approach was assisted by 3-dimensional sketching and elegance programs. Li Fengjun, Cai Anke and et.al.[6] A too significant chilling trend was present in the transition zone during the study that led to the fracture failure of the camshaft. Visual section characteristics indicate that the fracture zone is virtually white, has a ledeburite microstructure, and is also exceedingly hard. Mutukula Pavan Kumar and et.al.[7] Camshaft modeling and analysis are finished inside the research. Solid Works 2016 design program is used to model a camshaft. Ansys Workbench 16.0 employs static analysis. Materials used include 42CrMo4 (special alloy steel), Aluminum Silicon Magnesium Alloy, and Magnesium Alloy. The applied load is 850N. Stress, deformation, and strain in structures are investigated and tabulated. Santosh Patil, S. F. Patil and et.al.[8] This paper looked at The system shakes because of the fast camshaft spin. Camshafts are susceptible to various impact degradation stresses because the lever makes friction with the cam. These variances cause the shaft to vibrate and become worn out. Therefore, to assure safety and establish the individual's lifespan, modal and fatigue analysis should be used to the camshafts. The aforementioned study was carried out in this work using a numerical finite element method and the camshaft model. For further study, the camshaft was modelled in CATIA software and exported inSTEP format. Then, using ANSYS software, the camshaft member's inherent frequency, mode shapes, and alternate stresses were induced..

S.G.Thorat, Nitesh Dubey and et.al.[9] Using finite element analysis, they designed and analyzed the camshaft for this paper. The task's objective is to show and examine the camshaft under FEM in order to plan it diagnostically. In FEM, the camshaft's behavior is determined by the behavior of the components combined, influencing the cam to shaft robustness under the lightest possible load scenarios. Samta Jain and others (10) The stationary skeletal and acoustical analyses of the combustion chamber camshaft were studied in this work using ANSYS software. The static structural analysis, modal analysis, and enginecamshaft modeling are all included in this work. the The camshaft is one of the most important parts of the enginesin cars and other vehicles. High speed rotation of this camshaft stresses and vibrates the system. Because the levermakes friction with the cam, camshafts are vulnerable to different contact degradation stresses. Camshafts are revolving parts that carry a heavy weight. To prevent camshaft failure, these precise parameters must be established.

Uma Mahesh and et.al.[11] This work examined the finite element structural analysis and computational geometric modeling of automotive camshafts. In this project, an automobile camshaft is created using numerical calculations, followed by modeling using three different materials in CATIA and CAE(Structural) Analysis in ANSYS-WORKBENCH. Determine which material will provide the optimum performance for the camshaft by comparing cast iron, steel, and ALMMC.

Vivekanandan.Pa and et.al.[12] They performed modeling, The camshaft's geometry and evaluation of finite elements throughout this investigation. The research's objective is tosimulate the camshaft's design and analysis. In FEM, thebehavior of the camshaft is determined by examining theweather's overall behavior in order to design the camshaftstrong enough to withstand the fewest load instances. Thisstudy may be essential for determining the ideal camshaftsize and understanding the Volatile behaviors of thecamshaft. Wanjari and et.al.[13] This paper investigated the failure of the camshaft. They learned that single and doubleunderneath cranks are two distinct configurations. Theyclaimed that only engines with four or more valves per cylinder normally employ single heads in double underneath configurations, which have two cranks.

OUTCOMES

- There are many variables, comprising material characteristics engine speed, engine load, grease parameters, etc., that contribute to camshaft failures.
- Camshaft failure circumstances are largely identifiedthrough study of the relevant failure metrics in order

to prevent camshaft failure.

- Vibrations inside the system are caused by the high-speed rotating movement that camshafts experience under varying loads. Because the plunger and cam arein live contact, the camshafts are also susceptible to variable contact fatigue stresses. These variations leadto vibration and fatigue problems on the shaft.
- The research was performed using a computer finiteelement approach on a model of an engine camshaft. The natural frequency and different stress levels that emerge in camshafts during operation are then defined using the ANSYS program.
- ANSYS can quickly and virtually collaborate with manysophisticated engineering processes. The ANSYS technology integrates cutting-edge engineeringtechniques and CAD technologies to produce exceptional automation and performance.

CONCLUSIONS

Below is a summary of the arguments drawn from theabove dissertation:

- The camshaft plays a substantial influence on fuel economy by increasing the accuracy and efficacy of valve timing and maintaining the engine's favorable firing sequence.
- In this thesis, we looked at camshaft failures and the impact those failures had on engine performance. Concentrations of topological stress, changes in vehicle weights and velocity, drowsiness material deterioration, or other declining are the main causes of camshaft failure. Additionally, we sought to increase the camshaft's operational life by reducing the likelihood offailure.
- All the elements that contribute to camshaft failure must be taken into account and analyzed before the camshaft is designed in order to forecast and prevent early failure. Any breakdown may potentially be caused by vibration. Therefore, in order to analyze and correct vibration and resonance phenomena, it is necessary to ascertain the natural frequency.
- ANSYS software was used for the modal analysis in this thesis. the ANSYS module's calculation of the alternating stress. It is usually customary to compare theresults of software analysis to theoretical stress levels.

REFERENCES

[1]. Study of Modelling and Fracture Analysis of Camshaft: A Review, A.S.Dhavale, V.R.Muttagi,International Journal of Engineering Research and Applications, Vol. 2, Issue 6, pp. 835-842,2012.

[2]. Fracture analysis of a camshaft made from nodularcast iron, Bayrakceken, I. Ucun, S. Tasgetiren, Engineering Failure Analysis, Vol. 13, pp. 1240-1245,February 2006.

[3]. Finite Element Analysis of NCI, GCI, AND EN 18 Materials Camshaft, Dr P.S. Chahuan and Juber Hussain, European Journal of Mechanical EngineeringResearch Vol.5, No.2, pp.24-34, May 2018.

[4]. Prediction of fatigue failure in a camshaft using the crack modelling method, G. Wanga, D. Taylor, B.Bouquina, J. Devlukiab, A. Ciepalowicz, Engineering Failure Analysis 7 (2000) 189-197,2000.

[5]. Materials and Design, Levant Cenk Kumruog˘lu, Materials and Design 30 (2009) 927–938,15 July 2008.

[6]. Fracture analysis of chilled cast iron camshaft, Li Ping, Li Fengjun, Cai Anke and Wei Bokang, Feb 2009.

[7]. Modeling and analysis of camshaft, Mutukula Pavan Kumar, International Journal of Research in Advance engineering Technologies, Volume 6, Issue 3 May 2018.

[8]. Modal and Fatigue Analysis of a Camshaft using FEA, Santosh Patila,b, S. F. Patilb and Saravanan Karuppanana, International Journal of Applied Engineering Research ISSN 0973-4562 Volume 8, Number 14 (2013) pp. 1685-1694,2013.

[9]. Design and Analysis of Camshaft, S.G.Thorat, Nitesh Dubey, Arvind Shinde, Pushkar Fulpagare, Manish Suryavanshi, Proceedings of 11th IRF International Conference, 15 June 2014, Pune, India.

[10]. Static Structural and Modal Analysis of Engine Camshaft using ANSYS Software, Samta Jain, Vikas Bansal, International Journal of Engineering Technology, Management and Applied Sciences, (Volume 4, Issue 5, ISSN 2349-4476),2016.

[11]. Computational geometric modelling and finite element structural analysis of automobile camshaft Uma Mahesh, Bhaskar Reddy, Jaya Kishore, International Journal of Emerging Technology and Advanced Engineering, (ISSN 2250-2459, ISO 9001:2008

Certified Journal, Volume 5, Issue 7, July 2015).

[12]. Modelling, Design and Finite Element Analysis of Cam Shaft, Vivekanandan.Pa, Kumar. Mb, International Journal of Current Engineering and Technology (ISSN 2277 – 4106),2013.
[13]. Failure of Camshaft, Wanjari R. V. and Parshiwanikar
T. C., International Journal of Innovative Technology and Exploring Engineering, Vol. 2, Issue 6, pp. 248250,2013.

Experimental Study of Tensile Behavior for Hybrid Double Strap Joint using Different Adhesives

Shahid Iqbal
Mechanical Engineering Department
Wah Engineering College, UW
Wah Cantt, Pakistan
shahid.iqbal@wecuw.edu.pk

Abdul Manan
Mechanical Engineering Department
Wah Engineering College, UW
Wah Cantt, Pakistan
abdulmananmalik99@gmail.com

Muhammad Ahmed
Mechanical Engineering Department
Wah Engineering College, UW
Wah Cantt, Pakistan
ahmedmehmoodeng@gmail.com

Shahzaib Khan
Mechanical Engineering Department
Wah Engineering College, UW
Wah Cantt, Pakistan
khanshahzaib2021@gmail.com

Muhammad Abdullah
Mechanical Engineering Department
Wah Engineering College, UW
Wah Cantt, Pakistan
ak1425278@gmail.com

Muhammad Yasir
Mechanical Engineering Department
Wah Engineering College, UW
Wah Cantt, Pakistan
muhammad.yasir@wecuw.edu.pk

***Abstract*— Carbon fiber reinforced polymer hybrid double strap are extensively used in the field of aviation and automotives due to light weight, high strength and longer fatigue life. In this research study, an experimental investigation has been carried out of the hybrid double strap joint between carbon fiber reinforced polymer and aluminum alloy 6061-T6 using different adhesives. Two different epoxies thermosetting epoxy araldite LY5052 with aradur H5052 and thermoplastics epoxy polyurethane mixed with tetrahydrofuran were used for the fabrication of hybrid double strap joints. These specimens were prepared using hand layup method. A number of forty specimens were fabricated using both adhesives. Twenty specimens were fabricated using Thermosetting epoxy araldite LY5052 with aradur H5052 and twenty with thermoplastic epoxy polyurethane with tetrahydrofuran. Tensile experiments were performed to evaluate the elongation properties of the joints using UTM Machine. The results indicated that the static strength of thermosetting hybrid joint in which epoxy Araldite LY5052 with Aradur H5052 was 19.53 KN as compared to thermoplastic adhesive joint for which the value was 8.22 KN. The high static strength of thermosetting hybrid joint is due to the strong bonding of the adhesive. Furthermore, the microscopic failure modes revealed that the mode of failure for the joints was cohesive and mix mode failure.**

Keywords—Static Strength, Hybrid Joint, Double strap joint, Araldite LY5052, Polyurethane, Fractography.

Introduction

Composites materials are being used widely in many engineering structures due to their improved mechanical properties, better specific strength and light weight. Nowadays, new composites are increasingly used in automobiles, aerospace, railway industry and in many engineering structures [1-5]. Metals, Ceramics, polymers, rubber and combinations of these materials can be effectively bonded together using different adhesives [6]. However, these materials must be joined together based on their specific properties [7]. Metallic and new composites materials (dis-similar materials) adhesively bonded joints are being widely used for the fabrication of wing and fuselage in aerospace industry due to low cost and weight to fuel ratio [8,9]. Adhesive joints have been receiving huge attention due to their advantages over traditional bonding methods owing to lighter structures and reduced stress concentrations [10]. Adhesive bonding has emerged as a replacement for mechanical fastening in the assembly of composite and metal components, offering a new approach to joint assembly. Mechanically fastened joints, fabricate through bolts or rivets, tend to create high stress concentration results to a decrease in overall structural integrity. This phenomenon has been discussed in previous research [11–13] whereas, the adhesive joints show uniform distribution of stresses. The strength of the joint assembly is influenced by critical factors including the choice of adhesive, patch length, fiber patch thickness, and adherent strength. Zheng Y, Zhang C, Ying Ti, Xu Wa And Mingkun Li extensively explores the elongation characteristics of two double strap hybrid joints by utilizing two different adhesives with different patch length and rivets end distance because there is lack of experimental data of hybrid joints in literature [13]. Stress distribution in hybrid and rivetted joint has been investigated through simulation [15]. The properties and performance of the adhesive, fracture energy and stress bearing capacity have been investigated by [16]. In this study, CFRP/ steel single lap joints were investigated on the basis of static strength using different adhesives. Two different types of adherents, 3 different adhesives with different thickness were used to analyzed the mechanical behavior of the joint. It was concluded that, joint static strength and fracture energy has been affected by adhesive type and thickness. Ductile adhesive has stronger bond capacity as compared to thin adhesive layer thickness and longer effective bond length [17]. Yu Du and Lu Shi [18] proposed an experimental analysis of composites/ steel hybrid joint for finding tensile and fatigue strength of the joint and it was concluded that joint strength and performance depends upon the nature of adhesive and the applied force. Yogesh and N. Arunkumar [19] introduced three different methods for the fabrication of Single lap joint: adhesive bonding, mechanical fastening and hybrid bonding. The joint durability and failure strength was determined through tensile testing it was concluded that adhesive bonding has high strength as compared to mechanical fastening for acrylic-based adhesive. The behavior of axially loaded steel plates which are externally bonded with CFRP on both sides with variable bond lengths. The results are evaluated from both experimental and FE technique. It was concluded that failure always occurs in bonding between steel plates and carbon fiber reinforced polymers [20]. Campilho et al. [21] conducted FEA and experimental study of single and double strap joints under compression loading with variable overlap lengths and patch thicknesses between carbon epoxy laminates. The laminate patches were fabricated with hand layup between CFRP and epoxy. Each ply thickness is 0.15mm and total CFRP specimen thickness is 2.4mm with hole of 10mm diameter. The analysis carried out in relation of elastic stiffness and strength of bond. Depending on these factors double strap lap joint with strap lengths and patch thickness 15mm, 10mm and 1.2mm, 2.4mm respectively shows best results also single strap joint with patch length of 15mm show good results.

Rachid, M., et al. [22] studied FEM approach to investigate the effects of adhesive thickness and shape of patch of composites on the joint which has been used in aerospace industry where base metal was aluminum and repair patch material wass unidirectional boron/epoxy composite. It was concluded that rectangular shape patches could improve the strength and It also reduces the adhesive stresses. Selection of adhesives with and best appropriate surface treatment has been considered a challenge for adhesive bonding of fiber metal laminates. in this research the adhesives are epoxy and polyurethane and adherents are polymeric matrix with carbon fiber and aluminum. Results concluded in the form of high mech. Resistance and low adhesive failure in this respect for epoxy sanded and peel ply with composite and sandblasting with aluminum is best option on other hand for polyurethane sanded, peel ply and sandblast with composite and sanded, sandblast with aluminum is best option [23]. Moussavi-Torshizi, S. Ebrahim, Soheil Dariushi, Mojtaba Sadighi and Pedram Safarpou [24] investigated the tensile strength of FML's where metal is aluminum and unidirectional two types of fibers were used with combination of different orientations. Modified classical laminate theory was used to find the stress strain behavior of FML's using FEM modeling. It was concluded that fibers with zero orientation show best results in form of modules of elasticity, yield and ultimate stress. It was also observed that the orientation of Kevlar plays a vital role in FML's strength under tensile loading. Da Costa Mattos, H.S, A.H. Monteiro, and R. Palazzetti [25] proposed practical formulas for carbon/epoxy composite with adhesive single lap bonded joint as simple, safe and reliable with the effect of different overlap length correlated with FEM model under static and fatigue loading. The objective was to replace welded and solder joints with adhesively bonded joints where spark and heat is not allowed such as in offshore application. Result shows as the overlap length of bond increased its strength was also increased. LI, X. et al. [26] noted the tensile behavior of adhesive-bonded single lap hybrid joint and evaluate wide application in engineering practice because research focused on hybrid adhesive joints is currently in its preliminary phase. This research examines the static properties of a hybrid single lap joint and it was concluded that the tensile strength is increased due to the presence of rivets and fillets in the joint.

An extensive literature [15-26] has been reported on single and double lap adhesive joint, hybrid joints and mechanical bolted joint and a few were conducted on thermosetting adhesive hybrid adhesive joints. However, there is no published research available for finding the tensile behavior of hybrid double strap joint between reinforced fiber composite and metal (aluminum alloy 6061-t6 and carbon fiber reinforced polymer) using thermosetting and thermoplasties adhesives (araldite 5052 with aradur 5052 hardener and polyurethane mixed with tetrahydrofuran). The novel approach explored during this research study, is the comparison between thermosetting and thermoplastics adhesives for finding the tensile strength of hybrid double strap joints. These two different adhesives were used for the preparation of specimens by using hand layup method, which is relatively cost-effective, instead of using autoclaves. Tensile test was carried out to determine the failure load. Furthermore, the fractographic analysis of these joints was also conducted using optical microscope.

Experimental Procedure

Materials

High strength aerospace grade aluminum alloy plate having 5 mm thickness (Purchased from Aeromotive Technologies) was used for the preparation of hybrid double strap joint. The chemical composition of 6061-T6 aluminum alloy is shown in Table 1.

TABLE 1 CHEMICAL PROPERTIES OF 6061-T6 ALLOY

Element	Mg	Cu	Si	Cr	Mn	Fe	Zn	Ti	Al
Weight Percentage	1.26	0.4	0.8	0.38	0.15	0.8	0.25	0.15	Bal

Woven Carbon fiber TC-33(3K) (Purchased from Aeromotive Technologies) having a diameter of 5–10 µm with high strength-to-volume ratio was used in this study. For bonding of adherends (6061-t6) and Carbon fiber reinforced polymer (TC-33K), Two different adhesives particularly used for the manufacturing and repairing of aircraft, used in this study. First consists of Araldite LY5052 epoxy resin and Aradur 5052 hardener [27]. The Second one was Polyurethane mixed with tetrahydrofuran resin [28]. Mechanical properties of alloy 6061-T6, carbon fiber and adhesives are presented in Table 2 [29,30].

TABLE 2 MECHANICAL PROPERTIES OF 6061-T6 ALLOY AND CARBON FIBER TC-33K

Material	Ultimate Tensile Strength (MPa)	Elastic Modulus (GPa)	Poisson Ratio
Aluminum 6061-T6	310	69	0.33
Woven Carbon Fiber TC-33	3450	230	0.35

The Tensile strength of Araldite 5052 is 102 MPa and Polyurethane adhesive strength 42 MPa.

Test specimen preparation

The schematic diagram of hybrid DSJ test specimen with dimensions is shown in Fig. 1(a). The laminates were prepared using Aluminum Alloy 6061-T6 and Woven Carbon Fiber TC-33(3K) with Epoxy Araldite LY 5052 and Aradur 5052, along with Polyurethane mixed with tetrahydrofuran resin, using the hand layup method. The Hybrid Double Strap Joints with one bolt were designed and fabricated according to ASTM-D 3528-96 [31] as shown in Fig. 1(b) and 1(c).

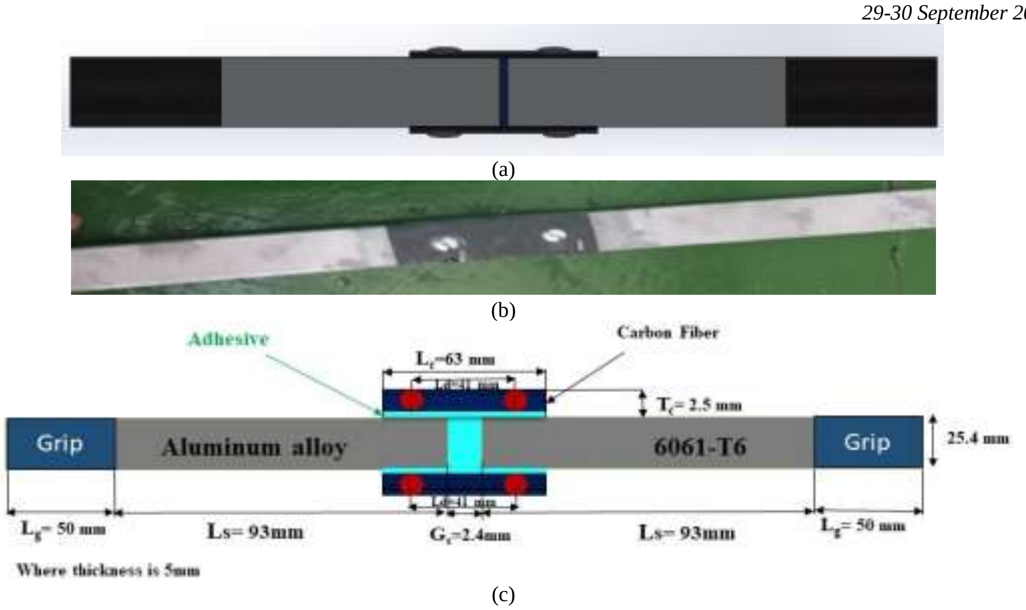

Fig. 1. (a) Schematic of hybrid double strap joint. (b) Final machined out hybrid ouble strap joint of CFRP/Aluminum alloy 6061-T6. (c) Configuration of hybrid double strap joint.

Fastening began with stainless steel SS 304 rivets. For the aluminum adherend, the bonding surface underwent sandblasting at 3 bar pressure, followed by polishing with 180 to 2000 mesh grade emery paper and cleaning with acetone. The hybrid joints were prepared using 5052 and polyurethane adhesives with a combination of rivets. The stepwise methodology of the specimen's preparation is presented in Fig. 2.

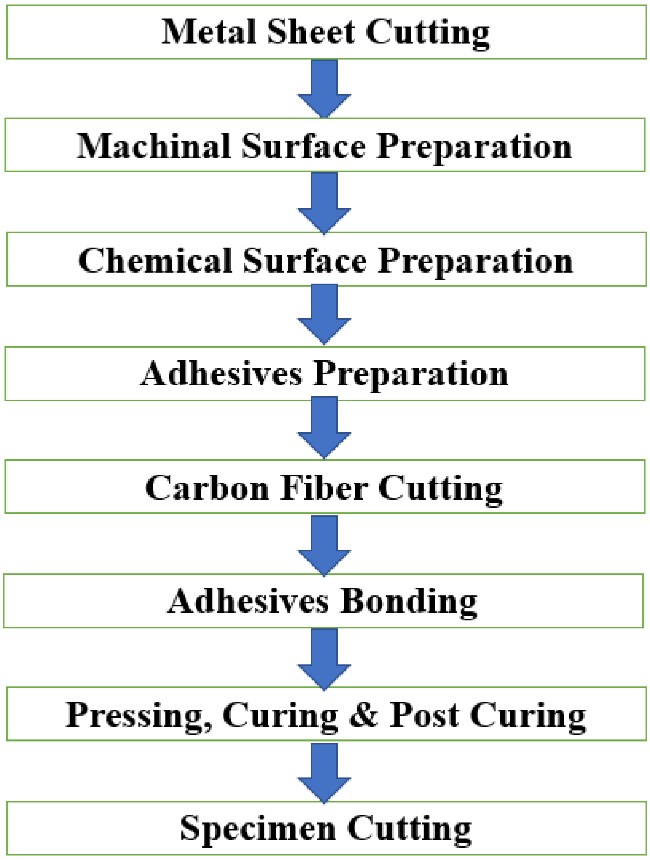

Fig. 2. stepwise methodology of Joint preparation.

Test Procedure

Tensile Testing

In order to find out the static strength of thermosetting and thermoplastics specimens, the static tests of both type of specimens were conducted on UTM machine (modal: SJ-10t) according to ASTM Standard [31]. During testing, all specimens were clamped on machine with fixed lower end and upper end check moves at a rate of 1.27mm/min. The distance between the check end and end of lap was 63mm and twenty specimens were testing with each type of joint. The tensile strength of the specimens was calculated using data obtained from data acquisition systems in the form of load and extension. UTM machine with test specimen is shown in Fig. 3.

]

Fig. 3 UTM machine with test specimen

The aim was to find out the tensile strength of the hybrid joint using thermosetting epoxy araldite LY 5052 and thermoplastic epoxy polyurethane. The static strength was investigated in the form of failure load and extension produced. A nearly linear correlation between the applied load and the resulting extensions for both adhesives can be observed from Fig. 4 (a) and it aligns with the findings presented in [32-36]. The thermosetting adhesive joint showed a maximum average bonding strength of 19.53 kN and stretched a maximum extension of 1.04 mm, whereas the thermoplastic adhesive joint attained values of 8.22 kN for bonding strength and 0.76 mm for extension. Araldite LY 5052 exhibits higher tensile strength compared to polyurethane (TPU) in hybrid joints for two reasons; Firstly, it possesses a homogeneous structure and secondly, the presence of air bubbles due to improper curing of polyurethane epoxy decreases the strength of hybrid joint [37-40]. The average failure load of thermosetting hybrid double strap joints is higher as compared to the thermoplastic joint as shown in Fig. 4(b). The experimental results are given in Table 3.

TABLE 3 FAILURE LOAD AND EXTENSION OF DIFFERENT ADHESIVES JOINTS

Type of specimen	Avg. Failure Load (KN)	Avg. deformation (mm)
Thermosetting Adhesive Hybrid DSJ	19.53	1.04
Thermoplastic Adhesive Hybrid DSJ	8.22	0.76

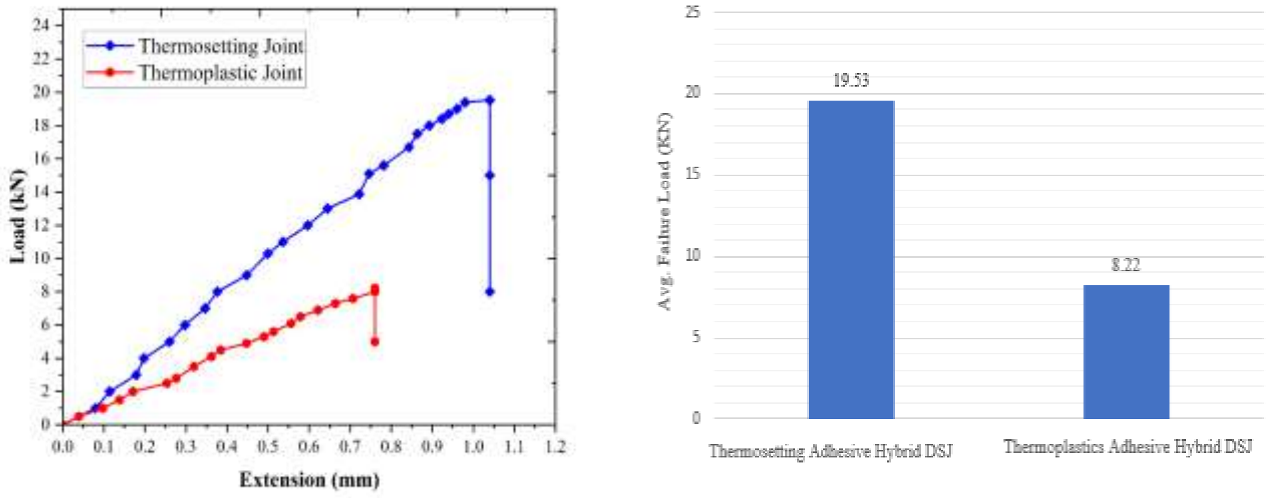

(a) (b)

Fig. 4. (a) Load-extension curve for tensile testing. (b) Average failure load for thermosetting and thermoplastics hybrid double strap joints.

Failure Modes

The failure mode in the case of thermosetting hybrid joints revealed both cohesive and mixed-mode failures, as clearly indicated by the noticeable detachment of CFRP at the bonded area as shown in Fig. 5. This mentions that the surface preparation techniques applied on the adherends were proper, while in certain area, there was a detachment between the CFRP and the adhesive, which resulted from a weak bond between the aluminum and carbon/epoxy laminates. Because the joints were fabricated using the hand layup technique, there is a possibility for adhesive shrinkage and presence of air bubbles in the adhesive that contributed for crack initiation within the CFRP layers. The progression of these cracks extended from the CFRP layers to the adhesive situated between the CFRP and aluminum sheets, ultimately leading to joint failure. Fractography results revealed that there was a cohesive and mixed mode failure.

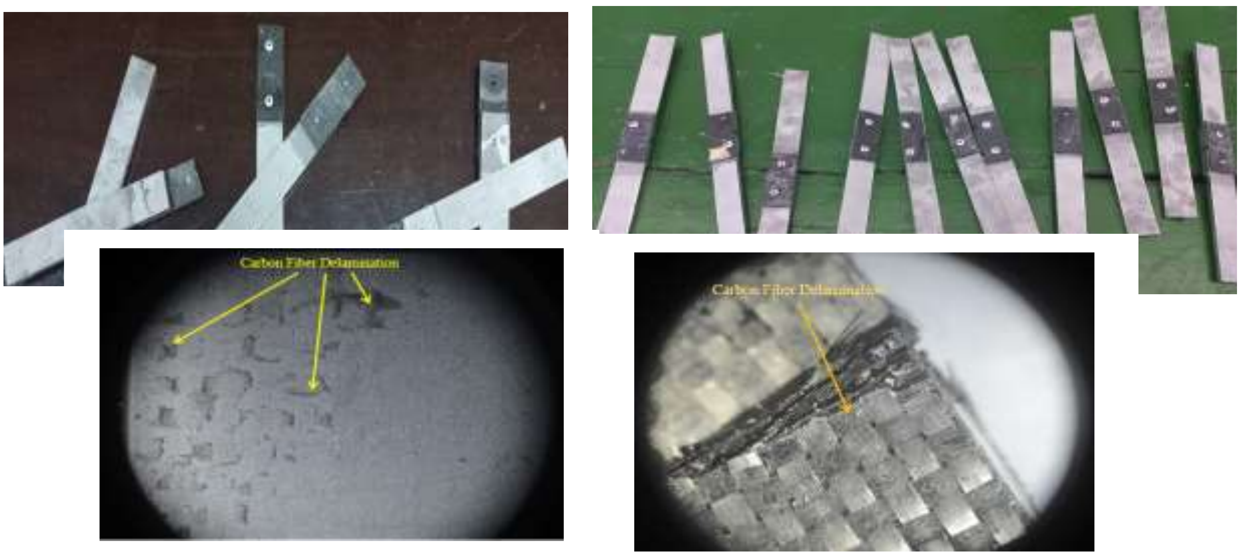

Fig. 5. CFRP delamination on fracture Surface of hybrid double strap Joint.

CONCLUSION

The objective of this research study was to investigate the static strength of hybrid double-strap joints between aluminum alloy 6061 and carbon fiber-reinforced polymer, utilizing Araldite 5052 and TPU polyurethane epoxy adhesives. Tensile testing and fractographic analysis were conducted to assess static strength and failure mechanisms. After conducting the experiments, several key findings emerged; Carbon fiber reinforced polymer hybrid joints bonded with Araldite 5052 exhibited a 37% higher elongation capacity compared to polyurethane epoxy hybrid joints, primarily attributed to the proper curing of thermosetting adhesive hybrid joints. The static strength in the form of failure load for thermoplastic polyurethane hybrid joints was found to be 58% lower than that of thermosetting hybrid joints. A difference in static strength was observed 76 % between thermosetting and thermoplastic hybrid joints. The deformation behavior of thermoplastic hybrid joints showed 27% lower elongation due to passive crack growth in the thermoplastic adhesive. The failure mode of both types of hybrid joints was characterized as a combination of cohesive and mixed-mode failures, owing to the clear detachment of Carbon fiber reinforced polymer from the aluminum alloy metal sheet.

Acknowledgment

The authors would like to express their gratitude to the Mechanical Engineering Department at Wah Engineering College for their generous support.

REFERENCES

H.K. Kim, E.T. Park, W.J. Song, B.S. Kang, and J. Kim, "Experimental and numerical investigation of the high-velocity impact resistance of fiber metal laminates and al 6061-T6 by using electromagnetic launcher" J. Mech. Sci, vol. 33, pp. 1219–1229, March 2019.

S. Iqbal, A. Tariq, W.A Khan, W Shahzad, M Azeem, W. Javid, H. Ali, M, Yasir, and M, Shakeel, "Comparative Analysis of Static and Fatigue Strength of Carbon Fiber and Al 6061-T6 Double Strap Joint" Mater. Trans, Vol. 63(8), pp.1120-1126, August 2022.

X,Li, W.Gao, and W.Liu, "Post-buckling progressive damage of CFRP laminates with a large-sized elliptical cutout subjected to shear loading" Compos. Struct, Vol. 128, pp.313-321. September 2015.

I. Benedetti, and V.Gulizzi, "A grain-scale model for high-cycle fatigue degradation in polycrystalline materials". Int. J. Fatigue, vol. 116, pp.90-105, November 2018.

I.Benedetti, H.Nguyen, R.A Soler Crespo, W.Gao, L.Mao, A.Ghasemi, J.Wen, S.Nguyen, and H.D.Espinosa, "Formulation and validation of a reduced order model of 2D materials exhibiting a two-phase microstructure as applied to graphene oxide" J Mech Phys Solids, vol.112, pp.66-88, March 2018.

M.D. Banea, and L.F.da Silva, "Adhesively bonded joints in composite materials: an overview" Proc. Inst. Mech. Eng., Part L; J. Mater. Des. Appl, vol. 223, pp.1-18, January 2009.

M.D.Banea, L.F. da Silva, R.D. Campilho and C.Sato, "Smart adhesive joints: An overview of recent developments" J. Adhes., vol. 90, pp.16-40, january 2014.

Y. Du, and L.Shi, "Effect of vibration fatigue on modal properties of single lap adhesive joints" Int. J. Adhes, vol.53, pp.72-79, September 2014.

A. Sellitto, S.Saputo, A. Russo, V. Innaro, A. Riccio, F. Acerra, and S. Russo, "Numerical-experimental investigation into the tensile behavior of a hybrid metallic–CFRP stiffened aeronautical panel" J. Appl. Sci., vol.10(5), p.1880, March 2020.

L.Ke, C.Li, N. Luo, J. He, Y. Jiao, and Y. Liu, "Enhanced comprehensive performance of bonding interface between CFRP and steel by a novel film adhesive". Compos. Struct., Vol. 229, 111393, December 2019.

F.Moroni, A.Pirondi, and F. Kleiner, "Experimental analysis and comparison of the strength of simple and hybrid structural joints", Int. J. Adhes, vol. 30, pp.367-379, July 2010.

Y. Chen,X. Yang, M. Li, K. Wei, and S. Li, "Mechanical behavior and progressive failure analysis of riveted, bonded and hybrid joints with CFRP-aluminum dissimilar materials" Thin-Walled Struct., vol.139, pp.271-280, Jun 2019.

G.H. Lim, K.Bodjona, K.P.Raju, S.Fielding, V. Romanov, and L. Lessard, "Evolution of mechanical properties of flexible epoxy adhesives under cyclic loading and its effects on composite hybrid bolted/bonded joint design". Compos. Struct, vol. 189, pp.54-60, April 2018.

Y.Zheng, C.Zhang, Y .Tie, X. Wang, and M.Li, "Tensile properties analysis of CFRP-Titanium Plate multi-bolt hybrid joints.", CJA. vol. 35, pp.464–474. March 2022.

E. Selahi, "Failure study of hybrid bonded-bolted composite single and double lap joints" J. Stress Anal, vol. 3, pp.37-46, Februray 2019.

R.Aniello, A. Valerio, S. Andrea, P. Concetta, and F. Di Caprio, "A comparative numerical-experimental investigation on the tensile behaviour of bonded, rivetted and hybrid composite joints configurations" Compos. Struct. , vol. 318, p.117114, August 2023.

L. Li, W. Wang, E. Chatzi, and E. Ghafoori,"Experimental investigation on debonding behavior of Fe-SMA-to-steel joints" Constr Build Mater. vol. 364, p.129857, January 2023.

Yu Du and Lu Shi, "Effect of vibration fatigue on modal properties of single lap adhesive joint", Int. J. Adhes. vol. 53, pp. 72–79, September 2014.

T. L. Yogesh and N. Arunkumar, "Failure mode and analysis of the bonded/bolted joints between a hybrid fibre reinforced polymer and aluminium alloy", J. Adv. Mater. vol.3, pp. 49-60, 2015.

S.Fawzia, R.Al-Mahaidi, and X.L.Zhao, "Experimental and finite element analysis of a double strap joint between steel plates and normal modulus CFRP".Compos. Struct. Vol. 75, p. 156- 162. September 2006.

R.D.S.G. Campilho, M.F.S.F.De Moura, D.A.Ramantani, J.J.L. Morais, and J.J.M.S. Domingues, "Buckling strength of adhesively-bonded single and double-strap repairs on carbon-epoxy structures" Compos Sci Technol. vol. 70, pp.371-379, Februray 2010.

M. Rachid, B. Serier, B.B. Bouiadjra, and M. Belhouari, "Numerical analysis of the patch shape effects on the performances of bonded composite repair in aircraft structures" Compos. B. Eng. vol.43, pp.391-397, March 2012.

J.M. Arenas, C. Alía, J.J. Narbón, R.Ocaña, and C. González, "Considerations for the industrial application of structural adhesive joints in the aluminium–composite material bonding". Compos. B. Eng. vol.44, pp.417-423, January 2013.

S.E. Moussavi-Torshizi, S. Dariushi, M. Sadighi, and P. Safarpour, "A study on tensile properties of a novel fiber/metal laminates". Mater. Sci. Eng.A. vol. 527, pp.4920-4925, July 2010.

H.S. da Costa Mattos, A.H. Monteiro, and R. Palazzetti, "Failure analysis of adhesively bonded joints in composite materials" Mater. Des. vol. 33, pp.242-247, January 2012.

LI, X. et al."Tensile properties of a composite–metal single-lap hybrid bonded/bolted joint", Chinese J. Aeronaut., vol.34, pp.629–640, Februray 2021.

Huntsman Advanced Materials. Advanced Materials; Araldite®LY 5052/Aradur®5052* COLD CURING EPOXY SYSTEMS; Huntsman Advanced Materials: Woodloch, TX, USA, 2010.

Elastollan TPU Technical Data Sheet BASF,http://www.elastollan.basf.us/pdf/1185AF01.pdf.

ASM International. ASM Handbook Volume 2: Properties and Selection: Nonferrous Alloys and Special-Purpose Materials; ASM International: Novelty, OH, USA, 1990; ISBN 978-0-87170-378-1.

Carbon fiber Tairyfil Carbon Fiber data, http://www.fpc.com.tw/fpcwuploads

ASTM International ASTM D3528-96(2016); Standard Test Method for Strength Properties of Double Lap Shear Adhesive Joints by Tension Loading. ASTM: West Conshohocken, PA, USA, 2016.

R.J. Carbas, M.P. Palmares and L.F.da Silva,"Experimental and FE study of hybrid laminates aluminium carbon-fibre joints with different lay-up configurations", Manuf. Rev. vol. 2, pp.2, January 2020.

L.Sun, C.Li, Y.Tie,Y. Houand and Y.Duan, "Experimental and numerical investigations of adhesively bonded CFRP single-lap joints subjected to tensile loads" Int. J. Adhes. Adhes, Vol. 95, pp.102402, December 2019.

M. El Zaroug, F. Kadioglu, M. Demiral and D. Saad, "Experimental and numerical investigation into strength of bolted, bonded and hybrid single lap joints",Int. J. Adhes. Adhes, vol.87, pp.130-141, December 2018.

H. Luo, Y. Yan, T. Zhang and Z. Liang, "Progressive failure and experimental study of adhesively bonded composite single-lap joints subjected to axial tensile loads". J. Adhes. Sci. Technol., vol.30, pp.894-914, April 2016.

L.D Ramalho, R.D Campilho, J. P Belinha and L.F da Silva, "Static strength prediction of adhesive joints: A review", Int. J. Adhes. Adhes. Vol. 96, pp.102451, January 2020.

R.D. Adams, J.Comyn and W.C.Wake, "Structural adhesive joints in engineering". Springer Science & Business Media, Otober 1997.

W.R. Ashcroft, "Curing agents for epoxy resins:In Chemistry and technology of epoxy resins" ,Dordrecht: Springer Netherlands, pp. 37-71,1993.

A.Kausar, "Polyurethane/epoxy interpenetrating polymer network". Aspects of polyurethanes, vol.27, 2017.

G.S Chae, H.W.Park, J.H.Lee and S.Shin, "Comparative study on the impact wedge-peel performance of epoxy-based structural adhesives modified with different toughening agents". Polym. J.vol.12, p.1549 July 2020.

Investigation of Tensile behavior of double lap Adhesive joints between metal and composite

Hafiz Muhammad Umar Farooq [1], Muhammad Yasir [2] , Muhammad Azeem [3]
Department of Mechanical Engineering, University of Wah
Wah cantt, Pakistan
umar.farooq@wecuw.edu.pk; muhammad.yasir@wecuw.edu.pk; m.azeem@wecuw.edu.pk;
Waqas Javid [4], Shahid Iqbal [5]
Department of Mechanical Engineering, University of Wah, Quaid Avenue
Wah cantt, Pakistan
Waqas.Javid@wecuw.edu.pk; Shahid.Iqbal@wecuw.edu.pk;

Abstract: In this study, Metal (AA 6061-T6) and composite (Kevlar/epoxy laminates) double lap adhesive joints were constructed and their mechanical properties were assessed. Prior to the fabrication of joints using hand layup technique, surface treatments are applied to metal sheet, such as grinding with sandpaper, degreasing, and anodizing (with phosphoric acid). Using the same method, two alternative joint configurations were created. In the first case, the double epoxy lap joint is used, while in the second case, the double phenolic lap joint is used. Using tensile failure load, fracture toughness (GIIC) was calculated analytically. In tensile test both specimens failed nearly at same failure load and dominating failure pattern was cohesive. The results showed that in tensile test both specimens i.e. double lap epoxy and phenolic joints failed at same load. Cohesive failure pattern was dominated in all tensile test cases, while in some cases there was mixed Kevlar fiber and adhesive failure.

Keywords: *Adhesively bonded joints, double lap joints, tensile loading, fiber metal laminate.*

Introduction

Fiber metal laminates (FMLs) are advanced composite materials that combine the high strength and stiffness of metal alloys such as aluminum with the toughness and damage tolerance of fiber-reinforced epoxy such as Kevlar/epoxy polymers. Many different industries, such as aerospace, automotive, marine, and construction, use FMLs, where they offer improved performance, durability, and weight savings over traditional materials. Adhesives come in many forms, including liquid, pastes, tapes and films and can be made from a variety of materials, such as epoxy, acrylic, cyanoacrylate and polyurethane. Mechanical fastening involves drilling holes in a material, which is a technique that can cause cracks to form. Following the application of load, cracks may spread and fail. FMLs have higher strength-to-weight ratios than traditional fasteners, are corrosion-resistant, and perform better under impact and fatigue [1]. There are several varieties of adhesive joints, including tongue-and-groove lap joints, joggle lap joints, single and double lap joints, single and double strap joints, and plain butt joints[2].

In order to repair massive structures like airplanes, bridges, turbine blades, and windmills, double lap adhesive joins between metal and composite are frequently utilized [3]. To create double lap joints using distinct mechanical processes (peel ply, sandpaper, sandblast), scientists employed diverse procedures (manual layup, autoclaves) [4,5] and chemical (phosphoric chromic acid anodizing, phosphoric acid, sulfuric acid, and phosphoric acid) [6,8] surface finishes on aluminum alloy with various composite lap shapes [9,10] edge geometry [11,13] fiber type, stacking sequence [14] overlap length [12,15,16] adhesive thickness [17] and curing temperature [18]. Tests were performed under tensile [13,19] to measure tensile strength.

To enhance composites' mechanical attributes, thin metallic sheets are frequently sandwiched between fiber-based polymers. Three of the most noteworthy FMLs are generally carbon-reinforced aluminum laminate (CARALL), glass-reinforced aluminum laminate (GLARE), and aramid-reinforced aluminum laminate (ARALL) [20]. Several kinds of FMLs showed great strength when in contrast to solid metal sheets [21]. As these laminates are used more often in aerospace applications, where failure could have catastrophic effects, their mechanical strength is essential. Researchers have investigated several preventative measures to better comprehend how FMLs react to failures. The kind and quantity of metal layers, the order in which they are stacked, and the layer orientation have all been found to be important factors in the FMLs' mechanical toughness [22]. Furthermore, the amount of glue has been seen to vary.

Through experiments or computational methods, a thorough examination of double epoxy lap joints has been documented in the literature. There is no published mention of the work including the investigation of phenolic double lap joints. This research study consequently includes tensile testing of double lap epoxy and phenolic adhesive connections between metal and composite (aluminum alloy 6061-T6 metal with Kevlar/epoxy composite laminates). In this study, two novel techniques are investigated. One concerns the woven Kevlar fiber orientation in Kevlar/epoxy laminates, while the other concerns a comparison of double lap (epoxy and phenolic) geometrical configurations. Instead of manufacturing with autoclaves, these designs were made using the fairly affordable hand layup approach. Tensile testing was used to determine the failure load. Analytical calculations were made to determine the Mode II fracture energy values (GIIC) utilizing experimental data. Finally, an optical microscope was used to observe the fracture surface between laminates made of aluminum and Kevlar/epoxy.

Experimental Procedures

A. Materials

In this study, an aluminum alloy 6061-T6 plate with a 5 mm thickness was used. This alloy finds extensive usage in the automotive and aerospace industries, particularly in the production of aircraft wings and fuselages [24]. The alloy's fluidity is a key factor in influencing the fracture energy of FMLs. The alloy AA6061-T6 has high formability and moderate strength. The chemical composition of this alloy is given in Table 1.

Table 1. Standard Al 6061-T6 alloy plate chemical makeup (35).

Element	2] Si	3] Mg	4] Cu	5] Cr	[6] Fe	[7] Mn	[8] Zn	[9] Ti	[10] Al
] Weight % (max)	2] 0.8	13] 1.2	14] 0.4	15] 0.35	[16] 0.7	[17] 0.15	[18] 0.25	[19] 0.15	[20] Bal

A synthetic fiber called KEVLAR is renowned for its extraordinary strength and heat resistance. It is a trademark for a kind of aramid fiber that DuPont created in the 1960s. Here are some key features and applications of KEVLAR, it is incredibly strong. It is five times stronger than steel on an equal weight basis, making it a popular choice for applications where high tensile strength are required. It has a high modulus of elasticity, which refers to its ability to resist deformation when subjected to an applied force. In terms of stiffness, KEVLAR is considered to be a highly stiff material.

Araldite LY5052 epoxy resin and Aradur 5052 hardener are the two components of the adhesive system used to join two constituents together (Tei Composites, Chang Hua, Taiwan) [25] and phenolic refers to a type of synthetic polymer known as phenolic resin, is a versatile and widely used material that exhibits excellent heat resistance. For the hand layup method, epoxy resin, a low viscosity epoxy resin, is employed. This needs 48 hours to cure at room temperature. To maximize the degree of cross-linkage and improve composite characteristics, the resin has to postcure for four hours at 100 °C. The adherence to aluminum alloy is not particularly optimized for this epoxy. Surface preparation is required to achieve a strong connection between epoxy and aluminum sheets [26,28].

B. Surface Preparation

There were two procedures used to prepare the aluminum alloy's surface. In the first step, several sandpapers with grain sizes of 180, 320, 600, 1000, 1200, and 2000 were used to polish the alloy aluminum's surface. The ground surface was then cleaned for 15 minutes with a solution of 11% NaOH, followed by 15 minutes of deoxidation with a solution of 10% Na2Cr2O7 and 30% H2SO4 in water. The plates were then anodized in accordance with ASTM standard D3933-98 using a 12% H3PO4 solution at 12 V DC for each of the 25 minute processes. After that, the resin layup was completed [29].

C. Resin Layup Process

The traditional hand layup method was used to complete the resin layup procedure. It is clear that, in order to complete the hand layup process, the substrate (aluminum) must be assembled on a fixture, particularly for the double lap junction. On each side of the aluminum plates, nine layers of fiber were layered. To enhance the mechanical qualities of the junction, all of the constructed plates underwent postcuring for 4 hours at 100 °C. So, for the tensile testing, five sets of specimens were constructed. As seen in Table 2, these specimens received specific identification codes.

Table 2. Codes assigned to different specimens prepared.

[21] **Specimen No.**	[22] **Specimen Configuration**	23] **Code Assigned**
1	Double Epoxy Lap Joint Tensile Test	TT-E
2	Double phenolic lap joint Tensile Test	TT-P

D. Specimen Configuration

The specimens were created in accordance with Fig. 1 and 2 in accordance with ASTM standard D 3528-96 [47].

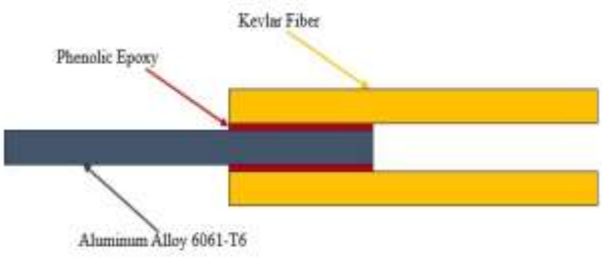

Fig. 1. Aluminum and KEVLAR fibers are sandwiched between two layers of phenolic (all measurements are in millimeters).

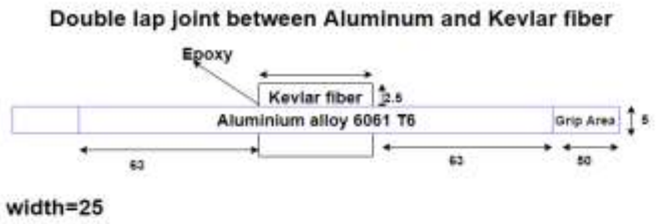

Fig. 2. Double lap epoxy between aluminum and KEVLAR fibers (all the dimensions are in

millimeters).

As shown in Fig. 3, standard tensile tests were completed, and load-displacement trajectories produced. Using these curves and an analytical equation, GIIC values were derived [30].

Fig. 3. Specimen under tensile test.

Energy release rate for double epoxy lap and phenolic lap joints between metal and composite is calculated under shear force for all sets of specimens using analytical expression in equation (1). The obtained values were used for simulation of cohesive zone model to have comparison with the experimental results. Both groups of tensile samples underwent the calculation of the Fracture energy GIIC. Equation (1) contains the formula for calculating fracture energy.

$$GIIC = \frac{Fmax^2(E_b t_b + 3E_s t_s)}{3E_b t_b w^2(E_b\ t_b + E_s t_s)} \qquad (1)$$

Where;

G_{IIC} = Fracture energy

Fmax = Maximum bearing force

Eb = Aluminum's base metal Young's modulus

Es = Young's Modulus of (Kevlar/epoxy)

tb = Thickness of base metal (aluminium)

ts = Thickness of (Kevlar/epoxy)

w = width of the specimen

Method and Results

A. *Tensile Test*

All specimens were evaluated using ASTM standard D 1002-01 till failure in stress to ascertain the impact of the epoxy and phenolic on the strength of the double lap joint [32]. The studies were carried out on a hydraulic MTS 810 machine with a crosshead speed of 1.27 mm/min and a lap-to-jaw distance of 63 mm. A data collecting system was used during the testing to gather displacement and loading records from the load cell mounted on the loading fixture. Tensile test was performed to find the failure load, failure pattern and fracture energy in case of lap joint with a configuration of epoxy and phenolic. Five specimens were tested for each case. Results in the form of failure load and extension is presented in table 3,4 and fig. 5,6 which shows that under tensile loading both specimens fail at same load with a difference of 1% which is negligible. Mean values of double lap epoxy and phenolic lap joints are presented in table 6. Fig. 4 depicts the fracture surfaces of the epoxy and phenolic double lap joints. Both sides of the aluminum sheets experience cohesive failure in the epoxy lap junction, but only cohesive failure was seen in the phenolic lap joint, despite greater failure stresses.

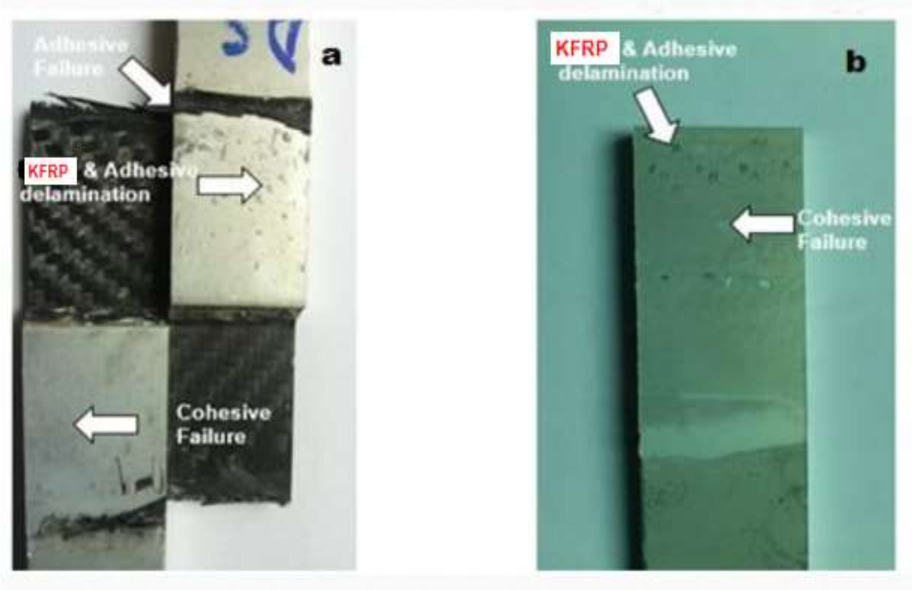

Fig.4. Failure patterns in tensile test. (a) Double Epoxy lap joint. (b) Double phenolic lap joint

Table 3 Tensile test of Double Epoxy lap joint

Double epoxy lap joint	**Failure Load (kN)**	**Failure Load Standard Deviation (kN)**	**Extension (mm)**	**Extension Standard Deviation (mm)**	**Fracture Energy (GIIC) (J/m^2)**
TT-E-01	6.82	[24] 0.03	0.60	0.006	340
TT-E-02	5.95	[25] 0.01	0.45	0.003	332
TT-E-03	6.49	0.02	0.49	0.004	334
TT-E-04	6.74	0.02	0.55	0.005	338
TT-E-05	6.01	0.01	0.46	0.003	331

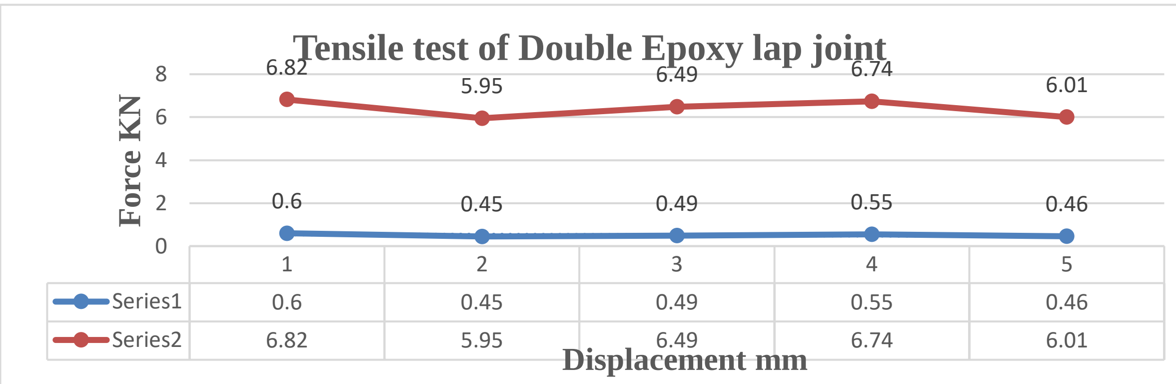

Fig. 5. Tensile test of Double Epoxy lap joint [36]

Table 4 Tensile test of Double phenolic lap joint [36]

Double epoxy lap joint	Failure Load (kN)	Failure Load Standard Deviation (kN)	Extension (mm)	Extension Standard Deviation (mm)	Fracture Energy (GIIC) (J/m^2)
TT-E-01	6.4	[26] 0.03	0.54	0.006	340
TT-E-02	5.65	[27] 0.01	0.46	0.003	332
TT-E-03	6.38	0.02	0.47	0.004	334
TT-E-04	6.27	0.02	0.51	0.005	338
TT-E-05	6.39	0.01	0.48	0.003	331

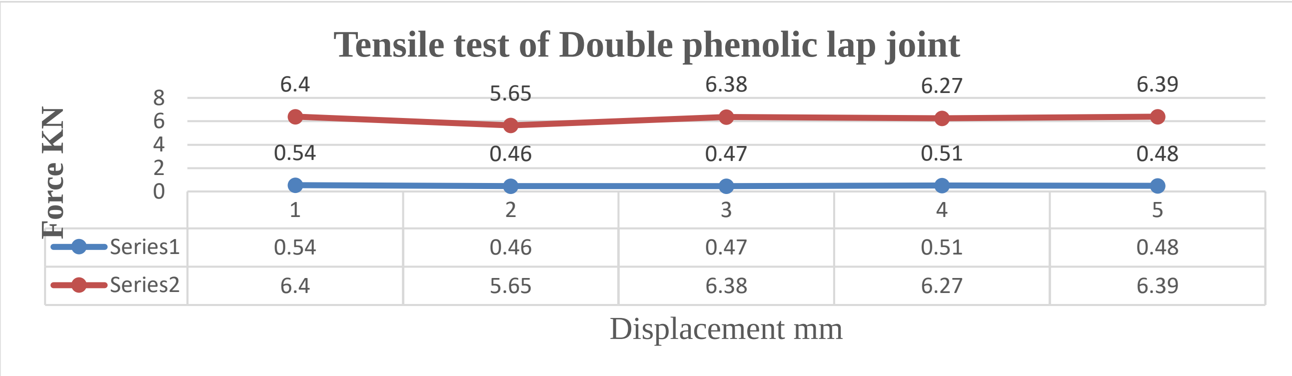

Fig. 6. Tensile test of Double phenolic lap joint

Table 6 Mean values of Epoxy and Phenolic lap joint

Specimen type	Failure Load kN	Extension mm
TT-E (Epoxy lap)	6.4	0.51
TT-P (Phenolic lap)	6.2	0.49

Conclusion

The strength of a double epoxy lap joint and the orientation of plain-woven Kevlar fiber on an aluminum 6061-T6 plate are the main subjects of this study, along with a comparison to the strength of a double phenolic lap joint. The impact of the preferred surface treatment and manufacturing method on tensile strength was assessed. Aluminum and Kevlar fiber lap joints made of double lap epoxy and phenolic have been used to analyze two different cases. The following are the research's primary findings: Both specimens—double lap epoxy and phenolic joints—failed the tensile test at the same load. In all tensile test situations, the adhesive failure pattern predominated, albeit there were a few instances of combined Kevlar fiber and adhesive failure. The traction-separation law failure pattern was bilinear or triangular in shape. As a result of the shearing mechanism, all cohesive elements were eliminated simultaneously. The cohesive strength of the adhesive is primarily responsible for the joint's strength. The strength of the junction was reduced by homogeneities such air bubbles, dust, or oil particles in the glue [36].

Both the double epoxy lap joint and the double phenolic lap joint exhibited adhesive and cohesive failures during tensile testing. However, when compared to double epoxy lap joints, double phenolic lap joints had 1.4% more fracture energy, 4.1% more capacity to stretch, and 0.6% more strength [36]. The outcomes of the experiment were supported by the literature [36]. The experimental and literature G_{IIC} As a function of the load-displacement curve, data were compared and found to be within 0.3% of one another. The traction-separation law's traction failure pattern was bilinear or triangularform.

References

1. Straznicky, P.; Laliberte, J.; Poon, C.; Fahr, A. Applications of Fiber-metal Laminates. *Polym. Compos.* **2004**, *21*, 558–567. [CrossRef]
2. Chapter 7-Joint Design. In *Adhesives Technology Handbook*, 2nd ed.; Ebnesajjad, S. (Ed.) William Andrew Publishing: Norwich, NY, USA, 2009; pp. 159–181, ISBN 978-0-8155-1533-3.
3. Pethrick, R.A. 5.15-Bond Inspection in Composite Structures. In *Comprehensive Composite Materials*; Kelly, A., Zweben, C., Eds.;Pergamon: Oxford, UK, 2000; pp. 359–392, ISBN 978-0-08-042993-9.
4. Kanerva, M.; Saarela, O. The Peel Ply Surface Treatment for Adhesive Bonding of Composites: A Review. *Int. J. Adhes. Adhes.* **2013**, *43*, 60–69. [CrossRef]
5. Arenas, J.M.; Alía, C.; Narbón, J.J.; Ocaña, R.; González, C. Considerations for the Industrial Application of Structural Adhesive Joints in the Aluminium–Composite Material Bonding. *Compos. Part B Eng.* **2013**, *44*, 417–423. [CrossRef]
6. Arenas, M.A.; Conde, A.; de Damborenea, J.J. Effect of Acid Traces on Hydrothermal Sealing of Anodising Layers on 2024 Aluminium Alloy. *Electrochim. Acta* **2010**, *55*, 8704–8708. [CrossRef]
7. Viejo, F.; Coy, A.E.; García-García, F.J.; Merino, M.C.; Liu, Z.; Skeldon, P.; Thompson, G.E. Enhanced Performance of the AA2050-T8 Aluminium Alloy Following Excimer Laser Surface Melting and Anodising Processes. *Thin Solid Film.* **2010**, *518*, 2722–2731.[CrossRef]
8. Moutarlier, V.; Gigandet, M.; Pagetti, J.; Normand, B. Influence of Oxalic Acid Addition to Chromic Acid on the Anodising of Al 2024 Alloy. *Surf. Coat. Technol.-SURF COAT TECH* **2004**, *182*, 117–123. [CrossRef]
9. Chuang, W.-Y.; Tsai, J.-L. Investigating the Performances of Stepwise Patched Double Lap Joint. *Int. J. Adhes. Adhes.* **2013**, *42*, 44–50. [CrossRef]
10. Benyahia, F.; Albedah, A.; Bachir Bouiadjra, B. Analysis of the Adhesive Damage for Different Patch Shapes in Bonded CompositeRepair of Aircraft Structures. *Mater. Des. (1980–2015)* **2014**, *54*, 18–24. [CrossRef]
11. Meneghetti, G.; Quaresimin, M.; Ricotta, M. Damage Mechanisms in Composite Bonded Joints under Fatigue Loading. *Compos.Part B Eng.* **2012**, *43*, 210–220. [CrossRef]
12. Quaresimin, M.; Ricotta, M. Fatigue Behaviour and Damage Evolution of Single Lap Bonded Joints in Composite Material. *Compos. Sci. Technol.* **2006**, *66*, 176–187. [CrossRef]
13. Sandu, M.; Sandu, A.; Constantinescu, D.M.; Apostol, D.A. Single-Strap Adhesively Bonded Joints with Square or TaperedAdherends in Tensile Test Conditions. *Int. J. Adhes. Adhes.* **2013**, *44*, 105–114. [CrossRef]
14. Akpinar, S. Effects of Laminate Carbon/Epoxy Composite Patches on the Strength of Double-Strap Adhesive Joints: Experimentaland Numerical Analysis. *Mater. Des.* **2013**, *51*, 501–512. [CrossRef]
15. Lee, H.K.; Pyo, S.H.; Kim, B.R. On Joint Strengths, Peel Stresses and Failure Modes in Adhesively Bonded Double-Strap andSupported Single-Lap GFRP Joints. *Compos. Struct.* **2009**, *87*, 44–54. [CrossRef]
16. Fawzia, S.; Al-Mahaidi, R.; Zhao, X.-L. Experimental and Finite Element Analysis of a Double Strap Joint between Steel Platesand Normal Modulus CFRP. *Compos. Struct.* **2006**, *75*, 156–162. [CrossRef]
17. Park, J.-H.; Choi, J.-H.; Kweon, J.-H. Evaluating the Strengths of Thick Aluminum-to-Aluminum Joints with Different AdhesiveLengths and Thicknesses. *Compos. Struct. -COMPOS STRUCT* **2010**, *92*, 2226–2235. [CrossRef]
18. Nguyen, T.-C.; Bai, Y.; Zhao, X.; Al-Mahaidi, R. Mechanical Characterization of Steel/CFRP Double Strap Joints at ElevatedTemperatures. *Compos. Struct.* **2011**, *93*, 1604–1612. [CrossRef]
19. Nguyen, T.-C.; Bai, Y.; Zhao, X.-L.; Al-Mahaidi, R. Durability of Steel/CFRP Double Strap Joints Exposed to Sea Water, CyclicTemperature and Humidity. *Compos. Struct.* **2012**, *94*, 1834–1845. [CrossRef]
20. Trzepieciński, T.; Najm, S.M.; Sbayti, M.; Belhadjsalah, H.; Szpunar, M.; Lemu, H.G. New Advances and Future Possibilities in Forming Technology of Hybrid Metal–Polymer Composites Used in Aerospace Applications. *J. Compos. Sci.* **2021**, *5*, 217. [CrossRef]
21. Vermeeren, C.A.J.R. An Historic Overview of the Development of Fibre Metal Laminates. *Appl. Compos. Mater.* **2003**, *10*, 189–205. [CrossRef]
22. Bieniaś, J.; Jakubczak, P.; Surowska, B. 11-Properties and Characterization of Fiber Metal Laminates. In *Hybrid Polymer Composite Materials*; Thakur, V.K., Thakur, M.K., Pappu, A., Eds.; Woodhead Publishing: Sawston, UK, 2017; pp. 253–277, ISBN 978-0-08-100787-7.
23. Li, H.; Hu, Y.; Fu, X.; Zheng, X.; Liu, H.; Tao, J. Effect of Adhesive Quantity on Failure Behavior and Mechanical Properties of Fiber Metal Laminates Based on the Aluminum–Lithium Alloy. *Compos. Struct.* **2016**, *152*, 687–692. [CrossRef]

24. Kim, H.-K.; Park, E.-T.; Song, W.-J.; Kang, B.-S.; Kim, J. Experimental and Numerical Investigation of the High-Velocity Impact Resistance of Fiber Metal Laminates and Al 6061-T6 by Using Electromagnetic Launcher. *J. Mech. Sci. Technol.* **2019**, *33*, 1219–1229.[CrossRef]
25. Huntsman Advanced Materials. *Advanced Materials*; Araldite®LY 5052/Aradur®5052* COLD CURING EPOXY SYSTEMS;
Huntsman Advanced Materials: Woodloch, TX, USA, 2010.
26. Wegman, R.F.; van Twisk, J. 2-Aluminum and Aluminum Alloys. In *Surface Preparation Techniques for Adhesive Bonding*, 2nd ed.;Wegman, R.F., van Twisk, J., Eds.; William Andrew Publishing: Norwich, NY, USA, 2013; pp. 9–37, ISBN 978-1-4557-3126-8.
27. Critchlow, G.W.; Brewis, D.M. Review of Surface Pretreatments for Aluminium Alloys. *Int. J. Adhes. Adhes.* **1996**, *16*, 255–275.[CrossRef]
28. Davis, M.; Bond, D. Principles and Practices of Adhesive Bonded Structural Joints and Repairs. *Int. J. Adhes. Adhes.* **1999**, *19*,91–105. [CrossRef]
29. Cheuk, P.T.; Tong, L.; Wang, C.-H.; Baker, A.; Chalkley, P. Fatigue Crack Growth in Adhesively Bonded Composite-MetalDouble-Lap Joints. *Compos. Struct.* **2002**, *57*, 109–115. [CrossRef]
30. *ASTM International ASTM D3528-96(2016)*; Standard Test Method for Strength Properties of Double Lap Shear Adhesive Joints byTension Loading. ASTM: West Conshohocken, PA, USA, 2016.
31. Rotwitt, P.B. Fatigue Life Extension Using Composite Patch Repairs. Master's Thesis, University of Oslo, Oslo, Norway, 2013.
32. *ASTM International ASTM D1002-10(2019)*; Standard Test Method for Apparent Shear Strength of Single-Lap-Joint AdhesivelyBonded Metal Specimens by Tension Loading (Metal-to-Metal). ASTM: Novelty, OH, USA, 2019.
33. *ASTM International ASTM D3166-99(2020)*; Standard Test Method for Fatigue Properties of Adhesives in Shear by Tension Loading(Metal/Metal). ASTM: Novelty, OH, USA, 2020.
34. Systèmes, D. Abaqus Standard and Abaqus Documentation for Version 6.14. *Dassault Syst. Simulia Corp.* **2014**, *651*, 2–6.
35. ASM International. *ASM Handbook Volume 2: Properties and Selection: Nonferrous Alloys and Special-Purpose Materials*; ASM International: Novelty, OH, USA, 1990; ISBN 978-0-87170-378-1.
36. Azeem, M., Irfan, M., Masud, M., Rehman, G. U., Ali, H., Ali, M. U., ... & Kratochvíl, J. (2022). Experimental and Numerical Investigation of Effect of Static and Fatigue Loading on Behavior of Different Double Strap Adhesive Joint Configurations in Fiber Metal Laminates. *Materials*, *15*(5), 1840.

Towards the Greener Environment: Development and Fabrication of a PET Pelletizing Unit for Commercial Purposes

Muhammad Usman[1], Muhammad Ali[1], Hammad Khalid[1, *], Khubaib Sayyaf Khan[1], Ahtasham ul Haq[1], Irfan Ahmed[1], Muhammad Iqbal[1]
Khwaja Fareed University of Engineering and Information Technology (KFUEIT) 64200, Rahim Yar Khan[1]
meen201101002@kfueit.edu.pk, meen201101064@kfueit.edu.pk, hkhalid@kfueit.edu.pk, meen201101072@kfueit.edu.pk ,meen201101058@kfueit.edu.pk, meen201101090@kfueit.edu.pk ,meen2011010108@kfueit.edu.pk

1. INTRODUCTION

In response to the pressing global need for sustainable environmental practices, this study explores the development and fabrication of a PET (Polyethylene Terephthalate) pelletizing unit designed for commercial purposes. PET is one of the most commonly used plastics, contributing significantly to the growing plastic waste crisis and environmental pollution. Humans currently produce more than 430 million metric tons of plastic waste per year after few years it will be around 1 billion metric tons. (PADILLA-VASQUEZ 2023). This research aims to address this issue by proposing an innovative solution that enables the efficient recycling of PET materials, thereby reducing environmental harm and promoting a circular economy.

2. MATERIALS AND METHODS

The project methodology involves several key stages. The initial phase encompasses the design and construction of the PET pelletizing unit, which includes components such as a shredder, cleaning unit, and extrusion system. Subsequently, the study outlines the design and engineering considerations for the PET pelletizing unit, focusing on efficiency, scalability, and eco-friendliness. A key emphasis is placed on ensuring that the unit can be adopted by commercial entities, fostering widespread adoption of sustainable practices. The main focus is to design the extruder and pitch angle of the screw shaft so that it gives the maximum flow without any wear and tear. Here the optimal pitch angle is 17^0. The fabrication phase involves the construction, analysis and testing of the PET pelletizing unit, with a focus on its operational efficiency and environmental impact. The compression ratio of the extruder is 1:1 which is obtain by the ratio of feeding and metering section with the drag flow of $7.48*10^{-6}$ m^3/s. The length and diameter of the barrel is 97.1cm and 6cm respectively. (P.Groover, Fundametal of Modern Manufacturing 2010)

3. CALCULATIONS

4.1 CALCULATING THE VOLUME OCCUPIED BY THE SCREW SHAFT (V_{SS})

Radius of screw shaft (r_{ss}) = 19mm ~ 1.9cm
Length of the screw shaft (L_{ss}) = 971mm = 97.1cm

$$V_{ss} = \pi \times r_{ss}^2 \times L_{ss} \qquad \text{(R.Millet 1997)}$$

$$V_{ss} = 3.142 \times (1.9)^2 \times 97.1$$

$$V_{ss} = 3.142 \times 3.61 \times 97.1$$

$$V_{ss} = 1100 cm^3$$

4.2 CALCULATING FOR VOLUME OCCUPIED BY THE SCREW FLIGHT (V_{SF})

Number of screw ribs (n_{sr}) = 14 = 7 rev
Length of 1 screw rib (L_{sr}) =20mm = 2cm
Length of 7 screw rib (L_{sr}) = 2 x 7 = 14cm
Radius of the screw rib (r_{sr}) = 30 - 19 = 11mm = 1.1cm

$$V_{sf} = \pi \times r_{sr}^2 \times L_{sr} \qquad \text{(R 1998)}$$

$$V_{sf} = 3.142 \times (1.1)^2 \times 14$$
$$V_{sf} = 3.142 \times 1.21 \times 14$$
$$V_{sf} = 53.22cm^3$$

4.3 **CALCULATING FOR VOLUME OCCUPIED BY THE SCREW (VS)**

$$V_s = V_{ss} + V_{sf}$$ (Tim A.Oswald 2009)

$$V_s = 1100cm^3 + 53.22cm^3$$
$$V_s = 1153.22cm^3$$

4.4 **CALCULATION FOR SCREW GEOMETRY**

$$\tan\varphi = \frac{pitch}{\pi D_s}$$

(P.Groover, Fundametal of Modern Manufacturing 2010)

Where,

Helix angle (φ) = ?

Screw diameter$(D_s) = 60mm$

Screw pitch (P) = 60 mm

$$\tan\varphi = \frac{60}{3.148 \times 60}$$
$$\tan\varphi = \frac{1}{3.148}$$
$$\varphi = tan^{-1}(0.3184)$$
$$\varphi = 17.7^{\circ}$$

4.5 **CALCULATION FOR COMPRESSION RATIO**

$$\text{CR} = \frac{\text{channel depth in feed section}}{\text{channel depth in metering section}}$$

(Ugboya, Odiamenhi and Aigbogie 2019)

$$\text{CR} = \frac{11}{11} = 1$$
$$\text{CR} = 1:1$$

4.6 **Drag Flow (Q_d)**

$$Q_d = \frac{1}{2} \times \pi^2 \times D_s^2 \times N_1 \times H_{cd} \times \sin\varphi \times \cos\varphi$$

(P.Groover, Fundamentals of the Modern Manufacturing 2010)

Where,
Screw diameter (D_s) = 60mm = 0.06m
Screw Speed (N_2) = 58.2r.p.m=0.97 r.p.s
Channel Depth (H_{cd}) = 1.5mm = 0.0015m
Helix angle (φ) = 17.7^0
Therefore,

$$Q_d = \frac{1}{2} \times (3.142)^2 \times (0.06)^2 \times 0.97 \times 0.0015 \times \sin(17.7) \times \cos(17.7)$$
$$Q_d = 7.48 * 10^{-6}\ m^3/s$$

4. CONCLUSION

In conclusion, the Development of a PET Pelletizing Unit for Sustainable Plastic Recycling has successfully realized its objectives. The unit is ready for implementation in industrial settings, where it has the potential to revolutionize PET recycling practices, reduce environmental harm, and foster a greener, more sustainable future. This project emphasis the importance of innovative engineering solutions in addressing critical global challenges.

5. RESULTS AND DISCUSSION

This research have two main outcomes i.e. pellets and finished products. The pellets are used by the industries as a raw material to make different plastic products and the finished products are obtained by using different dies. Furthermore, the study emphasis the importance of collaborative efforts among governments, industries, and consumers to promote the adoption of such eco-friendly technologies and practices on a global scale. This represents a significant step towards achieving a greener environment by addressing the challenges posed by PET waste through the development and fabrication of an efficient and scalable PET pelletizing unit for commercial use.

6. ACKNOWLEDGMENT

I take this momentous opportunity to express my heartfelt gratitude and regards to Institute of Mechanical & Manufacturing Engineering KFUEIT for providing us essential support, tools and mediums for my design idea and conducting its practical test.

7. REFERENCES

1. Sakai T, Seikei-Kakou (2005), International polymer processing, Vol. 17, 20, Pages17-216; 109.
2. R. M. Ogorkiewicz (1977), The Engineering Properties of Plastics, Oxford University Press.
3. Kokini J. L. (1993), the effect of processing history on chemical changes in single-screw and twin screw extruders. Trends in Food Science and Technology, 4 (10), 324-329
4. Cassagnau.P, M.and Taha, J. (1996), Application. Polymer.Science, 60 (10).
5. Karwe M. V; Godavarti S. (1997), Accurate measurement of extrudate temperature and heat loss on a twin-screw extruder. Journal of Food Science, 62(2), 367-372.
6. R. Millet (1997), Design and Technology of plastic, A Wheaton and Co. Ltd., Exeter.
7. Crawford R. (1998), Plastic Engineering, 3rd ed. Oxford: Butterworth - Heine-mann
8. Tim A. Oswald, Juan Pablo Hernandez-Ortiz (2009), Polymer processing [www.books.google.uk (online) Available, http://books.google.co.uk/books].
9. Rosato, Mariene G. (2000), Concise encyclopedia of plastics, Springer, page. 245, ISBN 978-0-7923-8496-0.
10. R. S. Khurmi and J. K. Gupta (2005). A Textbook of Machine Design, Eurasia Publishing House (PVT.) ltd.
11. S. Kalpakjian and S.R. Schmid (2008), Manufacturing Processes for Engineering Materials,
12. 5th ed., Pearson Education
13. Understanding Injection Molding Technology, Herbert Rees, Orangeville Ontario 1994, Hanser Publishers, Munich, ISBN 1-56990-130-9.
14. Shigley, J.E. (2006) Mechanical Engineering Design; McGraw-Hill Companies Inc., Eighth Edition
15. Design and development of injection moulding machine for manufacturing maboratory; IOP Conf. Series: Journal of Physics: Conf. Series 908: 1-6.
16. R A García-León et al 2019 J. Phys.: Conf. Ser. 1257 012006
17. John, M. (2009) Plastic Moulding Techniques, All about plastic moulding.
18. Melick, H.G.H. (1995) Design of an injection molding machine

Proc. 2023 International Conference on Advances in Multidisciplinary Engineering, Sciences and Technology (ICAMEST)
29-30 September 2023, Dubai, UAE

Diethyl Ether as an Additive for Improving Cold Flow Properties of Diesel Fuel/Biodiesel Blends

Mert Gülüm
Mechanical Engineering Department
Karadeniz Technical University
Trabzon, TURKEY
gulum@ktu.edu.tr

Sibel Osman
Department of Chemistry and Chemical Engineering
Ovidius University of Constanta
Constanta, ROMANIA
sibel_o@yahoo.ro

***Abstract*—Biodiesel has excellent properties, yet its main drawbacks encompass higher viscosity, lower heating value, and poor cold flow properties, compared to diesel fuel. In this study, diethyl ether is used as an additive in diesel fuel/biodiesel binary blends to enhance their cold flow properties. For this, diesel fuel/biodiesel/diethyl ether ternary blends are prepared. The ternary blends include 5%, 10%, 15%, 20%, and 25% diethyl ether (v/v). The ternary blends are labeled as DEE5, DEE10, DEE15, DEE20, and DEE25. Some fuel properties (cold filter plugging point, cloud point, density, and kinematic viscosity) of the ternary blends are measured according to international standards. According to the results, cold filter plugging point values of ternary blends gradually decrease from -6°C to -10°C with increasing diethyl ether content while that of diesel fuel is -5°C. In other words, diethyl ether significantly improves the cold filter plugging point, making it a promising diesel fuel additive for cold weather conditions. Cloud point values of ternary blends gradually diminish from -4°C to -7°C with rising diethyl ether content while that of diesel fuel is -3°C. The use of DEE10, DEE15, DEE20, and DEE25 leads to a 0.40%, 1.35%, 2.22%, and 3.10% diminish in density, compared to that of DF. The density of DEE10, DEE15, and DEE20 comply with the values set by the EN 590 norm (820 and 845 kg/m^3). Kinematic viscosity values of ternary blends decrease with higher diethyl ether concentration, enhancing fuel spray and atomization. In other words, the kinematic viscosities of DEE5, DEE10, DEE15, DEE20, and DEE25 are 13.88%, 28.29%, 43.32%, 54.27%, and 57.55% lower than that of DF. This study suggests that DEE can address cold flow problems for diesel fuel/biodiesel binary blends while meeting quality standards.**

Keywords*—*alternative fuels, biodiesel, diethyl ether, cold flow properties

Introduction

The decline in fossil fuel reserves, escalating petroleum costs, and increasing threat to the environment from exhaust emissions have prompted the investigation of cleaner, renewable, and oxygenated alternative fuels that can be used in diesel engines. Examples of such fuels are given biodiesel, alcohols, and ethers [1].

Chemically, biodiesel is defined as a mixture of mono-alkyl esters of fatty acids. Biodiesel possesses a non-toxic quality, is biodegradable, can be produced from renewable sources via the transesterification reaction, and does not contain sulphur and aromatic compounds. Due to the oxygen content in its molecular structure, using biodiesel in diesel engines can reduce some exhaust emissions. Biodiesel has a higher flash point, which makes it a safer fuel concerning storage and transportation than diesel fuel. It can be mixed with diesel fuel in any proportion. Moreover, it exhibits enhanced lubricity, which leads to the extended lifespan of engine components. Biodiesel has also some disadvantages, including higher viscosity, poor oxidation stability, lower heating value, lower volatility, and poor cold flow properties, compared to diesel fuel. Poor cold flow properties are barriers to the use of biodiesel in cold weather [2-6].

Diethyl ether ($C_4H_{10}O$, DEE) has several advantageous characteristics for diesel engines, including high cetane number (>125), high oxygen content (21.6% by mass), low auto-ignition temperature (150-160^{o}C), wide flammability limits, and great miscibility with diesel fuel. Moreover, it was previously used as a cold-start aid for engines due to its low auto-ignition temperature and high volatility. The use of DEE assists in enhancing engine performance and curtailing emissions. DEE can be derived from ethanol through a dehydration process using acid catalysts, which makes DEE a biofuel. DEE has a somewhat higher gross heating value (36.8 MJ/kg) compared to ethanol (~30 MJ/kg) and butanol (~36 MJ/kg).

However, the remarkably low viscosity of DEE (0.23 mm^2/s) can escalate the wear rate within the diesel injection system. Additionally, some concerns exist regarding the effect of DEE on air pollution while in storage, owing to its high volatility and its propensity to undergo oxidation forming peroxides over time [1, 7-10].

In the existing literature, lots of experimental and numerical studies focus on the effects of adding DEE to diesel fuel/biodiesel blends on the performance, combustion, and emission characteristics of diesel engines [11-14]. However, researches addressing the enhancement of the cold flow properties of diesel fuel/biodiesel blends by using DEE remain limited. Therefore, in this study, diesel fuel/biodiesel/DEE ternary blends are prepared, and their fuel properties (density, kinematic viscosity, cloud point, and cold filter plugging point) are measured according to international standards. Finally, DEE blends that comply with EN 590 standard are determined.

MATERIALS and METHODS

Preparation of Ternary Blends

Diesel fuel (DF) and biodiesel (BD) are supplied by a local company in Constanta (Romania). DEE (99%) is purchased from Sigma–Aldrich and used without further purification. Some properties of DF and DEE are shown in Table I [15, 16].

TABLE XI. SOME PROPERTIES OF DF AND DEE

Properties	***DF***	***DEE***
Oxygen content (wt.%)	0	21.60
Cetane number	51.6	>125
Flash point (°C)	61	-45
Boiling point (°C)	160.6-366.6	34.6
Density (kg/m^3)	842.2 at 15ºC	713 at NTP
Kinematic viscosity (cSt)	3.0727 at 40°C	0.23 at NTP

A total of five ternary blends are used for this investigation. All blends are prepared based on different volume ratios of BD and DEE. The composition of the ternary blends used in this study is shown in Table II. In other words, the volume percentages of DEE in the ternary blends are 5%, 10%, 15%, 20%, and 25% while the volume percentage of DF is kept constant at 70%. In order to obtain ternary blends, DEE is blended with DF and BD using a magnetic stirrer for a time for homogeneity. No phase separation is observed in the ternary blends for a long time at room temperature.

USED TERNARY BLENDS AND THEIR CORRESPONDING VOLUME PERCENTAGES

No.	***Ternary blends***	***DF (%)***	***BD (%)***	***DEE (%)***
1	***DF***	***100***	***-***	***-***
2	***DEE5***	***70***	***25***	***5***
3	***DEE10***	***70***	***20***	***10***
4	***DEE15***	***70***	***15***	***15***
5	***DEE20***	***70***	***10***	***20***
6	***DEE25***	***70***	***5***	***25***

Test Methods and Equipment

Gas chromatography equipment (Clarus 500 GC) with a flame ionization detector (FID) is used to monitor the fatty acid composition of BD used in this study. The fatty acid methyl ester composition of BD is given in Table III. The properties of ternary blends (cold filter plugging point, cloud point, density, and kinematic viscosity) are measured using the equipment listed in Table IV. The measurements are run in triplicate for each blend. All measurements are performed at Ovidius University (Department of Chemistry and

Chemical Engineering).

FATTY ACID COMPOSITION OF BD

Fatty acid	*Composition (% w/w)*
Palmitic (C16:0)	3.12
Stearic (C18:0)	1.54
Arachidic (C20:0)	0.41
Oleic (C18:1)	39.41
Linoleic (C18:2)	39.08
11-Octadecenoic (C19:2)	15.82
Gadoleic (C20:1)	0.52

THE METHOD AND EQUIPMENT USED FOR THE DETERMINATION OF THE PROPERTY

Properties	*Standard Method*	*Equipment*	*Repeatability*	*Reproducibility*
Cold filter plugging point	EN 116: 2015	CFPP OptiFPP	1.76°C	0.102(25-x)°C
Cloud point	EN ISO 3015:2019	Herzog 852 Automatic Analyzer	2°C	4°C
Density	EN ISO 12185:1996	Anton Paar - SVM 3000	0.0001 g/cm^3	0.0005 g/cm^3
Viscosity	EN ISO 3104:1996		0.1%	0.35%

RESULTS and DISCUSSION

The cold filter plugging point (CFPP) and the cloud point (CP) are used to assess a fuel's performance at low temperatures. Diesel fuel/biodiesel blends may have starting problems at low temperatures, through the formation of small crystals which can clog filters. Because biodiesels generally have relatively poor cold flow properties, it is disadvantageous to use them in cold weather.

Cold Filter Plugging Point (CFPP)

CFPP is the lowest temperature at which 20 mL of fuel passes through a filter within 60 s by applying a vacuum of 2 kPa [17]. Figure 1 shows the CFPP values of ternary blends. The addition of DEE results in a significant improvement in low temperature performance. The CFPP of DF is -5°C. CFPP of DEE5, DEE10, DEE15, DEE20, and DEE25 is measured as -6°C, -7°C, -8°C, -9°C, and -10°C, respectively. In other words, CFPP gradually decreases with increasing DEE content, compared to DF. The extremely low freezing point of DEE (-116°C) [18, 19] allows lowering of the freezing point of blends, which improves the CFPP of DEE blends. It can be concluded that the addition of DEE improves the crystallization properties of ternary blends. The results are quite promising for the prospect of using DEE as an additive in diesel fuel/biodiesel blends. These blends comply with the EN 590 norm in terms of CFPP.

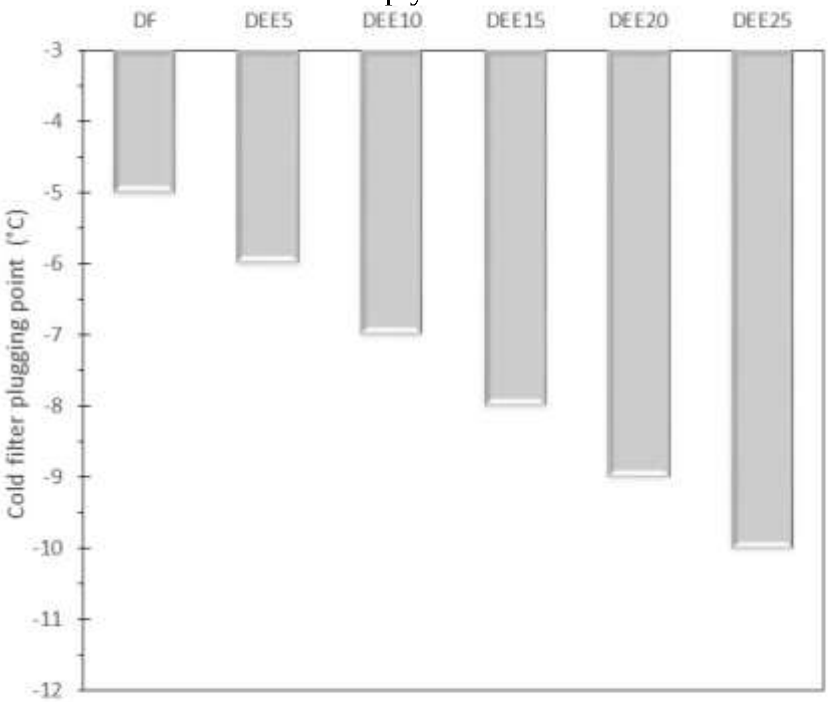

CFPP of ternary blends.

Cloud Point (CP)

CP can be defined as the temperature at which crystals are first detected in the fuel [20]. The temperature at which a cloudy appearance is visually detected in the sample while cooling is considered the cloud point temperature of the sample. Figure 2 presents the CP values of ternary blends. In all DEE blends, CP decreases with the DEE addition. In the case of DEE5, DEE10, DEE15, DEE20 and DEE25, CP values are measured as -3°C, -4°C, -5°C, -6°C, and -7°C, respectively. These results show that the addition of DEE has led to a decrease in CP. In other words, DEE improves CP. The addition of DEE cannot lead to operational issues in cold climates, such as filter plugging due to wax build-up or reduced fuel flow [21].

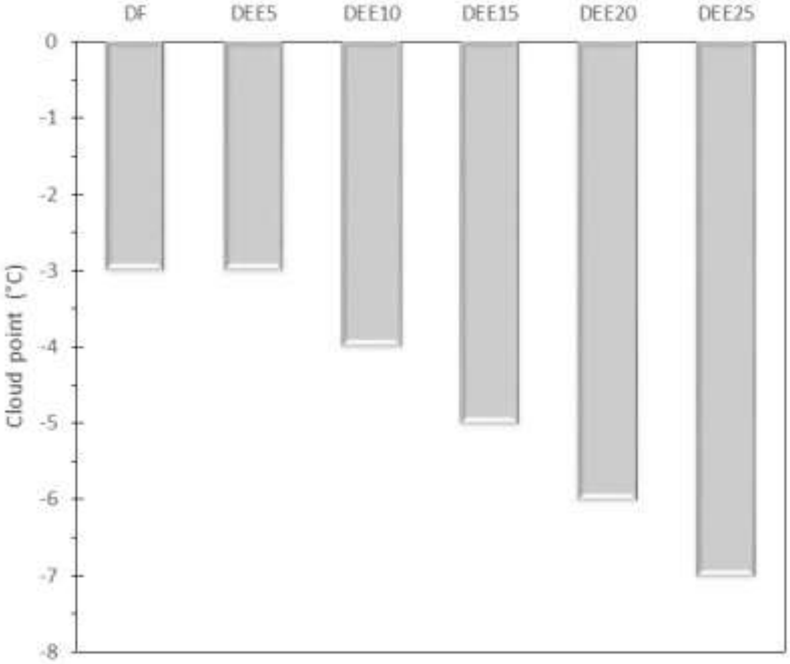

CP of ternary blends

Density

The density values of ternary blends at 15°C are given in Figure 3. As expected, the densities of DEE blends decrease with the increase of DEE concentration, because the density of DEE (713 kg/m^3) is lower than that of DF (842.2 kg/m^3 at 15ºC). Density values are measured as 846.7 kg/m^3, 838.8 kg/m^3, 830.8 kg/m^3, 823.5 kg/m^3, and 816.1 kg/m^3 for DEE5, DEE10, DEE15, DEE20, and DEE25, respectively. DEE5 is slightly denser (+0.53%) than DF due to the higher density of BD (883.7 kg/m^3 at 15ºC). The obtained results show that DEE10, DEE15, DEE20, and DEE25 lead to a 0.40%, 1.35%, 2.22%, and 3.10% decrease, compared to the initial density value of DF. The density of DEE10, DEE15, and DEE20 comply with the values set by the EN 590 norm (820 and 845 kg/m^3).

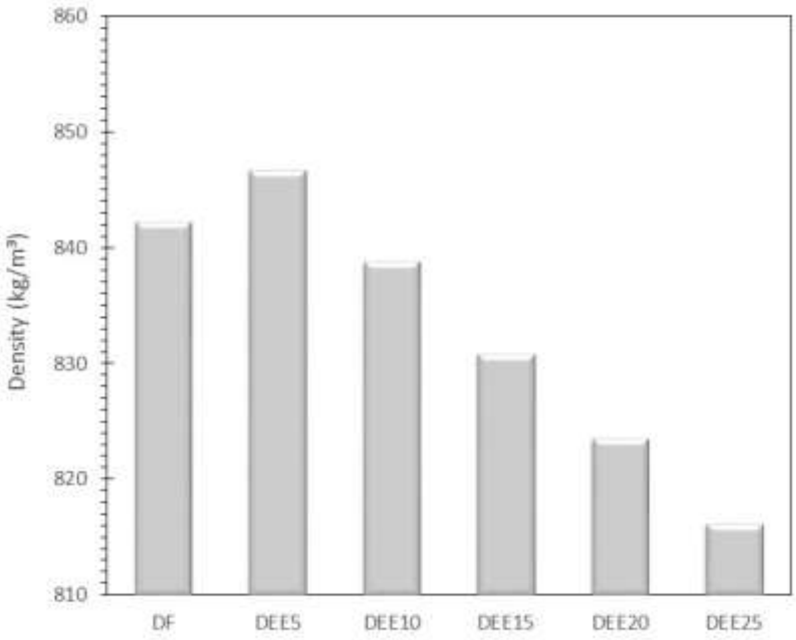

Density of ternary blends

Kinematic Viscosity

The kinematic viscosity values of ternary blends at 20°C are given in Figure 4. Kinematic viscosity decreases with the increase in the percentage of DEE. The viscosity values of DEE lie between 4.2319 mm^2/s and 2.0862 mm^2/s. Kinematic viscosity values are measured as 4.2319 mm^2/s, 3.5238 mm^2/s, 2.7855 mm^2/s, 2.2474 mm^2/s, and 2.0862 mm^2/s for DEE5, DEE10, DEE15, DEE20, and DEE25, respectively. The kinematic viscosities of DEE5, DEE10, DEE15, DEE20, and DEE25 are 13.88%, 28.29%, 43.32%, 54.27%, and 57.55% lower than that of DF (4.9140 mm^2/s at 20°C). The maximum decrease occurs with the use of DEE25. The decrease in kinematic viscosities of ternary blends is due to the considerably lower kinematic viscosity value of DEE, compared to DF. The high viscosity of BD is compensated by the lower viscosity of DEE. The reduced viscosity improves the fuel spray and atomization. Similarly, Górski et al. investigated some fuel properties of diethyl ether/linseed oil blends. It was found that the addition of DEE diminished the viscosity, density, and surface tension, and improved low temperature properties of tested oils (for example, cold filter plugging point (CFPP) decreased up to -24°C with the use of the blend including 30% DEE) [22].

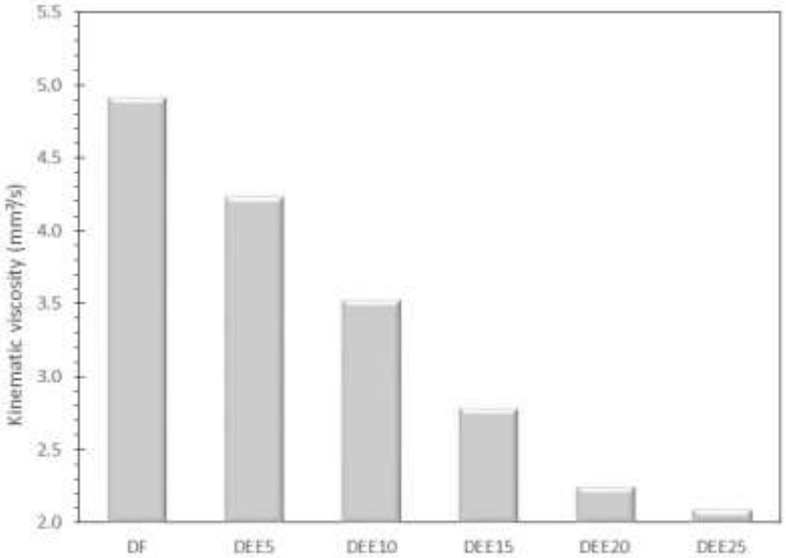

Kinematic viscosity of ternary blends

CONCLUSION

This study investigates some fuel properties (CFPP, CP, density, and kinematic viscosity) of ternary blends consisting of DF, BD, and DEE. The ternary blends consist of different volume concentrations of DEE (5%, 10%, 15%, 20%, and 25%), with the volume concentration of DF maintained constant at 70%. The ternary blends are named DEE5, DEE10, DEE15, DEE20, and DEE25. The fuel properties of ternary blends are measured according to international standards.

CFPP gradually diminishes with increasing DEE content from -6°C to -10°C, compared to DF (-5°C). In other words, the CFPP of DEE5, DEE10, DEE15, DEE20, and DEE25 blends are notably improved, making these blends suitable for use as diesel fuel additives, especially in cold weather conditions. All blends meet the CFPP requirements specified in EN 590. Similarly, the use of DEE10, DEE15, DEE20, and DEE25 results in a decrease in CP from -4°C to -7°C, compared to DF. At 15^{o}C, DEE5 is slightly denser than DF while DEE10, DEE15, DEE20, and DEE25 result in the density reductions of 0.40%, 1.35%, 2.22%, and 3.10%, respectively. DEE10, DEE15, and DEE20 comply with EN 590 standards for density, further supporting their potential as viable alternatives in the fuel industry. The kinematic viscosities of DEE5, DEE10, DEE15, DEE20, and DEE25 at 20^{o}C exhibit reductions of 13.88%, 28.29%, 43.32%, 54.27%, and 57.55%, respectively, compared to DF. The diminishing kinematic viscosity with increasing DEE concentration in the ternary blends improves fuel spray and atomization, contributing positively to engine performance and emissions.

This study suggests that DEE, when combined with DF and BD, can alleviate cold flow problems associated with biodiesel blends while meeting fuel quality standards at the same time. The effects of these blends on the performance and emissions characteristics of diesel engines can be investigated for further research to assess their practical feasibility.

References

[1] A. Ibrahim, "Investigating the effect of using diethyl ether as a fuel additive on diesel engine performance and combustion," Applied Thermal Engineering, 107, pp. 853-862, 2016.

A. López-Yerena, D. Guerra-Ramírez, B. Reyes-Trejo, I. Salgado-Escobar, and J. G. Cruz-Castillo, "Waste from Persea schiedeana fruits as potential alternative for biodiesel production," Plants, 11(3), pp. 252, 2022.

S. Sivalakshmi, and T. Balusamy, "Effect of biodiesel and its blends with diethyl ether on the combustion, performance and emissions from a diesel engine," Fuel, 106, pp. 106-110, 2013.

J. C. Ge, J. Y. Kim, B. O. Yoo, and J. H. Song, "Effects of engine load and ternary mixture on combustion and emissions from a diesel engine using later injection timing," Sustainability, 15(2), 1391, 2023.

F. Sundus, M. A. Fazal, and H. H. Masjuki, "Tribology with biodiesel: A study on enhancing biodiesel stability and its fuel properties," Renewable and Sustainable Energy Reviews, 70, pp. 399-412, 2017.

E. Alptekin, and M. Canakci, "Determination of the density and the viscosities of biodiesel–diesel fuel blends," Renewable Energy, 33(12), pp. 2623-2630, 2008.

B. Bailey, J. Eberhardt, S. Goguen, and J. Erwin, "Diethyl ether (DEE) as a renewable diesel fuel," SAE Transactions, pp. 1578-1584, 1997.

S. Iliev, "A comparison of ethanol, methanol, and butanol blending with gasoline and its effect on engine performance and emissions using engine simulation," Processes, 9(8), 1322, 2021.

D. C. Rakopoulos, C. D. Rakopoulos, E. G. Giakoumis, and A. M. Dimaratos, "Characteristics of performance and emissions in high-speed direct injection diesel engine fueled with diethyl ether/diesel fuel blends," Energy, 43(1), pp. 214-224, 2012.

S. Imtenan, H. H. Masjuki, M. Varman, I. R. Fattah, H. Sajjad, and M. I. Arbab, "Effect of n-butanol and diethyl ether as oxygenated additives on combustion–emission-performance characteristics of a multiple cylinder diesel engine fuelled with diesel–jatropha biodiesel blend," Energy Conversion and Management, 94, pp. 84-94, 2015.

K. Raja, V. Srinivasa Raman, R. Parthasarathi, K. Ranjitkumar, and V. Mohanavel, "Performance analysis of DEE-biodiesel blends in diesel engine," International Journal of Ambient Energy, 43(1), pp. 1016-1020, 2022.

A. Ibrahim, "An experimental study on using diethyl ether in a diesel engine operated with diesel-biodiesel fuel blend," Engineering Science and Technology, An International Journal, 21(5), pp. 1024-1033, 2018.

R. Raman, and N. Kumar, "Performance and emission characteristics of twin cylinder diesel engine fueled with mahua biodiesel and DEE," Transportation Engineering, 2, 100024, 2020.

N. Zhang, Z. Huang, X. Wang, and B. Zheng, "Combustion and emission characteristics of a turbo-charged common rail diesel engine fuelled with diesel-biodiesel-DEE blends," Frontiers in Energy, 5, pp. 104-114, 2011.

H. Wang, F. Wu, S. Guo, X. Pan, M. Hua, X. Zang, and J. Jiang, "Experimental investigation on the explosion limits of diethyl ether spray near boiling point temperatures," Journal of Loss Prevention in the Process Industries, 85, 105150, 2023.

K. R. Patil, and S. S. Thipse, "Experimental investigation of CI engine combustion, performance and emissions in DEE–kerosene–diesel blends of high DEE concentration," Energy Conversion and Management, 89, pp. 396-408, 2015.

R. Mahesh, "Production of biodiesel and exopolysaccharides from Scenedesmus abundans cell factory in flat panel photobioreactor with autoflocculation harvesting strategy," PhD Thesis, Department of Biosciences and Bioengineering Indian Institute of Technology Guwahati, Assam, India, July 2023.

The properties of diethyl ether. https://www.carlroth.com/com/en/a-to-z/diethyl-ether/p/8810.2. Accessed: 28.09.2023.

The properties of diethyl ether. https://www.sigmaaldrich.com/TR/en/sds/sial/296082. Accessed: 28.09.2023.

R. C. Elias, M. Senra, and L. Soh, "Cold flow properties of fatty acid methyl ester blends with and without triacetin," Energy & Fuels, 30(9), pp. 7400-7409, 2016.

G. Montero, and M. Stoytcheva, "Biodiesel-quality, emissions and by-products," Published by InTech, Printed in Croatia, November 2011, ISBN: 978-953-307-784-0.

K. Górski, R. Smigins, and R. Longwic, "Research on physico-chemical properties of diethyl ether/linseed oil blends for the use as fuel in diesel engines," Energies, 13(24), 6564, 2020.

Modified Vogelpohl Equation for Hydrodynamic Pressure between Rough Sliding Surfaces

M Gulzar[1], SA Qasim[2], MSS Malik[1,3], H.H Masjuki[4], MA Kalam[5]

[1]Department of Mechanical Engineering UET Taxila, Pakistan
[2]National University of Technology (NUTECH), Islamabad Pakistan
[3]School of Engineering and Materials Science, Queen Mary University of London, E1 4NS, United Kingdom
[4] Department of Mechanical Engineering, International Islamic University , Kuala Lumpur, Malaysia
[5]Univesrity of Technology Sydney, Australia.

Abstract

The purpose of this paper is to explore the surface roughness effects on hydrodynamic pressure between sliding surfaces under isothermal conditions. The proposed lubrication model provides effects of isotropic as well as anisotropic stochastic roughness in slider bearings. Using the Vogelpohl parameter, the modified two dimensional Reynolds equation is mathematically modeled to consider the effects of surface roughness.The comparison of results shows that the surface roughness not only changed the magnitude of dimensionless hydrodynamic pressures but also the position of pressure fields on the piston skirt is varied.

Keywords:
Hydrodynamics, Surface roughness, Flow factors, Incompressible flow

1. Introduction

Two sliding surfaces can be physically separated by hydrodynamic pressure of viscous liquid. Such characteristics help in reducing wear and friction between sliding surfaces. The theory of hydrodynamic lubrication and related analytical proof by Reynolds helped in breakthrough for developing bearings in various applications [1]. The presence of appropriate lubrication film is necessary and a relative sliding motion of inclined surfaces is essential for hydrodynamic pressure generation. To calculate the hydrodynamic pressure with better numerical accuracy of Reynolds equation, the Vogelpohl parameter was introduced [2]. The Vogelpohl parameter has been used by various researchers to model the Reynolds equation for smooth interacting surfaces [3-7]. For extending the application of Reynolds equation to real surfaces, two dimensional average Reynolds equation was modified by Patir and Cheng. They provided stochastic average flow model which include the surface asperity as well as surface pattern effects [8-9]. Finite slider bearing approximations were used in their model and analytical results were given in modified two dimensional average Reynolds equation [9-10]. With the changes in average Reynolds equation for surface roughness effects, the modification in Vogelpohl equation is also essentially required. To provide the Vogelpohl equation with surface roughness effects, the Vogelpohl parameter is introduced in average flow model of Reynolds equation. The present research provides new Vogelpohl equation and related numerical solution. The contributions by this research are as follows:

- The hydrodynamic pressure in flow factors based average Reynolds equation is evaluated in terms of Vogelpohl parameter, which enhances the accuracy of numerical solution.
- The model is applied on piston skirt lubrication and the simulation results are compared with smooth piston skirt and isotropic rough piston skirt lubrication models.

2. Theoretical Analysis

In the considered case two surfaces with random roughness are taken such that one surface is moving with velocity U_1 and other is stationary. The geometry of the considered problem of two rough sliding

surfaces is given in Figure.1. For developing mathematical model, the following assumptions are taken:
1. Newtonian behaviour of lubricant is considered.
2. No compressibility with isothermal condition.
3. Pressure at the inlet of contact region is zero.
4. Laminar flow of lubricant is considered.
5. Cavitations and squeeze film effects are ignored.

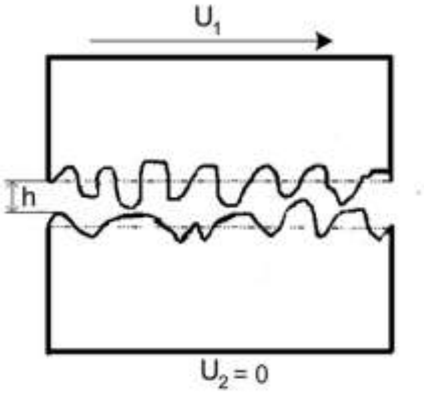

Figure1. Geometry of sliding rough surfaces

2.1 Dimensional analysis of Reynolds equation

The following two dimensional Reynolds equation developed by Patir and Cheng [10] is used to incorporate the rough surface profile effects in the lubrication model

$$\frac{\partial}{\partial x}\left(h^3\Phi_x\frac{\partial p}{\partial x}\right)+\frac{\partial}{\partial y}\left(h^3\Phi_y\frac{\partial p}{\partial y}\right)=6U\eta\left(\frac{\partial h}{\partial x}+\sigma\frac{\partial \Phi_S}{\partial x}\right) \tag{1}$$

To make the numerical solution more generalized, the modified two dimensional average Reynolds equation is non dimensionalized as follows.

$$\frac{\partial}{\partial x^*}\left(h^{*3}\Phi_x\frac{\partial p^*}{\partial x^*}\right)+\left(\frac{R}{L}\right)^2\frac{\partial}{\partial y^*}\left(h^{*3}\Phi_y\frac{\partial p^*}{\partial y^*}\right)=\frac{\partial h^*}{\partial x^*}+\sigma^*\frac{\partial \Phi_S}{\partial x^*} \tag{2}$$

The following equations represent pressure and shear flow factors which are function of dimensionless film thickness parameter 'σ/h' as well as surface pattern 'γ' [11]

$$\Phi_x=1+\left[3(\gamma-2)/(\gamma+1)\right][\sigma/h]^2\};\quad \Phi_y=\Phi_x(1/\gamma) \tag{3}$$

$$\Phi_s=\frac{\sigma_1^2}{\sigma^2}\phi_s(h/\sigma,\gamma_1)-\frac{\sigma_2^2}{\sigma^2}\phi_s(h/\sigma,\gamma_2);\qquad \phi_s(h/\sigma,\gamma)=\left[\frac{3}{(\gamma+1)}(\sigma/h)\right] \tag{4}$$

2.2 Modeling the modified Vogelpohl equation

The dimensionless Reynolds equation is solved numerically for Vogelpohl parameter 'M_v'. Vogelpohl parameter is given as

$$M_v = p^* h^{*1.5} \tag{5}$$

After incorporating the Vogelpohl parameter ‘M_v’ the non dimensional Reynolds equation can be written as

$$\frac{\partial}{\partial x}\left(h^{*3}\Phi_x \frac{\partial (M_v h^{*-1.5})}{\partial x^*} \right) + \left(\frac{R}{L}\right)^2 \frac{\partial}{\partial y^*}\left(h^{*3}\Phi_y \frac{\partial (M_v h^{*-1.5})}{\partial y^*} \right) = \frac{\partial h^*}{\partial x^*} + \sigma^* \frac{\partial \Phi_S}{\partial x^*} \tag{6}$$

Solving the above equation, the ‘Modified Vogelpohl equation’ is given as follows

$$\Phi_x \frac{\partial^2 M_v}{\partial x^{*2}} + \left(\frac{R}{L}\right)^2 \Phi_y \frac{\partial^2 M_v}{\partial y^{*2}} + \frac{\partial M_v}{\partial x^*}\frac{\partial \Phi_x}{\partial x^*} + \left(\frac{R}{L}\right)^2 \frac{\partial M_v}{\partial y^*}\frac{\partial \Phi_y}{\partial y^*} = FM_v + G \tag{7}$$

Where parameters ‘F’ and ‘G’ are given as

$$F = \frac{0.75\left[\Phi_x\left(\frac{\partial h^*}{\partial x^*}\right)^2 + \left(\frac{R}{L}\right)^2 \Phi_y \left(\frac{\partial h^*}{\partial x^*}\right)^2\right]}{h^{*2}} + \frac{1.5\left[\Phi_x\left(\frac{\partial^2 h^*}{\partial x^{*2}}\right) + \left(\frac{R}{L}\right)^2 \Phi_y\left(\frac{\partial^2 h^*}{\partial y^{*2}}\right) + \left(\frac{\partial \Phi_x}{\partial x^*}\right)\left(\frac{\partial h^*}{\partial x^*}\right) + \left(\frac{R}{L}\right)^2\left(\frac{\partial \Phi_y}{\partial y^*}\right)\left(\frac{\partial h^*}{\partial y^*}\right)\right]}{h^*} \tag{8}$$

$$G = \frac{\left[\frac{\partial h^*}{\partial x^*} + \sigma^* \frac{\partial \Phi_S}{\partial x^*}\right]}{h^{*1.5}} \tag{9}$$

After getting values of ‘M_v’, the values of hydrodynamic pressure ‘p^*’ can be evaluated from the definition in equation (5).

2.3 Finite difference equivalence

Using basic expressions of finite differencing as discussed by [12], the finite difference form of modified Vogelpohl equation is:

$$FM_{i,j} = \Phi_x\left(\frac{M_{i+1} - M_{i-1} - 2M_i}{(\delta x^*)^2}\right) + \left(\frac{R}{L}\right)^2 \Phi_y\left(\frac{M_{i+1} - M_{i-1} - 2M_i}{(\delta y^*)^2}\right) + \left(\frac{M_{i+1} - M_{i-1}}{2\delta x^*}\right)\frac{\partial \Phi_x}{\partial x^*} + \left(\frac{R}{L}\right)^2\left(\frac{M_{i+1} - M_{i-1}}{2\delta x^*}\right)\frac{\partial \Phi_y}{\partial y^*} - G \tag{10}$$

The finite difference form for modified Vogelpohl equation is

$$M_{i,j} = \frac{C_1\Phi_x(M_{i+1} - M_{i-1}) + \left(\frac{R}{L}\right)^2 \Phi_y C_2(M_{i+1} - M_{i-1}) + \frac{\partial \Phi_x}{\partial x^*} C_3(M_{i+1} - M_{i-1})}{2C_1\Phi_x + 2C_2\Phi_y + F} + \frac{\left(\frac{R}{L}\right)^2 \frac{\partial \Phi_y}{\partial y^*} C_4(M_{i+1} - M_{i-1}) - G}{2C_1\Phi_x + 2C_2\Phi_y + F} \tag{11}$$

Where C_1, C_2, C_3, C_4 can be given as

$$C_1 = \frac{1}{\delta x^{*2}} \quad ; \quad C_2 = \frac{1}{\delta y^{*2}},$$

$$C_3 = \frac{1}{2\delta x^{*}} \quad ; \quad C_4 = \frac{1}{2\delta y^{*}} \qquad (12)$$

3 Application of Modified Vogelpohl Equation

The modified Vogelpohl equation is applied on the piston skirt to investigate the effects of surface asperity height as well as surface pattern. For this purpose, the input data as well as governing equations for motion and lubrication film thickness between the piston skirt and the cylinder surfaces are required.

The important input parameters used in the model equations for lubrication and geometry of piston are given in Table 1.

Table 1: Input parameter for piston lubrication application

Input Parameter	Value	Input Parameter	Value
Radius of Piston	41.50 mm	Radial Clearance	10 µm
Stroke	83.60 mm	Roughness of piston skirt surface	1.4 µm
Length of Connecting Rod	133.00 mm	Roughness of cylinder bore	1.5 µm
Piston skirt length	33.80 mm	Mass of wrist-pin	0.090 kg
Piston skirt angle	37.5 degree	Mass of piston	0.295 kg
Engine Speed	600 RPM	Coefficient of friction	0.150

3.1. Piston primary motion equations

While considering the piston sliding motion, the related sliding velocity 'U' and acceleration of the piston are functions of the crank angle 'ψ'. For constant crankshaft speed 'ω', the piston speed is given by Zhu D *et al*.[13]

$$U = \dot{Y} r\omega \sin\psi + r\omega B \cos\psi (l^2 - B^2)^{-0.5}$$

where

$$B = C_p r \sin\psi \qquad (14)$$

3.2. Piston transverse motion equations

Eccentricities of top and bottom of surfaces of piston can be calculated by considering the forces and moments as given by [14]

$$\begin{bmatrix} a_{11} & a_{22} \\ a_{21} & a_{22} \end{bmatrix} \begin{bmatrix} \ddot{e}_t \\ \ddot{e}_b \end{bmatrix} = \begin{bmatrix} F_h + F_s + F_{fh} \tan\phi \\ M_h + M_s + M_{fh} \end{bmatrix} \qquad (15)$$

Where

$$a_{11} = m_{pin}\left(1 - \frac{a}{L}\right) + m_{pin}\left(1 - \frac{b}{L}\right) \qquad (16)$$

$$a_{12} = m_{pin}\left(\frac{a}{L}\right) + m_{pin}\left(\frac{b}{L}\right) \qquad (17)$$

$$a_{21} = \left(\frac{I_{pin}}{L}\right) + m_{pin}(a-b)(1 - \frac{b}{L}) \qquad (18)$$

$$a_{22} = m_{pin}(a-b)(\frac{b}{L}) - \left(\frac{I_{pin}}{L}\right) \quad (19)$$

$$F_h = R\iint_A p\ (\theta, y)\cos\theta d\theta dy \quad (20)$$

$$M_h = R\iint_A p(\theta, y)(a-y)\cos\theta d\theta dy \quad (21)$$

$$F_s = \tan\phi\left(F_G + \tilde{F}_{IP} + \tilde{F}_{IC}\right) \quad (22)$$

$$M_s = F_G C_p + \tilde{F}_{IC} C_g \quad (23)$$

The value of gas force F_G is a function of crank rotation angles for the 720 degree cycle. The forces and moments of rigid piston are given in Figure 2.

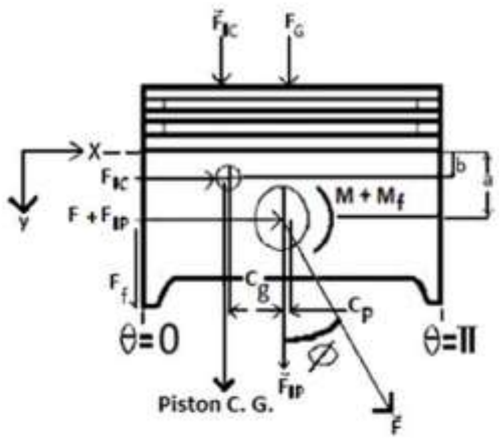

Figure 2. Forces and moments of rigid piston

3.3 Film thickness equation

The lubricant film thickness without the surface deformation effects is given by Zhu D *et al*. [14]

$$h = C + e_t(t)\cos x + \left[e_b(t) - e_t(t)]\frac{y}{L}\cos x\right]$$

3.4 Boundary conditions and solution domain

For surface of piston skirt, the boundary conditions require that ‘p*’ or ‘M_V’ are zero at the edges of the surface. For the bearing area of piston skirt the considered boundary conditions are given by Zhu D *et al*. [14]

$$\frac{\partial p}{\partial x_{\theta=0}} = \frac{\partial p}{\partial x_{\theta=\pi}} = 0$$

$p\ = 0$ when $\theta_1 \leq \theta \leq \theta_2$

$$p(\theta, 0) = p(\theta, L) = 0$$

4. Numerical Solution

Equation (15) represents an initial value problem for the two second order differential equations as represented by Qasim SA *et al*., (2011). It is solved to find out the values of piston eccentricities $e_t(t)$ and $e_b(t)$.

The average flow model based average Reynolds equation and the hydrodynamic film thickness equations are solved simultaneously by using the finite difference method and Gauss Seidel iterative scheme. A convergence criterion is defined for restricting the error within the allowable limits of the explicit numerical scheme. After that all the forces and moments in equation (15) are computed. When the satisfactory values of the secondary velocities $\dot{e}_t$, $\dot{e}_b$ are achieved, the piston position at the end of the current time step is obtained as represented by Zhu D *et al*. [1]

$$e_t(t_i + \Delta t) = e_t(t_i) + \Delta t \dot{e}_t(t_i)$$

$$e_b(t_i + \Delta t) = e_b(t_i) + \Delta t \dot{e}_b(t_i)$$

Converged solution is obtained in the sixth crank rotation cycle. The simulation results of the hydrodynamic lubrication model correspond to the 720 degree crank rotation.

5 Results and Discussion

Simulation results provide the plots for dimensionless hydrodynamic pressures, secondary eccentricities, and film thickness. The results of hydrodynamic pressure profiles are discussed here to highlight the effects of modified Vogelpohl parameter 'M_v'. In the considered case, the piston and cylinder surfaces are having transversally oriented surface roughness with Peklenik number = 1/3.

5.1 Comparison with smooth surface lubrication model

A comprehensive comparison is made for six crank angle positions of piston using less viscosity oil between surfaces as given in smooth surfaces lubrication model by Malik, M.A. *et al.*[14]. The dimensionless pressures are plotted and the peak pressure value is considered. The pressures on the top of piston skirt are taken positive and negative on the bottom of piston skirt. Figure 4 shows a comparison with γ=1/3 (transversal orientation) and γ=3 (longitudinal orientation).The magnitude of dimensionless hydrodynamic pressure is varied at all six crank angles but a shift of pressures from piston top skirt to piston bottom skirt can be observed at crank angle of 120 degrees. Figure 5 shows detailed comparison with γ=1/6 and γ=6. Here again it can be seen that the magnitudes of dimensionless hydrodynamic pressures are varied at all six crank angles. A shift of pressures from piston top skirt to piston bottom skirt can be observed at crank angle of 120 degrees. Another interesting shift of pressures can be seen at 480 degrees crank angle where only transversal rough surfaces provide positive value.

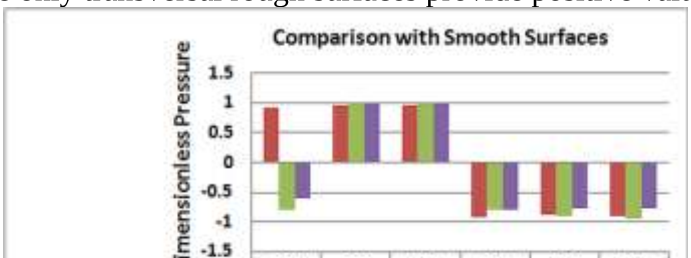

	120	240	360	480	600	720
smooth surfaces	0.9	0.95	0.96	-0.92	-0.88	-0.9
Peklenik Number = 1/3	-0.8	0.98	0.98	-0.8	-0.9	-0.95
Peklenik Number = 3	-0.62	0.99	0.99	-0.8	-0.78	-0.78

Figure 4 Dimensionless hydrodynamic pressures comparison of given model with smooth surfaces model for γ=1/3 and γ=3.

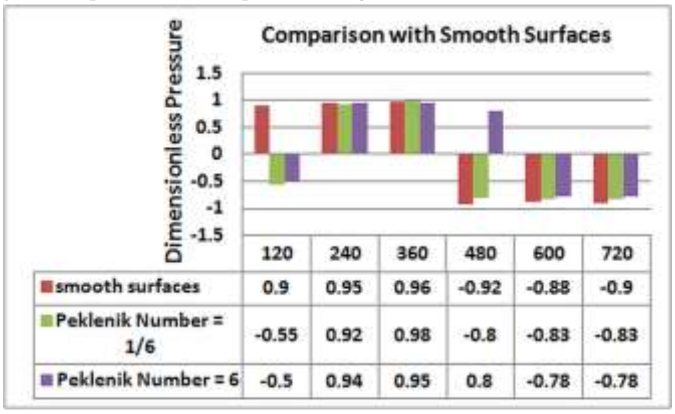

Figure 5 Dimensionless hydrodynamic pressures comparison of given model with smooth surfaces model for γ=1/6 and γ=6.

6 Conclusions

The modified Vogelpohl equation helps in providing dimensionless hydrodynamic pressures buildup between rough interacting surfaces. The modified Vogelpohl equation finds its application for lubrication characteristics of different bearings. The significant change in the magnitude and direction of pressures highlights the tribological application of the model between rough sliding surfaces. The modified Vogelpohl equation provide realistic picture of lubrication between piston and liner surfaces. The changes in magnitude and direction of dimensionless pressures are seen all over 720 degrees crank angle.

Acknowledgements:
Authors are also thankful to Professor Dr. Azad A. Siddiqui, Principal School of Natural Sciences, NUST, Pakistan, for his valuable guidance

References

[1] Reynolds, O. On the Theory of Lubrication and its Application to Mr Beauchamp Tower's Experiments Including an Experimental Determination of the Viscosity of Olive Oil, *Phil. Trans., Roy. Soc. London* **177**(1886), 157-234
[2] Vogelpohl, G. (1937) , "Beitrage zur Kenntnis der Gleitlagerreibung." *Ver. Deutsch. Ing. Forschungsheft*, pp. 386
[3] Chu Li-Ming and Hsiang-Chen Hsu ,Effect of surface roughness on pure Squeeze EHL motion of circular contacts", *Industrial Lubrication and Tribology*, **65** (2013), 259–265
[4] Qasim SA, , Malik MA, Mumtaz Ali Khan ,R.A Mufti(2011), Low viscosity shear heating in piston skirts EHL in the low initial engine start up speeds. *Tribology International* **44**(2011) 1134–1143
[5] Komar, I. , Vulić, N. and Roldo, L, Hydrodynamic and Elastohydrodynamic Lubrication Model to Verify The Performance Of Marine Propulsion Shafting, *TRANSACTIONS OF FAMENA* Vol.XXXVII, .**1** (2013), 15-27
[6] Pandazaras, C.N. and Petropoulos, G.P., (2001), A computational estimation of the critical rotational speed for finite hydrodynamically lubricated journal bearings, *Industrial Lubrication and Tribology*, **53**(2001).141 – 148
[7] D Dowson, J F Dunn, C M Taylor, The Piezo-Viscous Fluid, Rigid Solid Regime of Lubrication, Proceedings of the Institution of Mechanical Engineers, Part C: Journal of Mechanical Engineering Science, **197** (1983) 43-52
[8] Mahdavi, S.H. and Mansouri, S.H. , Effects of using smart fluid in lubrication on skirt- liner friction, *Industrial Lubrication and Tribology* , **64** (2012), 90– 97
[9] Patir, N. , Cheng and H.S., An Average Flow Model for Determining Effects of Three-Dimensional Roughness on Partial Hydrodynamic Lubrication. *ASME Journal of Tribology* **100** (1978) 12-17.
[10] Patir, N. , Cheng and H.S. Application of Average Flow Model to Lubrication Between Rough Sliding Surfaces". *ASME Journal of Tribology*, **101** (1979), 220-230
[11] Tripp, J. H. Surface Roughness Effects in Hydro-dynamic Lubrication: The Flow Factor Method, *ASME Journal of Tribology* **105**(1983) 458-463
[12] Hoffmann KA ,Chiang ST "Computational Fluid Dynamics". *EES* **1**(2000), 4th ed. 29-96
[13] Zhu, D., Cheng, H. S., Arai, T. and Hamai, K. A Numerical Analysis for Piston Skirts in Mixed Lubrication –Part I: Basic Modeling. *ASME Journal of Tribology* **114**(1991), 553-562
[14] Malik, M.A., Rashid, B., Qasim, S.A. and Khushnood S , Modeling and Simulation of Elastohydrodynamic Lubrication of Piston Skirts Considering Elastic Deformation in the Initial Engine Startup, *Proceedings of 2004 ASME/STLE International Joint Tribology Conference* , Long Beach, California USA.TRIB2004-64101, (2004) 859-867
[15] Gulzar, M., Qasim, S.A., Mufti, R.A. "Analyzing the Surface Roughness Effects on Piston Skirt EHL in Initial Engine Start-Up Using Different Viscosity Grade Oils" *Tribology in Industry*, **35** (2013).141-147